INFRARED INSIGHTS ON THE NATURE AND EVOLUTION OF STAR-FORMING GALAXIES

by Wiphu Rujopakarn

A Dissertation Submitted to the Faculty of the

DEPARTMENT OF ASTRONOMY

In Partial Fulfillment of the Requirements For the Degree of

DOCTOR OF PHILOSOPHY

In the Graduate College

THE UNIVERSITY OF ARIZONA

THE UNIVERSITY OF ARIZONA GRADUATE COLLEGE

As members of the Dissertation Committee, we certify that we have read the dissertation prepared by Wiphu Rujopakarn entitled "Infrared Insights on the Nature and Evolution of Star-Forming Galaxies" and recommend that it be accepted as fulfilling the dissertation requirement for the Degree of Doctor of Philosophy.

	_ Date: 23 July 2012
George H. Rieke	, ,
	_ Date: 23 July 2012
Daniel J. Eisenstein	
	_ Date: 23 July 2012
Buell T. Jannuzi	<i>y y</i>
	_ Date: 23 July 2012
Romeel Davé	,
	_ Date: 23 July 2012
Brant E. Robertson	
Final approval and acceptance of this dissertation is date's submission of the final copies of the dissertation	<u> </u>
I hereby certify that I have read this dissertation pre and recommend that it be accepted as fulfilling the dis	
	_ Date: 23 July 2012
Dissertation Director: George H. Rieke	,,,

STATEMENT BY AUTHOR

This dissertation has been submitted in partial fulfillment of requirements for an advanced degree at The University of Arizona and is deposited in the University Library to be made available to borrowers under rules of the Library.

Brief quotations from this dissertation are allowable without special permission, provided that accurate acknowledgment of source is made. Requests for permission for extended quotation from or reproduction of this manuscript in whole or in part may be granted by the head of the major department or the Dean of the Graduate College when in his or her judgment the proposed use of the material is in the interests of scholarship. In all other instances, however, permission must be obtained from the author.

SIGNED: Wiphu Rujopakarn

ACKNOWLEDGMENTS

I thank my advisors, George Rieke and Daniel Eisenstein, for their investment of time, thoughts, and energy in mentoring me in the past six years. I thank them for creating a safe harbor for me to learn, for encouragements to venture out into deeper water, for rescuing papers and proposals comprising this thesis from the verge of disaster, and, most importantly, for having faith that I will one day emerge as a scientist. There is an old adage in Thai that draws parallels between a teacher and a sculptor who crafts his art out of ordinary clay. Over the years, I have realized more and more how true this is. There is no appropriate way that I can thank them enough for their unending patience.

I am grateful for invaluable assistance with my research from the following astronomers: Almudena Alonso-Herrero, Romeel Davé, Arjun Dey, Mark Dickinson, Eiichi Egami, Chad Engelbracht, Buell Jannuzi, Jeyhan Kartaltepe, Chris Kochanek, Emeric Le Floc'h, John Moustakas, Pablo Pérez-González, Marie Rex, Marcia Rieke, Yancy Shirley, JD Smith, Ben Weiner, Christopher Willmer, my prelim and thesis committees, and the NDWFS, AGES, XBoötes, IRAC Shallow Survey, and PRIMUS teams. Casey Papovich deserves special recognition for providing practical advice during my first years in IR astronomy. I also appreciate the indispensable support from the staff of Steward Observatory, MMT, and LBT, with special thanks to Michelle Cournoyer, Jeff Fookson, Grisela Koeppen, Olga Kuhn, Sharon Jones, and Dave Thompson.

Thanks to the *Domeites* and current and former grad students of Steward Observatory, especially Tim Arnold, Vanessa Bailey, Fuyan Bian, Marc-André Besel, Richard Cool, Jenn Donley, Kristian Finlator, András Gáspár, Stephanie Juneau, Dennis Just, Desika Narayanan, Jane Rigby, Wayne Schlingman, Andy Skemer, Brandon Swift, Johanna Teske, Krystal Tyler, Greg Walth, and Yujin Yang, along with my friends and colleagues in Thailand, Hawaii, Ann Arbor, and Tucson.

I owe deep gratitude to my undergraduate advisor, Carl Akerlof, at the University of Michigan, together with the ROTSE collaboration, for getting me started in astronomy research, and Ajarn Tossaporn Wongratana, who kindly took me on as an intern at the Natural History Museum of Chulalongkorn University during the summers of my childhood. Those summers proved to be extremely influential to my training as a scientist later on.

Special thanks go to the following figures whose support is pivotal to my career as an astronomer: Khun Thagoon and Anna Kirdkao; Drs. Saran Poshyachinda, Pisarn Soydhurum, and Helmut Abt; Professors Boonraksar Soonthorntham, Prapod Assavavirulhakarn, Pairash Thajchayapong and Tim McKay.

I am indebted to the Royal Thai Government for a decade-long scholarship during 2002 - 2012 to pursue physics and astronomy in the US.

Lastly, I thank my parents and Kamolnate, whom this thesis is dedicated to, for more than I can ever say.

DEDICATION

To my parents, and Kamolnate.

๑ ละอองละเอียดล่องลอย ก่อนก่อเป็นกลุ่มรวมกัน
 เป็นหมู่เป็นมวลมหันต์ พลุ่งพล่านพลังพลัน สาดแสงแรงรุ่งระวี
 เพลิงเพริศเฉิดฉายรังสี เติบตามวิถี ตราบสิ้นเชื้อไขของกรรม
 ชีวิตดวงดาวเดินดำ- เนินไปในธรรม เวียนวนกลไกจักรวาล
 ไขว่คว้าความรู้ไขขาน ศึกษาแก่นสาร รู้นอกเพื่อรู้ในเราพ

– แม

TABLE OF CONTENTS

L	IST	of Fig	URES	9
L	JST	OF TAI	BLES	11
				12
F	ABS I	IKACI		14
Сна	PTE	r 1 I	NTRODUCTION	14
Сна	PTE	r 2 N	Morphology and Size Differences Between Local and	
F	IIGI	H REDS	HIFT LUMINOUS INFRARED GALAXIES	20
2	.1	Introd	uction	21
2	.2	The M	easurements	23
		2.2.1	Intermediate and High-Redshift Compilation	23
		2.2.2	Local Compilation	34
		2.2.3	HST Imaging of the High-Redshift Sample in the GOODS-	
			N Field	39
2	.3	Result	s	40
		2.3.1	$\Sigma_{\rm SFR}$ as a Tracer of Star-Forming Environment	43
		2.3.2	A Unified View of Star-Forming Galaxies	46
2	.4	Chapte	er Conclusions	50
Сна	PTE	R 3 N	MID-INFRARED DETERMINATION OF TOTAL INFRARED LUMI-	
			D STAR FORMATION RATES OF LOCAL AND HIGH-REDSHIFT	
				52
	.1		uction	53
3	.2		ifying the IR SED Evolution	56
		3.2.1	$\Sigma_{ m L(TIR)}$ as an Indicator of SEDs for Star-Forming Galaxies	56
		3.2.2	The Local Reference for the Galaxy SEDs	67
3	.3	A Mid	-IR Estimator for $L(TIR)$ at $0 < z < 2.8 \ldots$	68
3	.4		g the New 24 μ m $L(TIR)$ Indicator	75
		3.4.1	Testing the 24 μ m $L(TIR)$ Indicator with Far-IR $L(TIR)$ Mea-	
			surements for Individual Galaxies	76
		3.4.2	Tests of the 24 μ m $L(TIR)$ Indicator on Average SEDs	92
		3.4.3	Verifying the Uncertainty Estimate for Individual Galaxies	
			with an Independent Sample	93
3	.5	L(TIR))—SFR Relation	96
3	.6	Discus	ssion	97
		3.6.1	Validity of the Aromatic Emission as a $L(TIR)$ and SFR In-	
			dicator	98
		3.6.2	Modes of Star Formation and the Validity of the Main Se-	
			quence Assumption	102

TAB	LE OF C	CONTENTS — CONTINUED
	3.6.3	The Eddington Luminosity of ULIRGs
3.7	Chapte	er Conclusions
Снарт	er 4 L	BT AND Spitzer Spectroscopy of Star-Forming Galaxies
		3: Extinction and Star Formation Rate Indicators . 108
4.1	Introd	uction
4.2	Observ	vations and Data Reduction
	4.2.1	Sample Selection
	4.2.2	LBT/LUCIFER Near-infrared Spectroscopy
	4.2.3	LBT/LUCIFER Data Reduction
	4.2.4	Spitzer IRS Mid-infrared Spectroscopy and Data Reduction . 117
	4.2.5	Archival and Literature Data
	4.2.6	Additional Spitzer MIPS Photometry and Data Reduction 126
	4.2.7	Augmented Sample Summary
4.3	Result	s
	4.3.1	Near- and Mid-IR Spectroscopy
	4.3.2	Metallicity
	4.3.3	Infrared Luminosity and Star Formation Rate 132
	4.3.4	Extinction
4.4		of Extinction on Star Formation Rate Indicators 144
4.5	Chapte	er Conclusions
Снарт	er 5 T	THE EVOLUTION OF THE STAR FORMATION RATE OF GALAXIES
AT (0.0 < z < 0.0	< 1.2
5.1		uction
5.2		ata
	5.2.1	Spitzer 24 μ m-Observations, Reduction, and the Final Cat-
		alogue
	5.2.2	Optical Spectroscopy Target Selection, Observation, and the
		Final Catalogue
5.3	Infrare	ed Luminosity Function
	5.3.1	24 μ m and I-band Luminosity Estimation
	5.3.2	Separating Starforming Galaxies and AGN Hosts 159
	5.3.3	Methodology
	5.3.4	Bivariate Selection Bias
	5.3.5	Evolution of the Luminosity Function
	5.3.6	Estimation of SFR
	5.3.7	Uncertainties Analysis for the LF and SFR
5.4	Result	
	5.4.1	Local 24 μ m Luminosity Functions
	5.4.2	Evolution of the 24 μ m LF

TABLE OF CONTENTS — CONTINUED	
5.4.3 Extending the LF evolution constraint to $z \sim 1.2 \ldots$	185
5.4.4 The Evolution of the Star Formation Rate Density	186
5.5 Chapter Conclusions	
CHAPTER 6 SUMMARY AND THE WAY FORWARD	194
6.1 Systematic study of the structure of star-forming galaxies from lo-	
cal to high- z	195
6.2 A new mid-IR star formation rate indicator for $0 < z < 3 \dots \dots$	196
6.3 Physical properties of individual star-forming galaxies at $1 < z < 3$	197
6.4 The Evolution of Star-forming Galaxies at $0 < z < 1.2 \dots$	198
6.5 Future Works	
APPENDIX A ESTIMATION OF PHYSICAL SIZES FOR LOCAL IR GALAXIES	202
A.1 Normal Star-Forming Galaxies	202
A.2 LIRGs	203
A.3 ULIRGs	
References	210

LIST OF FIGURES

2.1	Measurement of the physical size of star-forming regions in local galaxies	26
2.2	HST/ACS imaging of the subsample of our compilation in the	
	GOODS field	35
2.3	Physical sizes of star-forming galaxies at various redshifts and IR	
	luminosities	41
2.4	IR luminosity surface density as a function of IR luminosity	42
2.5	The logarithmic ratio of 24 μ m and 1.4 GHz flux for our galaxy	4.4
2.0	sample	44
2.6	The logarithmic ratio of the observed 24 μ m and 1.4 GHz flux ratios and those predicted by the Rieke et al. (2009) SED library	48
2.7	The stacked spectra of high-redshift ULIRGs compared to the local	40
2.7	SED templates	49
	old unplaces	1,
3.1	The relationships between the $L(TIR)$ and $L(TIR)$ surface density	
	for the local and non-local galaxies	59
3.2	The coefficients for the relationship between the observed <i>Spitzer</i>	_
2.2	$24 \mu \text{m}$ flux and the $L(\text{TIR})$	7 4
3.3	Comparison of $L(TIR)$ estimated with the new estimator to $L(TIR)$	O.
3.4	measured from $Herschel$	87
J. 4	library to $L(TIR)$ measured from $Herschel \dots \dots \dots \dots$	89
3.5	Comparison of $L(TIR)$ estimated from the new indicator to $L(TIR)$	0,
0.0	measured from the stacked and gravitationally lensed galaxies with	
	far-IR observations	91
3.6	The sources of scatter in using aromatic emissions (e.g., PAH) to	
	predict $L(TIR)$ and SFR	99
3.7	The correlation between the rest-frame L(8 μ m) and L(TIR) for	
	local star-forming galaxies	101
11	Images of the larged calaxies in our sample from the Hubble Space	
4.1	Images of the lensed galaxies in our sample from the <i>Hubble</i> Space Telescope Advanced Camera for Survey (ACS)	115
4.2	Spitzer/IRS mid-IR and LBT/LUCIFER near-IR spectra of Abell	110
1.2	2218b	120
4.3	Spitzer/IRS mid-IR and LBT/LUCIFER near-IR spectra of Abell	
	2667a, Abell 2218a, and Abell 1835a	121
4.4	Spitzer/IRS mid-IR spectra for the Clone and cB58	
4.5	Spitzer/IRS SL2 spectrum for the 8 O'clock arc	130
4.6	The relationship of 6.2 μ m PAH emission line luminosity to $L(TIR)$	138

4.7	The comparison of optical extinction from our study with the liter-
	ature
4.8	Comparison of star formation rate (SFR) indicators
5.1	Redshift distribution of the rest-frame 24 μ m luminosity for our
	sample
5.2	Identification of active galactic nuclei
5.3	Mid-IR properties of active galactic nuclei in our sample 163
5.4	The 24 μ m Luminosity distribution of the starforming and AGN
	sub-samples at $0.05 \le z \le 0.65$
5.5	The 24 μ m and I-band bivariate luminosity functions 173
5.6	Evolution of the 24 μ m luminosity functions
5.7	The mid-IR local luminosity function
5.8	Evolution of the characteristic 24 μ m luminosity of galaxies 187
5.9	Evolution of the star formation rate density $(\dot{\rho}_*)$ as a function of
	redshift

LIST OF TABLES

2.1	High-Redshift Compilation of Star-Forming Galaxies	29
3.1 3.2 3.3	Local Galaxies with $\Sigma_{\rm L(TIR)}$ Measurement	
	SED Templates	72
3.4	Coefficients of the Fits for the Relation Between <i>Spitzer</i> 24 μ m Flux and the $L(TIR)$	73
3.5	Individual Galaxies in the ECDFS with <i>Herschel/SPIRE</i> observa-	70
0.6	tions and ACES Spectroscopic Redshifts	80
3.6	Galaxies with Far-IR $L(TIR)$ Measurement for $L(TIR)$ Indicator Calibration	86
3.7	The Luminosity of the Appropriate Rieke et al. (2009) SED Template to Describe SED of a Star-Forming Galaxy for a Given 24 μ m Flux and Redshift	90
4.1	The Sample of High-Redshift Strongly-Lensed Star-Forming Galax-	
4.2	ies	
4.2	Near- and Mid-Infrared Spectroscopic Observations	
4.4	Measured Fluxes	
4.5	Metallicity Estimates from [NII]/ $H\alpha$	
4.6	Derived Quantities	136
5.1	Parameters of the mid-IR local luminosity function in comparison with other works	181
5.2	The 24 μ m and total-IR luminosities above which the cumulative number density of starforming galaxies is $10^{-4} {\rm Mpc}^{-3}$ for each red-	101
г о	shift bin	184
5.3	Evolution of the characteristic 24 μ m luminosity, L _* (24 μ m), and the star formation rate density, $\dot{\rho}_*$, to $z \sim 1.2 \ldots \ldots \ldots$	190
A.1	Local Compilation of Star-Forming Galaxies	207

ABSTRACT

The peak of the star formation rate (SFR) of the Universe is widely accepted to be at 1 < z < 3, after which the SFR declined by more than an order of magnitude to the present level. The mechanisms resulting in the decline and the nature of individual star-forming galaxies at the peak of galaxy evolution, however, are poorly understood. This thesis summarizes an effort to understand both the statistical properties of star-forming galaxies and the physical conditions in individual galaxies at 0 < z < 3. I have studied the star formation (SF) sizes of local and high-z ultraluminous infrared galaxies (ULIRGs) using Pa α , 24 μ m and radio continuum observations and discovered that high-z ULIRGs have extended SF regions over 3-10 kpc, similar to local lower LIR SF galaxies, but with a scaled-up star formation rate surface density, Σ_{SFR} . Local ULIRGs, in contrast, are compact and invariably merger-triggered starbursts. A major implication to galaxy evolution is that there is a route besides major mergers to trigger very high levels of SF activity at $z \sim 2$, a conclusion further supported by our morphological study. I also find Σ_{SFR} to be a good indicator of the IR galaxy spectral energy distribution universally and use this fact to develop a new SFR estimator using single- band 24 μ m observations. The resulting indicator predicts IR luminosity and SFR within 0.15 dex of the values measured with far-IR photometry. This affords the deepest unobscured probe of SF at 0 < z < 3. According to my separate study, the spread of extinction values of SF galaxies is larger than previously known from optical observations and also indicates a large variety of dust distribution scenarios, from a uniform mixture that resembles the extinction screen assumption to inhomogeneous mixtures, which could undermine the assumptions commonly used to correct for extinction at high-z and necessitates the use of unobscured SF tracers. Lastly, I present the luminosity functions of galaxies and their evolution measured from IR observations out to z=1.2.

CHAPTER 1

Introduction

The history of the Universe is written in the light of young stars. After its origin in the Big Bang, the Universe was largely a homogeneously cold and dark environment devoid of features until gravitational accretion of primordial cold gas precipitated into the first stars when the Universe was about a tenth of its present age. Since then, star formation rapidly transformed the Universe into one filled with stars, galaxies, large scale structures, and the heavy elements that are a by-product of stellar evolution, which constitute the building blocks for life.

The advancement of ground-based and space observatories in the past two decades conferred an unprecedented view into the past and allowed astronomers to identify the peak epoch of star formation and galaxy assembly activities as the period between 8-11 billion years ago. During this period, star formation was intense and ubiquitous, but the cosmic star formation rate has declined by a factor of 20 ever since. The most transformative era has passed and the present day Universe is filled with relics from the peak galaxy evolution epoch: the extremely diverse properties of today's galaxies; environment, groups and clusters of galaxies; central bulges as that of our Galaxy; heavy elements-enriched interstellar medium; the tight relationship between velocity dispersion of the galactic bulges and the mass of the supermassive black holes residing in their centers; and the dramatic differences between stellar mass and halo mass functions, to name a few. A goal of the study of galaxy evolution is to relate these present-day relics with the processes that shaped them in the distant Universe, as seen by looking back in time, and determining *how* these processes shaped them. This thesis examines various aspects of star formation in the past 11 billion years through the infrared (IR) light that affords insights into star-forming regions that are heavily obscured by dust and are nearly invisible in visible light. Specifically, the research presented in this thesis focuses on the properties of the intensely star-forming galaxies or *starburst galaxies*, where most of the stellar mass in the Universe was formed, their evolution, and on developing a consistent measure for star formation across the cosmic time.

The star formation rate (SFR) in starburst galaxies often exceed $10-1000\times$ that of the Milky Way, which forms about one solar mass worth of stars per year. With such an elevated star formation rate, the microscopic grains naturally present in molecular gas cloud, by which the star formation is fueled, collectively absorb most of the optical and UV radiation from young stars within and re-radiate the energy in thermal infrared (5 – $1000~\mu\text{m}$), effectively obscuring the optical view of the star-forming activity in its entirety. In other words, the sites of the most intense star formation in the Universe are often obscured by dust to the extent that they were never identified as such by conventional optical instruments.

It was only when mid-IR (5 - 30 μ m) detectors became available in the late 1960s that Low & Kleinmann (1968) and Kleinmann & Low (1970) first identified nearby galaxies with IR output comparable in energy to their optical emission. Rieke & Low (1972) subsequently measured IR photometry of a larger sample and identified four *Ultra-High Luminosity Galaxies* (now known as *ultra-luminous infrared galaxies* or ULIRGs). IR emissions were associated with thermal dust emission, instead of other candidate emission processes, such as synchrotron radiation by the lack of time-domain photometric variability in the IR (theoretical argument given by, e.g., Rees et al., 1969). In the 1970s, IR observations were conducted for increasingly large samples and diverse types of galaxies, including normal spirals analogous to our Galaxy, starbursts, and Seyferts (Rieke &

Low, 1975; Neugebauer et al., 1976; Rieke, 1978; Rieke & Lebofsky, 1978). Optical morphological studies in the same period revealed two distinct types of IR luminous galaxies: normal spirals and Seyferts, with the latter commonly found to have excess 1.4 GHz radio continuum emission compared to the former (e.g., Condon & Dressel, 1978). These findings pointed to star formation and active galaxy nuclei (AGN) being the sources of energy for the thermal dust emission. Star formation and AGN activities were later found to commonly coexist in host galaxies and their disentanglement remains an issue to this day. Not surprisingly, the identification and exclusion of AGNs will be among the recurring themes in this thesis. The fact remains, however, that once AGNs are carefully excluded, IR emission can serve as a tracer for star formation.

The series of IR space observatories since 1983 has revolutionized infrared astronomy, namely the *Infrared Astronomical Satellite* (*IRAS*, 1983); *Infrared Space Observatory* (*ISO*, 1995); *Spitzer* (2003); *Akari* (2006); *Herschel Space Observatory* (*Herschel*, 2009); and the *Wide-field Infrared Survey Explorer* (*WISE*, 2009). *IRAS* surveyed the entire sky in mid and far-IR at 12, 25, 60, and 100 μ m for the first time; the latter two are not accessible through the Earth's atmosphere. Early *IRAS* samples are dominated by spiral galaxies because they emit large amounts of energy in the IR, while very few of ellipticals do (de Jong et al., 1984), confirming that IR galaxies are not a special class of objects, but rather an unseen facet of typical star-forming galaxies. Local luminosity functions of IR galaxies were first constructed by Saunders et al. (1990) and Rush et al. (1993). Astronomical capability¹ of infrared telescopes progressed quickly, doubling approximately every ten months since the 1970s (Rieke & Rieke, private comm.), such that *ISO*, whose aperture is essentially the same as *IRAS*, was more than 1,000 times more capable,

¹defined as (number of pixels) \times (sensitivity per pixel)²

allowing the IR facet of galaxies to be studied beyond the local Universe.

Source counts for IR star-forming galaxies from ISO indicate rapid evolution with redshift (Elbaz et al., 1999; Franceschini et al., 2001). In the same period, the emergence of deep-field-style surveys such as the Hubble Deep Field, development of the photo-z techniques, and high-multiplex spectroscopy yielded multiwavelength samples with redshift measurements, which led to studies of the cosmic star formation rate (SFR) history beyond z > 1, half of the cosmic time (Lilly et al., 1996; Madau et al., 1996). Significant contributions came from optical observations that probe the rest-frame ultraviolet (UV) at intermediate and high-z (see, e.g., the review by Ferguson et al., 2000). But it was also quickly realized that star formation in the high redshift Universe is typically obscured and the extinction correction required is on the order of 0.5 dex or more (e.g., Steidel et al., 1999), which introduces uncertainties to the SFR estimates. The larger aperture and, again, vastly improved IR detector technology of Spitzer came to the rescue by offering unobscured (i.e., not affected by dust extinction) probes for star formation out to z > 2 (e.g., Pérez-González et al., 2005; Caputi et al., 2007; Rodighiero et al., 2010; Magnelli et al., 2011). In conjunction with optical and radio tracers for star formation, IR observations constrained the peak of the cosmic SFR history to within the range of 1 < z < 3 (compilation in, e.g., Hopkins, 2004). This period coincides with the peak epoch of the stellar mass assembly of massive galaxies (compilation in, e.g., Pérez-González et al., 2008) and AGN activity (Hewett et al., 1993; Schmidt et al., 1995; Fan, 2006), suggesting evolutionary relationships between star formation and these processes.

As mentioned earlier, the cosmic SFR has declined by a more than a factor of 20 since the peak period to the present day level (Le Floc'h et al., 2005; Magnelli et al., 2009; Rujopakarn et al., 2010). The mechanism driving this decline

is still a subject of debate. Supernovae that would occur frequently in intensely star-forming galaxies as well as the photo-heating by UV background were suggested as potential mechanisms regulating SF (McKee & Ostriker, 1977; Hollenbach & Tielens, 1999). Radiative and momentum-driven feedback from AGN that could be ignited during major galaxy mergers could, in theory, blow out cold gas and deprive star formation of its raw material, effectively shutting it down (e.g., Hopkins et al., 2006; Croton et al., 2006). These explanations are consistent with local observations that the most luminous starbursts are invariably merging systems that also harbor AGNs (see, e.g., a review by Sanders & Mirabel, 1996), and also the observations of post-starburst galaxies that could represent a population that have recently undergone star formation quenching (Quintero et al., 2004). Although gas-rich major mergers, intense bursts of star formation, and luminous AGNs necessary to shut off star formation in this manner were observed at high-z, they appeared to be rare and were often seen only in the most massive halos (e.g., Tacconi et al., 2008; Ivison et al., 2012). On the other hand, observations commonly found gas-rich galaxies at high-z harboring intense star formation that show no dynamical signs of major mergers (e.g., Tacconi et al., 2010), which highlights possible routes towards starbursts other than interactions. This leads to the question of how starbursts were fueled at high-z and whether the mechanisms are similar to those found at lower-z.

These are among the controversies surrounding the field of galaxy evolution at the time of my thesis work. In this thesis, I studied representative samples of galaxies out to $z \lesssim 3$ both on an individual basis, namely the physical properties of individual galaxies (e.g., physical size, star formation rate, extinction, and metallicity), as well as studying large samples of galaxies collectively as a statistical sample to understand their luminosity function and its evolution. I

also focused on developing the method to trace star formation in a self-consistent manner at 0 < z < 3 from the *Spitzer* 24 μ m observations, which, in the deep survey fields, are the deepest unobscured probe of SFR in this redshift range. This work is made possible by the wealth of multiwavelength data that cover galaxies across the X-ray, UV, optical, infrared, sub-millimeter, and radio regimes accumulated in the *Great Observatories* era, as well as the emergence of the high-throughput near-IR ground-based spectroscopy via large telescopes, such as that on the Large Binocular Telescope.

This thesis is organized as follows. Chapter 2 examines the structural differences between local and high-z intensely star-forming galaxies. Chapter 3 explores the implication of the structural differences on the star formation rate indicator and developed a new mid-IR tracer for star formation. Chapter 4 studies individual star forming galaxies at 1 < z < 3 that are gravitationally lensed, which allowed detailed spectroscopic studies in the mid-IR. Chapter 5 constructs the luminosity function of star forming galaxies out to $z \sim 1.2$, quantifying their evolution and their star formation rates. Lastly, Chapter 6 summarizes these results and discusses the ongoing investigations that stemmed from this thesis work using the rapidly emerging new multiwavelength capabilities.

CHAPTER 2

MORPHOLOGY AND SIZE DIFFERENCES BETWEEN LOCAL AND HIGH REDSHIFT

LUMINOUS INFRARED GALAXIES¹

We show that the star-forming regions in high-redshift luminous and ultraluminous infrared galaxies (LIRGs and ULIRGs) and submillimeter galaxies (SMGs) have similar physical scales to those in local normal star-forming galaxies. To first order, their higher infrared (IR) luminosities result from higher luminosity surface density. We also find a good correlation between the IR luminosity and IR luminosity surface density in starburst galaxies across over five orders of magnitude of IR luminosity from local normal galaxies to $z \sim 2$ SMGs. The intensely star-forming regions of local ULIRGs are significantly smaller than those in their high-redshift counterparts and hence diverge significantly from this correlation, indicating that the ULIRGs found locally are a different population from the highredshift ULIRGs and SMGs. Based on this relationship, we suggest that luminosity surface density should serve as a more accurate indicator for the IR emitting environment, and hence the observable properties, of star-forming galaxies than their IR luminosity. We demonstrate this approach by showing that ULIRGs at $z\sim 1$ and a lensed galaxy at $z\sim 2.5$ exhibit aromatic features agreeing with local LIRGs that are an order of magnitude less luminous, but have similar IR luminosity surface density. A consequence of this relationship is that the aromatic emission strength in star-forming galaxies will appear to increase at z > 1 for a given IR luminosity compared to their local counterparts.

¹Originally appeared as Rujopakarn et al. 2011, The Astrophysical Journal, 726, 93

2.1 Introduction

Luminous and Ultraluminous Infrared Galaxies (LIRGs and ULIRGs) whose total infrared luminosities, $L({\rm TIR})$, are in the range of $10^{11}-10^{12}$ and $>10^{12}$ L_{\odot} , respectively, are among the most important populations for the study of galaxy evolution. Their extreme $L({\rm TIR})$ signifies intense star formation hidden by dust and only visible through the infrared (IR) emission resulting from the reprocessing of UV photons that originate from populations of rapidly forming hot young stars. They are among the most extreme star-forming regions known.

A majority of the local ULIRGs are disturbed systems of galaxies undergoing mergers. Some ULIRGs harbor active galactic nuclei (AGN) often thought to be associated with merger activity and the resulting enhanced dense molecular gas fractions observed in the nuclei of these systems (e.g. Gao & Solomon, 2004; Juneau et al., 2009). Locally, luminous IR galaxies are very rare (Lagache et al., 2005) but they contribute significantly to the total IR energy density beyond redshift $z\sim 1$ (e.g., Le Floc'h et al., 2005; Pérez-González et al., 2005; Rodighiero et al., 2010). At high redshift, $z\gtrsim 2$, luminous IR galaxies are typified by submillimeter galaxies (SMGs; e.g. Blain et al., 2002). So far it is common to view SMGs as a more luminous counterpart of local ULIRGs. This naturally leads to the view of SMGs being disturbed, interacting systems (e.g. Tacconi et al., 2008).

However, there are many indications that the SEDs of the high redshift infrared galaxies differ systematically from those of local galaxies of similar luminosity. Papovich et al. (2007) found that the 70 μ m (observed) outputs tended to be weaker relative to those at 24 μ m (observed) than expected from local templates. Many authors have found that the aromatic bands in these galaxies appear to be similar in structure to those in significantly lower-luminosity local galaxies (e.g., Rigby et al., 2008; Farrah et al., 2008; Takagi et al., 2010). The far infrared

SEDs appear to be cold, again similar to those of lower luminosity local galaxies (e.g., Pope et al., 2006; Symeonidis et al., 2009; Muzzin et al., 2010). These findings suggest an underlying physical difference between local luminous infrared galaxies and those at high redshift. Rigby et al. (2008) suggested that such a difference might arise either through reduced metallicity or lower optical depth due to a greater extent of the emitting regions. Erb et al. (2006) find that the metallicities are of order three times lower at $z\sim 2$ for a given galaxy mass. Engelbracht et al. (2008) show that, for local galaxies, there is only a weak trend in 8 μ m vs. L(TIR) down to 1/3 solar metallicity, and that at lower metallicity the 8 μ m luminosity is suppressed. This correlation is also reported for $z\sim 2$ galaxies by Reddy et al. (2010). We conclude that reduced metallicity is unlikely to be the primary cause of the changes in SED with redshift. We therefore turn our attention to the second possibility, that the galaxies have structures different from local ones of similar luminosity.

Recent high-resolution studies of SMGs in the submillimeter, radio, and near-IR have shown that their star-forming regions are generally relatively extended, with diameters of order 1-10 kpc (Chapman et al., 2004; Muxlow et al., 2005; Biggs & Ivison, 2008; Bothwell et al., 2010; Casey et al., 2009; Iono et al., 2009; Lehnert et al., 2009; Carilli et al., 2010; Swinbank et al., 2010a; Tacconi et al., 2010; Younger et al., 2010). Thus, the surface densities of the star formation rate (SFR) must be substantially lower in the high-z galaxies than for the local ones of similar $L({\rm TIR})$. This paper explores the importance of this difference in explaining the different SED behavior. We make the simplest possible assumption, that the SED is a function of the SFR surface density, $\Sigma_{\rm SFR}$, and that galaxies with similar $\Sigma_{\rm SFR}$, and consequently similar $L({\rm TIR})$ surface density, $\Sigma_{\rm L(TIR)}$, will have similar optical depths in their star forming regions and similar SEDs. In section 2.2, we

describe the compilation of data for the study as well as discuss our derivation of a consistent set of sizes for the star forming regions for 0 < z < 2.5. Section 2.3 shows the results and discusses the implications for both galaxy evolution and for improved estimates of the SFRs of high redshift IR galaxies. We assume a Λ CDM cosmology with $\Omega_m = 0.3$, $\Omega_{\Lambda} = 0.7$, and $H_0 = 70$ km s⁻¹Mpc⁻¹ throughout this paper.

2.2 The Measurements

A major challenge in studying the $\Sigma_{L(TIR)}$ of galaxies across a broad redshift range is to obtain physical size information for the IR-emitting regions in a consistent way for both the local and high-redshift samples. We discuss in this section the compilation of physical sizes and IR luminosity data from the literature and our steps to compare them on the same metric. Despite the abundantly available high-quality data for local galaxies, it is necessary to select a subset that can best match the high-redshift sample. We therefore will begin our discussion with the high-redshift compilation, then follow with the local compilation.

2.2.1 Intermediate and High-Redshift Compilation

The past five years have seen an unprecedented number of high-resolution, multiwavelengths observations of high-redshift galaxies. Our compilation of the physical sizes of intermediate and high-redshift starburst galaxies is based on radio interferometric observations at the Multi-Element Radio Linked Interferometer Network (MERLIN) and the Very Large Array (VLA), as well as submillimeter interferometric observations at the IRAM Plateau de Bure Interferometer (PdBI). Submillimeter and 1.4 GHz observations, rather than rest-frame optical or near-IR, are chosen because they closely trace the star-forming regions of galaxies while being little affected by the old stellar light. The submillimeter is a

more direct tracer in this regard because it observes thermal emission from dust while the 1.4 GHz data probe synchrotron radiation from supernovae remnants, whose progenitors are short-lived massive stars and hence indirectly trace star-formation. Because of the radio-infrared relation within galaxies (e.g., Murphy et al., 2006), radio observations should give a valid measure of the size of the active region in a star forming galaxy. Ivison et al. (2010a) report that the IR-radio relation could evolve at high redshifts. However, their reported evolution law given by $(1+z)^{-0.15\pm0.3}$ is small and unlikely to affect significantly our estimation of IR-emitting region size using radio observations. Sargent et al. (2010), along with a recent result using *Herschel* by Ivison et al. (2010b), also found little or no evolution in the IR-radio relation at z < 2.

Although submillimeter transitions (e.g. CO) are more direct tracers of molecular clouds and star-forming regions than is radio emission, they tend to trace colder gas. In comparison, the star-forming regions in most local LIRGs and ULIRGs are sub-kpc in size (e.g., Condon et al., 1991). Thus the physical size given by submillimeter observation tends to be systematically larger than that of radio observations. Moreover, selection of high-redshift submillimeter galaxies will tend to result in a sample with colder SEDs, which are brighter in submillimeter wavelengths, and hence an inherently physically extended sample. This bias towards larger physical size should be more pronounced for the low–J CO transitions such as CO (1 – 0) and CO (2 – 1) and thus we will adopt sizes from higher–J CO transitions such as CO (3 – 2) and CO (6 – 5) if available. To be conservative, we will take the radio sizes to be the physical size of the star-forming region in galaxies and treat submillimeter sizes as upper limits to isolate this possible selection effect.

2.2.1.1 High-z Submillimeter Compilation

The submillimeter data were compiled from Tacconi et al. (2006), Tacconi et al. (2010), and Daddi et al. (2010). These authors used the IRAM PdBI to study submillimeter-selected samples using CO transitions with 0'.6 to \sim 1'.0 resolution. Tacconi et al. (2006) observed six SMGs, including four sources from Greve et al. (2003) and Neri et al. (2003), and two new sources at redshifts 2.2 < z < 3.4. Their observations yield four resolved SMGs with a median FWHM diameter of ~ 4 kpc. One of the Tacconi et al. (2006) sources needs to be excluded because its radio emission is significantly stronger than predicted by the IR-radio relation, indicating the presence of an AGN. Tacconi et al. (2010) reported the physical sizes (effective CO diameters) of two sources in the Extended Groth Strip at redshifts $z \sim 1.1$ to be 13 and 16 kpc in diameter, which they have found to be smaller but consistent with the size based on an I-band observation. It should be noted that although Tacconi et al. (2006) find the SMGs to be "compact", they still generally are a factor of 100 larger in area than local ULIRGs of similar IR luminosities. Additionally, Daddi et al. (2010) reported sizes of four BzK-selected $z \sim 1.5$ starforming galaxies (one member of this sample also has 1.4 GHz size measurement from Casey et al. (2009), which we adopt in preference to the CO data). In total we have eight data points from the submillimeter observations; three from Tacconi et al. (2006), two from Tacconi et al. (2010), and three from Daddi et al. (2010). IR luminosities for these eight galaxies were estimated via the Rieke et al. (2009) formalism based on 24 μ m fluxes from Hainline et al. (2009), Menéndez-Delmestre et al. (2009), and *Spitzer* deep imaging in Great Observatories Origins Deep Survey (GOODS, Dickinson et al., in prep.).

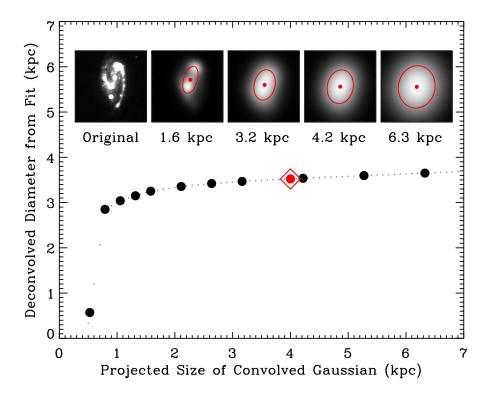


Figure 2.1: To determine the physical size of star-forming regions consistently for both local and high-redshift galaxies, we need to degrade the image of local galaxies to resolution similar to that observed at high-redshift. We convolve local images with a Gaussian beam of 4 kpc at the galaxy's distance and fit the convolved images to estimate the deconvolved diameters. A typical case, NGC 3627, is shown here with the original *Spitzer* 24 μ m image at the left panel of the inset. Subsequently we show the convolved images with the corresponding sizes of the convolved Gaussian beam and the 2D Gaussian fits to the convolved images overplotted as ellipses. This example demonstrates that the estimated deconvolved size is relatively insensitive to the choice of Gaussian used to convolve the original image.

2.2.1.2 High-z Radio Compilation

The 1.4 GHz radio observations were drawn from Chapman et al. (2004); Muxlow et al. (2005); Biggs & Ivison (2008) and Casey et al. (2009). Chapman et al. (2004) used MERLIN+VLA with 0''3 resolution to study 12 SMGs selected from the HDF at a median redshift of $z=2.2\pm0.2$. 8/12 of their targets were resolved with an effective median diameter measured above the 3σ contour of 7.0 ± 1.0 kpc. Biggs & Ivison (2008) used MERLIN+VLA to observe 12 SMGs in the Lockman Hole at 1.2 < z < 2.7 with 0''2 - 0''5 resolution (all sources were resolved). The sample was selected from SMGs found by surveys carried out with SCUBA and MAMBO (Scott et al., 2002; Greve et al., 2004; Coppin et al., 2006). Biggs & Ivison (2008) reported physical sizes of these SMGs ranging from 1-8 kpc with a median of 5 kpc. Lastly, Casey et al. (2009) used MERLIN (0''3 - 0''5 resolution) to observe seven ULIRGs and a HyLIRG selected by optical and radio color criteria from GOODS and the Lockman Hole at redshifts 0.9 < z < 2.4. They resolved all eight and report an average physical diameter of 5.0 ± 1.2 kpc, corresponding to the surface area within the 3σ detection level.

Muxlow et al. (2005) used MERLIN+VLA to conduct a deep 1.4 GHz survey of the HDF and Hubble Flanking Field (HFF) and studied 92 radio sources at 0.18 < z < 4 with 0''2-0''5 resolution. All but one source was resolved. For this study, we exclude sources that Muxlow et al. (2005) classified as AGN or AGN candidates. We also exclude the Muxlow sources that are observed only by the VLA and hence have lower resolution that may affect the accuracy of size estimates, as well as those with complex morphology such that their size estimation requires visual inspection (Muxlow et al., 2005; Thrall et al., 2007). Out of 92 objects from the Muxlow et al. (2005) sample, 72 have spectroscopic redshifts and 27 pass the aforementioned criterion and have a 24 μ m counterpart in GOODS. Muxlow et al.

(2005) reported sizes in terms of the largest angular size determined by Gaussian fitting (Thrall et al., 2007). Taking the largest angular size, which is the size of the major axis, as the diameter directly would overestimate the surface area; we assume that the sizes of the minor axes of these galaxies are 0.6 of the major-axis (the largest angular FWHM) and then calculate the surface areas and circularized diameters for the Muxlow et al. (2005) sample as reported in Table 2.1. This value is an average ratio of minor-to-major axes of SMGs from the Biggs & Ivison (2008) sample. An average physical diameter for the Muxlow et al. (2005) sample is 4.5 kpc. $L({\rm TIR})$ for the Chapman et al. (2004), the Muxlow et al. (2005), and the Casey et al. (2009) samples in the GOODS field were estimated via the Rieke et al. (2009) formalism and the *Spitzer* 24 μ m imaging in GOODS. $L({\rm TIR})$ for the Biggs & Ivison (2008) and the Casey et al. (2009) samples in other fields are also estimated using the Rieke et al. (2009) formalism based on the 24 μ m fluxes reported by Ivison et al. (2007) and Casey et al. (2009).

Table 2.1. High-Redshift Compilation of Star-Forming Galaxies

R.A.	Decl.	Source	z	$S_{24}\mum$	$S_{1.4~\mathrm{GHz}}$	Diameter	References ^a
(J2000)	(J2000)			(μJy)	(μJy)	(kpc)	
10 51 46.61	57 20 33.4	RGJ105146.61+572033.4	2.383	298 ± 16	33.5 ± 5.8	4.2	7
10 51 51.69	57 26 36.1	SMMJ105151.69+572636.1	1.147	314 ± 24	106 ± 6	6.1	8, 11
10 51 54.19	57 24 14.6	RGJ105154.19+572414.6	0.922	510 ± 22	45.4 ± 6.3	4.0	7
10 51 55.47	57 23 12.8	SMMJ105155.47+572312.8	2.686	104 ± 14	51.0 ± 4.3	2.2	8, 11
10 51 58.02	57 18 00.3	SMMJ105158.02+571800.3	2.239	303 ± 32	92.3 ± 4.5	6.7	8, 11
10 51 59.90	57 18 02.4	RGJ105159.90+571802.4	1.047	738 ± 27	74.5 ± 5.6	5.4	7
10 52 01.25	57 24 45.8	SMMJ105201.25+572445.8	2.148	217 ± 16	78.9 ± 4.7	3.3	8, 11
12 35 49.44	62 15 36.8	SMM123549.44+621536.8	2.203	630	74.6 ± 9.5	2.5	2, 3, 6
12 36 07.13	62 13 28.6	J123607+621328	0.435	259 ± 6	80.1 ± 6.0	5.3	10, 12, 14
12 36 15.60	62 09 46.4	J123615+620946	1.263	101 ± 4	55.3 ± 9.7	5.2	10, 12, 14
12 36 16.15	62 15 13.7	SMMJ123616.15+621513.7	2.578	313 ± 7	53.9 ± 8.4	8.0	2, 10, 12, 14
12 36 17.07	62 10 11.2	J123617+621011	0.845	88 ± 6	65.3 ± 8.3	3.6	10, 12, 14
12 36 18.32	62 15 50.5	J123618+621550	1.870	330 ± 7	164.4 ± 6.9	2.6	10, 12, 14

Table 2.1 (cont'd)

R.A.	Decl.	Source	z	S ₂₄ μm	S _{1.4 GHz}	Diameter	References ^a
(J2000)	(J2000)			(μJy)	(μJy)	(kpc)	
12 36 19.46	62 12 52.6	J123619+621252	0.473	976 ± 12	65.3 ± 4.8	1.8	10, 12, 14
12 36 22.65	62 16 29.7	SMMJ123622.65+621629.7	2.466	414 ± 7	70.9 ± 8.7	9.7	2, 10, 12, 14
12 36 26.52	62 08 35.4	BzK-4171	1.465	142	34	11.3	9, 13
12 36 29.13	62 10 45.8	SMMJ123629.13+621045.8	1.013	724 ± 12	81.4 ± 8.7	6.6	1, 2, 10
12 36 30.02	62 09 23.7	J123630+620923	0.953	223 ± 6	41.1 ± 4.7	3.7	10, 12, 14
12 36 30.12	62 14 28.0	BzK-16000	1.522	183	19	10.9	9, 13
12 36 33.67	62 10 05.8	J123633+621005	1.016	581 ± 9	58.5 ± 9.1	7.5	10, 12, 14
12 36 34.45	62 12 12.9	J123634+621213	0.456	1290 ± 8	224.7 ± 10.9	5.4	10, 12, 14
12 36 34.49	62 12 41.0	J123634+621241	1.219	446 ± 5	201.1 ± 10.3	6.4	10, 12, 14
12 36 35.57	62 14 24.0	J123635+621424	2.011	1480 ± 10	76.0 ± 7.9	1.9	10, 12, 14
12 36 41.52	62 09 48.2	J123641+620948	0.518	433 ± 6	83.5 ± 8.1	2.9	10, 12, 14
12 36 45.89	62 07 54.1	RGJ123645.89+620754.1	1.433	369 ± 7	83.4 ± 9.8	4.2	7, 10
12 36 46.64	62 08 33.3	J123646+620833	0.971	982 ± 8	81.7 ± 5.1	4.9	10, 12, 14

Table 2.1 (cont'd)

R.A.	Decl.	Source	z	$S_{24}\mum$	$S_{\rm 1.4~GHz}$	Diameter	Referencesa
(J2000)	(J2000)			(μJy)	(μJy)	(kpc)	
12 36 49.68	62 13 12.9	J123649+621313	0.475	371 ± 10	59.3 ± 8.2	4.6	10, 12, 14
12 36 50.01	62 08 01.6	J123650+620801	0.559	223 ± 6	34.1 ± 8.1	3.5	10, 12, 14
12 36 51.11	62 10 30.8	J123651+621030	0.410	984 ± 9	86.8 ± 8.2	5.1	10, 12, 14
12 36 53.37	62 11 39.6	RGJ123653.37+621139.6	1.275	322 ± 6	86.7 ± 8.3	5.8	7, 10
12 36 55.73	62 09 17.4	J123655+620917	0.419	846 ± 9	78.3 ± 8.8	2.6	10, 12, 14
12 36 55.93	62 08 08.2	J123655+620808	0.792	832 ± 7	118.0 ± 5.6	4.1	10, 12, 14
12 36 59.92	62 14 50.1	J123659+621449	0.761	466 ± 5	42.1 ± 9.2	5.7	10, 12, 14
12 37 04.08	62 07 55.3	J123704+620755	1.253	497 ± 9	63.1 ± 10.2	6.5	10, 12, 14
12 37 05.88	62 11 53.7	J123705+621153	0.902	655 ± 8	49.4 ± 8.1	9.1	10, 12, 14
12 37 07.21	62 14 08.1	SMMJ123707.21+621408.1	2.484	235 ± 8	45.0 ± 7.9	7.3	2, 3, 10
12 37 08.32	62 10 56.0	J123708+621056	0.422	648 ± 7	66.8 ± 8.1	3.0	10, 12, 14
12 37 10.60	62 22 34.6	RGJ123710.60+622234.6	1.522	227 ± 39	38.3 ± 10.1	3.4	7
12 37 11.98	62 13 25.7	SMMJ123711.98+621325.7	1.992	225 ± 7	53.9 ± 8.1	6.9	1, 2, 10

Apparently there are two approaches in reporting galaxy sizes from the radio measurements: the deconvolved FWHM (Muxlow et al., 2005; Biggs & Ivison, 2008) and the circularized diameter enclosing the surface area of the $> 3\sigma$ radio detections (Chapman et al., 2004; Casey et al., 2009). Despite the methodological differences between these two approaches, they agree very well for the objects with overlapping observations, especially in the HDF where there are six such galaxies. This agreement is expected, since the area detected above 3σ is likely to be consistent with that of half-max power given the typical levels of signal to noise ratio in the observations. We also note a very good agreement of sizes from 1.4 GHz and CO (3-2) observations of a HDF object, SMMJ123707+6214SW, where observations from Muxlow et al. (2005) and Tacconi et al. (2006) overlap.

Although galaxies drawn from the aforementioned samples are likely dominated by star-forming activity, we independently confirm this by inspecting whether their ratio of 850 μ m and 1.4 GHz fluxes follows the IR-radio relation for starburst galaxies given by Rieke et al. (2009). Galaxies with radio flux significantly stronger than predicted by the IR-radio relation likely harbor radio-loud AGN. Indeed, we have found that the only two objects with $F_{850}/F_{1.4}\gg 2$ are the most compact objects in our compilation (consistent with AGN-domination) and thus we exclude these objects (SMMJ163650.43+405734.5 and SMMJ105207.49+571904.0). It is worth noting that this test is unnecessary for the Muxlow et al. (2005) sample, where both radio spectral slope and radio morphology are already employed to identify AGN and AGN candidates.

In total our compilation has 48 intermediate and high-redshift starburst galaxies with a median redshift of 1.0 and a median size of 5.1 kpc. Our primary sample comprises the 27 galaxies from Muxlow et al. (2005), which should provide an unbiased and complete sample, selected by radio flux alone. The results from

Table 2.1 (cont'd)

R.A. (J2000)	Decl. (J2000)	Source	z	S ₂₄ μm (μJy)	S _{1.4 GHz} (μJy)	Diameter (kpc)	Referencesa
12 37 13.58	62 16 03.7	J123713+621603	0.938	208 ± 6	61.2 ± 9.1	5.5	10, 12, 14
12 37 14.34	62 15 58.8	J123714+621558	0.567	155 ± 5	51	7.6	10, 12
12 37 16.58	62 16 43.2	J123716+621643	0.557	512 ± 6	79.1 ± 5.2	4.5	10, 12, 14
12 37 16.81	62 10 07.3	J123716+621007	0.411	583 ± 8	92.7 ± 9.3	3.0	10, 12, 14
12 37 21.45	62 13 46.1	J123721+621346	1.019	217 ± 6	41.6 ± 8.7	4.4	10, 12, 14
12 37 51.82	62 15 20.2	BzK-17999	1.414	230	34	6.4	9, 13
14 18 03.55	52 30 22.3	EGS 12007881	1.161	327.6		16	4, 13
14 20 05.43	53 01 15.5	EGS 13035123	1.115	571.3		13	4, 13
16 36 58.19	41 05 23.8	SMMJ163658.19+410523.8	2.454	330 ± 55	92 ± 16	3.2	2, 3, 5

^a1. Chapman et al. (2004), 2. Chapman et al. (2005), 3. Tacconi et al. (2006), 4. Tacconi et al. (2010), 5. Hainline et al. (2009), 6. Menéndez-Delmestre et al. (2009), 7. Casey et al. (2009), 8. Biggs & Ivison (2008), 9. Daddi et al. (2010), 10. GOODS *Spitzer* Legacy Data, Dickinson et al., in prep., 11. Ivison et al. (2007), 12. Muxlow et al. (2005), 13. Weiner, private comm., 14. Morrison et al. (2010)

the additional 21 galaxies are consistent with those from the Muxlow et al. (2005) observations.

2.2.2 Local Compilation

For local galaxies, there is no homogeneous set of radio or submillimeter images suitable for our needs. Therefore, we use two additional measures of the star formation rate, Paschen- α images (Alonso-Herrero et al., 2006) and images at 24 μ m from a number of sources. As with the radio, both measures are not strongly affected by extinction and are good tracers of star forming activity (e.g., Murphy et al., 2006; Calzetti et al., 2010). Although radio images of local galaxies have somewhat larger extent than these other indicators, the high surface brightness areas that would dominate the high-redshift measurement have very similar morphologies and sizes (Murphy et al., 2006).

The high redshift galaxies have limited structural information, typically equivalent to a FWHM from Gaussian fitting or deconvolution of the observed image, in which the galaxy is only modestly well resolved. The FWHM of the beam is typically 0''3 to 1''0. A 1''0 beam corresponds to a diameter of 5 kpc at z=0.4, 7.5 kpc at z=0.8, and 8.5 kpc at z=2. However, the images of local galaxies often provide many more resolution elements across the target. To put them on the same scale as the radio images at high redshift, we convolved them with a Gaussian beam, and then determined sizes by Gaussian fitting and deconvolution. We demonstrate with a typical case of local star-forming galaxy in Fig. 2.1 that this method yields a robust measurement of physical sizes for local galaxies.

Despite our efforts to put all the images on the same basis, a possible source of systematic error remains. An image with low signal to noise will tend not to go as far into the wings of the star-forming activity and hence there will be a tendency for a systematic reduction in the estimated FWHM with decreasing

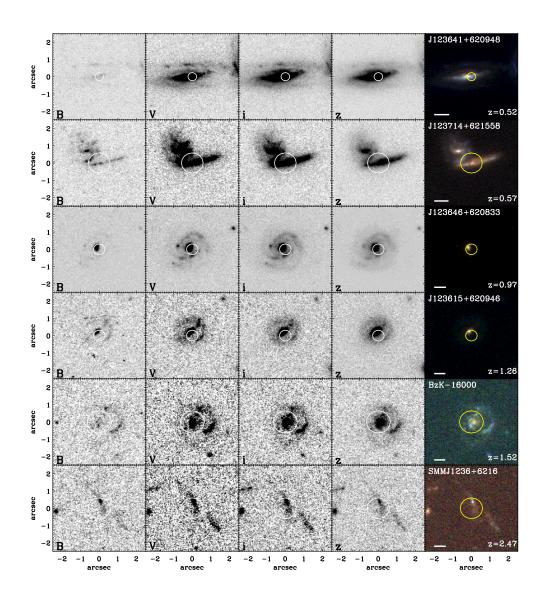


Figure 2.2: HST/ACS imaging of the subsample of our compilation in the GOODS field in B, V, i, and z. The circles indicate the size of the circularized diameter for the star-forming region in the corresponding galaxy. The bar at the lower left corner of the images in the right column represents a physical scale of 5 kpc. We found that $\sim 2/3$ of the subsample in GOODS display isolated, quiescent star-forming galaxies while a few cases show obvious signs of galaxy interaction as well as disturbed morphologies that can be associated with asymmetric clumps of star formation, especially at high-redshift.

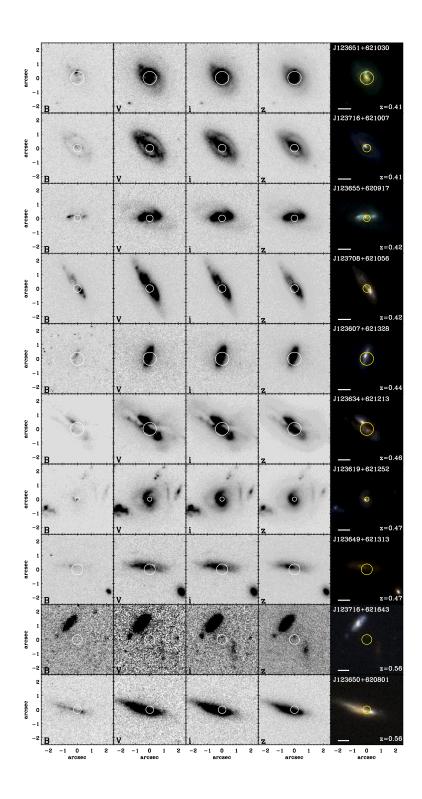


Figure 2.2 (continued)

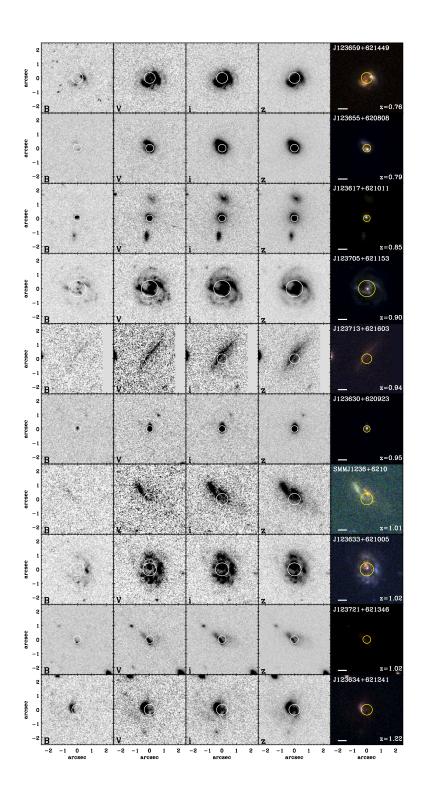


Figure 2.2 (continued)

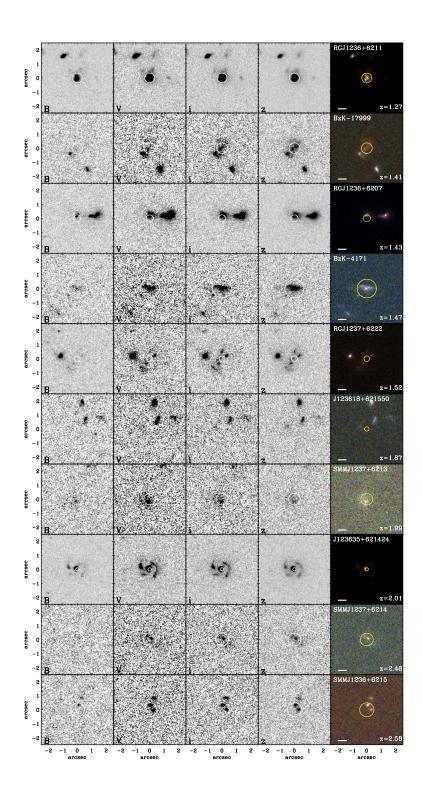


Figure 2.2 (continued)

signal to noise. Thus, the sizes of the high-redshift galaxies may be underestimated compared with the local ones. Since the major result of this paper is that the high-z galaxies have substantially larger sizes than local ones of similar luminosity, the result is that we may understate this conclusion, not that it would be undermined.

We describe our compilation of local IR galaxies in detail in the Appendix A. It comprises 19 normal star-forming galaxies ($L(\text{TIR}) \leq 10^{11} \ L_{\odot}$), 21 luminous IR galaxies (LIRG, $10^{11} \leq L(\text{TIR}) \leq 10^{12} \ L_{\odot}$), and 4 ultraluminous IR galaxies (ULIRG, $L(\text{TIR}) \geq 10^{12} \ L_{\odot}$).

2.2.3 HST Imaging of the High-Redshift Sample in the GOODS-N Field

Since 36 of 48 high-redshift galaxies in our sample are in the Hubble Deep Field imaged by the Great Observatories Origins Deep Survey (GOODS; Dickinson et al., in prep.) using the Advanced Camera for Survey (ACS) on the Hubble Space Telescope, we investigate the GOODS imaging (Version 2.0) of these galaxies in the B, V, i, and z bands. Details about the ACS observations of GOODS as well as the data can be found in Giavalisco et al. (2004) and at the survey's website¹.

GOODS optical images are used to confirm independently that the sizes and positions of the star-forming regions determined by radio or submillimeter observations are consistent with the high-resolution optical observations. The synthesized beam sizes of the radio and submillimeter observations are 0'2 - 0'5 while the optical imaging in GOODS/ACS has resolution at $\sim 0'.05/\text{pixel}$. Although the radio and submillimeter observations can constrain the size of the star formation regions without being affected by stellar emission, their interpretation benefits from high-resolution optical imaging, especially for morphological classifications. We illustrate the circularized size for the star-forming regions compared

¹http://www.stsci.edu/science/goods

to the optical extents of their host galaxies as seen in various optical filters in Fig. 2.2. The star-forming regions seen at radio and submillimeter wavelengths typically coincide with the central part of the optical structure, but there are a few cases where the star-forming region is at the collision interface of an interacting system (e.g. J123714+621558, J123716+621643). We will discuss our qualitative assessment of optical morphologies to address the structure of high-redshift star-forming galaxies in § 2.3.2.

2.3 Results

Our determinations of the physical sizes and luminosities for star-forming galaxies from the local sample out to the high-redshift SMGs are summarized in Fig. 2.6. We find the physical sizes of star-forming galaxies to be comparable within an order of magnitude across the entire IR luminosity $(10^9-10^{14}~L_{\odot})$ and redshift range (0 < z < 2.5). Local LIRGs and ULIRGs, however, are significantly smaller in size. It follows from Fig. 2.6 and is apparent from the diagram of $\Sigma_{\rm L(TIR)}$ as a function of $L({\rm TIR})$ in Fig. 2.7 that there is a correlation extending more than five orders of magnitude between $\Sigma_{\rm L(TIR)}$ and $L({\rm TIR})$. A linear fit to this correlation yields a formal slope of 0.9. However, given the inhomogeneity of the methods employed to estimate uncertainties in each of the subsamples comprising our compilation, we expect the uncertainty for this formal slope to encompass the slope of unity and hence suggest that the two parameters are proportional to each other.

Local LIRGs and ULIRGs have 1-4 orders of magnitude higher $\Sigma_{\rm L(TIR)}$ than indicated by this correlation suggesting that the starburst regions in these galaxies are not representative of their high-redshift counterparts of similar $L({\rm TIR})$. In fact, local ULIRGs with $L({\rm TIR}) \sim 10^{12}$ have a comparable $\Sigma_{\rm L(TIR)}$ to high-redshift

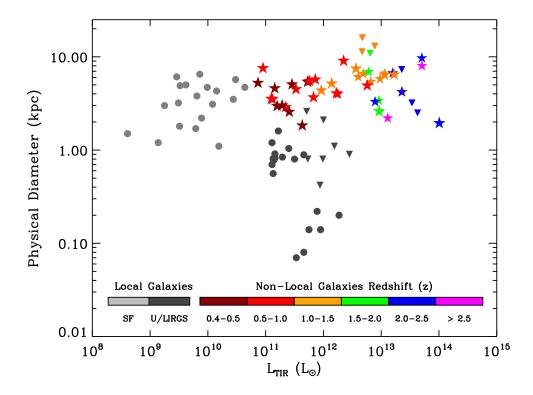


Figure 2.3: Physical sizes of star-forming galaxies at various redshifts and IR luminosities. Galaxies shown in color-coded stars and grey dots have diameters determined by radio observations (24 μ m for the local normal star-forming galaxies), while those shown in color-coded downward triangles and grey downward triangles have diameters determined with CO observations, which could yield systematically larger values (particularly for low–J CO transitions), the symbols signify upper limits in size. High-redshift LIRGs, ULIRGs, and SMG have similar sizes to local normal star-forming galaxies, while local LIRGs and ULIRGs are significantly smaller.

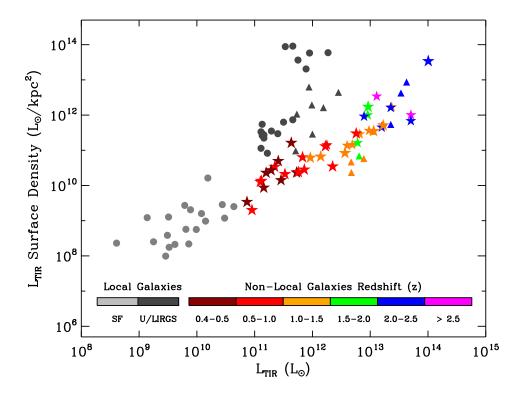


Figure 2.4: IR luminosity surface density, $\Sigma_{L(TIR)}$, as a function of IR luminosity for star-forming galaxies at various redshifts with the same color scheme as Fig. 2.6. The correlation seen in local starbursts and intermediate- and high-redshift LIRGs, ULIRGs, and SMGs indicates a general relationship in their conditions for star formation. On the other hand, local LIRGs and ULIRGs represent a different class of objects with star formation likely driven by some other process, such as galaxy interactions and mergers.

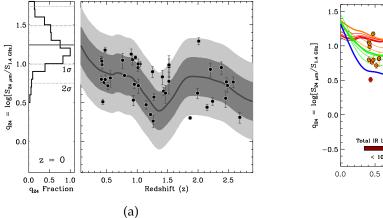
SMGs with $L(TIR) \sim 10^{14} L_{\odot}$.

2.3.1 Σ_{SFR} as a Tracer of Star-Forming Environment

The aforementioned correlation suggests an explanation for the strong aromatic emissions as well as the SEDs of star-forming galaxies at high redshift. If we assume that $\Sigma_{\rm SFR}$, and hence $\Sigma_{\rm L(TIR)}$, is an accurate indicator of the star-forming environment in starburst galaxies, Fig. 2.7 would suggest that $z\sim 1$ ULIRGs have similar environments to local LIRGs with an order of magnitude lower $L({\rm TIR})$, and likewise $z\sim 2$ SMGs have similar environments to local ULIRGs with two orders of magnitude lower $L({\rm TIR})$. We test this possibility with three independent approaches.

First, we compare the logarithmic ratio of $24~\mu m$ flux and $1.4~{\rm GHz}$ flux, $\log({\rm S}_{24}/{\rm S}_{1.4})$ or q_{24} , predicted by the SEDs of local LIRGs and ULIRGs and the observed flux ratio for high-redshift galaxies. At redshift 1 < z < 2.5 the *Spitzer* $24~\mu m$ observed bandpass probes rest-frame wavelengths of $7-12~\mu m$ and thus q_{24} at these redshifts is highly sensitive to emission from aromatic complexes, which are sensitive to the star formation environment. We first investigate the intrinsic scatter of q_{24} by considering the scatter observed locally derived from the *IRAS* and VLA observations, shown in Fig. 2.8. If we assume a similar scatter around the mean value of q_{24} and project this scatter to higher redshifts, Fig. 2.8 demonstrates that the observed scatter at high redshift is within the expected scatter based on local observations.

We then show in Fig. 2.8 that q_{24} for high-redshift galaxies is consistent with the ratios from local LIRGs and ULIRGs with significantly lower L(TIR). Consider the SMGs at $z\sim 2.4$ with $L(\text{TIR})\sim 10^{13.5}~L_{\odot}$; the correlation in Fig. 2.7 suggests their starburst environment to be similar to local ULIRGs with $L(\text{TIR})\sim 10^{12}~L_{\odot}$ and q_{24} is clearly inconsistent with the extrapolation for local ULIRGs



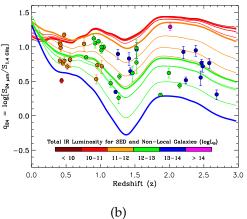


Figure 2.5: (a) The logarithmic ratio of 24 μ m and 1.4 GHz flux densities, q_{24} , for high-redshift star-forming galaxies (right panel, black dots) with the local distribution of q_{24} (left panel). The local distribution is from the IRAS Bright Galaxy Catalog (Sanders et al., 2003) and the NRAO VLA survey (Condon et al., 1998). The thick central line in the *right panel* shows the track of q_{24} predicted by the Rieke et al. (2009) SED for a galaxy with L(TIR) of $10^{12} L_{\odot}$, with dark and light grey shades showing the 1σ and 2σ extents assuming the local distribution of q_{24} . Despite a relatively large scatter, the distribution of q_{24} at intermediate and high redshifts broadly agrees with the scatter observed locally. (b) The logarithmic ratio of 24 μ m and 1.4 GHz flux densities, q_{24} , for high-redshift star-forming galaxies (right panel, black dots) with the local distribution of q_{24} (left panel). The local distribution is from the IRAS Bright Galaxy Catalog (Sanders et al., 2003) and the NRAO VLA survey (Condon et al., 1998). The thick central line in the right panel shows the track of q_{24} predicted by the Rieke et al. (2009) SED for a galaxy with $L({\rm TIR})$ of $10^{12}~L_{\odot}$, with dark and light grey shades showing the 1σ and 2σ extents assuming the local distribution of q_{24} . Despite a relatively large scatter, the distribution of q_{24} at intermediate and high redshifts broadly agrees with the scatter observed locally.

at $L(\text{TIR}) \sim 10^{13.5}~L_{\odot}$ while agreeing with the SED for $L(\text{TIR}) \sim 10^{12}~L_{\odot}$ local ULIRGs. Another way to interpret this is illustrated by Fig. 2.9 that the aromatic features are significantly stronger compared to local SED templates at redshifts greater than $z \sim 1$.

Second, we consider a result from Rigby et al. (2008), specifically their Fig. 3, that shows aromatic emissions for SMM J1635554.2+661225, a lensed SMG at z=2.516. This SMG has $L({\rm TIR})$ of $10^{11.9}~L_{\odot}$, which would be hardly detectable if not for the $22\times$ lensing magnification. The magnification also allows high signal-to-noise mid-IR spectroscopy with *Spitzer*, in which Rigby et al. (2008) found aromatic emission band shapes similar to those of NGC 2798 and to the average mid-IR spectra of 13 local normal starburst galaxies with average $L({\rm TIR})$ of $10^{10.7}~L_{\odot}$ (Brandl et al., 2006; Dale et al., 2007). This result is consistent with the relationship given in Fig. 2.7; high-redshift galaxies with $L({\rm TIR})$ of $\sim 10^{11.9}~L_{\odot}$ would have $\Sigma_{L({\rm TIR})}$ similar to local galaxies with an order of magnitude lower $L({\rm TIR})$.

Third, we compare a stacked mid-IR spectrum of $z\sim 1$ ULIRGs observed by Dasyra et al. (2009) with the local SEDs from Rieke et al. (2009). Fig. 2.7 suggests that the spectral features of local $L({\rm TIR})\sim 10^{11.1}~L_{\odot}$ galaxies should be similar to those for $z\sim 1$ ULIRGs with $L({\rm TIR})\sim 10^{12.3}~L_{\odot}$. We confirm this prediction in Fig. 2.10, where the stacked spectrum is indeed consistent with local LIRGs with $L({\rm TIR})$ of $\sim 10^{11.00}-10^{11.25}~L_{\odot}$ and clearly departs from the local SED for $\sim 10^{12.25}~L_{\odot}$ ULIRGs.

These tests support our hypothesis that $\Sigma_{L(TIR)}$ is a valid tracer for the star-burst environment and the observable spectral features. More importantly, they independently confirm that high-redshift star-forming galaxies, including SMGs, have similar star-forming environments to local normal star-forming galaxies and their higher star-formation rate is primarily due to higher Σ_{SFR} .

2.3.2 A Unified View of Star-Forming Galaxies

We believe from the nearly consistent sizes of local and high-redshift star-forming galaxies that the most significant evolution between these two populations is in the $\Sigma_{\rm SFR}$. In other words, while the sizes of these galaxies remain about the same, their star formation rate densities increase greatly from normal star-forming galaxies to SMGs.

Apart from many high-resolution observations of high-redshift SMGs that find them to be physically extended systems, recent observations of the 158 μ m [CII] line provide another probe into the environment of the star-forming regions. The [CII] line is an important cooling line for the photodissociation regions at the surfaces of molecular clouds. Combining this [CII] line with the CO (1-0) line yields a color-color diagram of $L_{\rm [CII]}/L_{\rm IR}$ vs. $L_{\rm CO(1-0)}/L_{\rm IR}$ that is sensitive to both the incident UV flux and the gas density. Hailey-Dunsheath et al. (2010) study the environment of the z=1.3 galaxy MIPS 1428 that has $L(TIR) \sim 10^{13} L_{\odot}$ and report that its $L_{\rm [CII]}/L_{\rm IR}$ is a factor of ~ 4 higher than for local ULIRGs while the $L_{CO(1-0)}/L_{IR}$ ratios are comparable, indicating a similar incident UV flux in both populations but that the gas density of MIPS 1428 is $\sim 100 \times$ lower than those in local ULIRGs. This behavior suggests a galaxy-wide starburst. Ivison et al. (2010c) apply this analysis using Herschel measurements, resulting in a similar finding for SMMJ2135 at z=2.3. The star-forming environments in these two high-redshift galaxies appear to be similar to M82 and other normal starburst galaxies rather than to local ULIRGs (Hailey-Dunsheath et al., 2010; Ivison et al., 2010c). SMMJ2135 is a particularly noteworthy case because it is lensed by $32\times$, which allowed Swinbank et al. (2010b) to observe it with the SMA at $0'3 \times 0'2$ resolution. They resolved the galaxy into four ~ 100 -pc massive star-forming regions distributed across the projected distance of 1.5 kpc, directly confirming

the distributed nature of the galaxy-wide star formation.

The optical morphologies of the subsample observed by GOODS, shown in Fig. 2.2, suggest that $\sim 2/3$ of the subsample are quiescent, normal galaxies and the other $\sim 1/3$ show signs of disturbed morphologies. The fraction of disturbed morphologies increases with redshift. However, only ~ 5 systems out of 36 can be identified positively as interacting systems, while the rest of those with disturbed morphologies could as well be due to instabilities fueled by rapid, asymmetric infall of gas resulting in large clumps of star-forming regions similar to those seen in SMMJ2135. Lehnert et al. (2009) also observed clumpy, galaxy-wide starbursts in 11 star-forming galaxies at $z\sim 2$ in rest-frame optical wavelengths. The optical surface brightnesses for their sample are more than an order magnitude greater than for local star-forming galaxies, consistent with our result.

The molecular gas and star formation relation, the Kennicutt-Schmidt Law (e.g. Schmidt, 1959; Kennicutt, 1998b), is shown by Genzel et al. (2010) to have a slope of 1.1 to 1.2 over a large range of stellar mass surface density ($10^{0.5}$ to $10^4~{\rm M_{\odot}pc^{-2}}$) for both low and high-redshift samples. A remarkable difference between low and high-redshift star-forming galaxies is that the gas depletion time increased from 0.5 Gyr at $z\sim2$ to 1.5 Gyr locally (Genzel et al., 2010), which is consistent with the picture that star-forming galaxies at low and high-redshift harbor similar star-forming environments but the gas consumption rate, and hence the star formation rate, is significantly higher at high-redshift.

The finding that the physical conditions in high-redshift galaxies' star-forming regions are similar to those in local quiescent star-forming galaxies indicates that their intense star formation is unlike the transient starbursting phase due to rapid infall of gas as a result of galaxy interaction, as seen in local ULIRGs. Rather they may represent an isolated evolution which could be observable for an extended

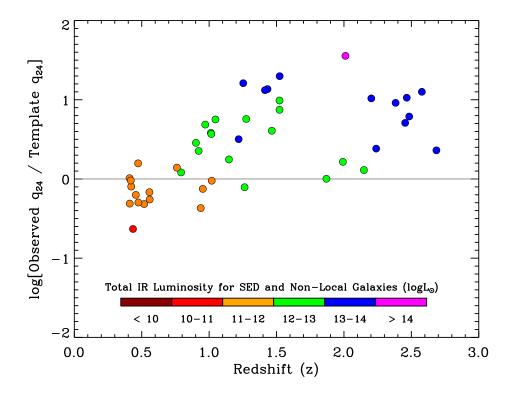


Figure 2.6: The logarithmic ratio of the observed 24 μ m and 1.4 GHz flux ratios and those predicted by the Rieke et al. (2009) SED templates based on local star-forming galaxies. Color coding represents the $L({\rm TIR})$ for each object as in Fig. 2.8. The increase of the ratios above $z\sim 1$ indicates that the aromatic emissions at this redshift range are stronger than expected based on local SED templates.

period of time. This picture is supported by the behavior of massive star-forming galaxies at high-redshift found in the cosmological simulations of Agertz et al. (2009) and Davé et al. (2010). The latter simulated populations with observational properties consistent with SMGs consists of isolated galaxies in the middle of large potential wells with large gas reservoirs. It should also be noted that Davé et al. (2010) report a highly asymmetric distribution of gas density, star formation, and velocity field in the simulated SMGs consistent with the disturbed morphologies observed.

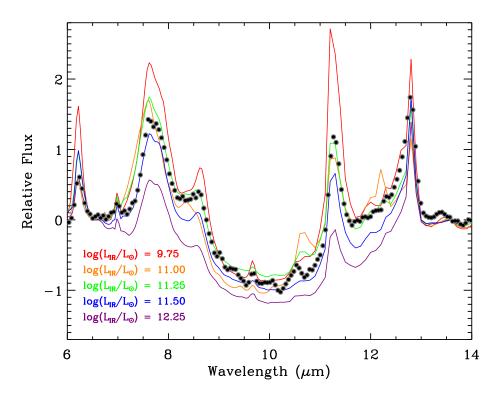


Figure 2.7: The stacked observed spectrum of high-redshift ULIRGs (black dots) with mean redshift and $L(\mathrm{TIR})$ of $z\sim 1$ and $10^{12.3}~L_{\odot}$, respectively, from Dasyra et al. (2009) compared to the local SED templates of Rieke et al. (2009) shown in color-coded lines. The relationship in Fig. 2.7 suggests that a spectrum of a local galaxy with $L(\mathrm{TIR})$ of $10^{11.1}~L_{\odot}$ would be an appropriate spectral description for a galaxy with $L(\mathrm{TIR})$ of $10^{12.3}~L_{\odot}$ at high-redshift. Indeed the emission features of the stacked spectra are consistent with the local galaxy templates with $L(\mathrm{TIR})$ of $10^{11.00}-10^{11.25}~L_{\odot}$, while departing significantly from the $L(\mathrm{TIR})=10^{12.25}~L_{\odot}$ template, despite the similar $L(\mathrm{TIR})$.

2.4 Chapter Conclusions

We made a compilation of physical size measurements for 44 local galaxies with $L({\rm TIR})$ ranging from normal star-forming galaxies at $10^9~L_{\odot}$ to ULIRGs at $>10^{12}$ L_{\odot} , as well as 48 intermediate and high-redshift galaxies, including SMGs.

Our compilation shows that (1) the physical scale of high-redshift ULIRGs and submillimeter galaxies is consistent within an order of magnitude with that of local normal star-forming galaxies (4.4 kpc in median diameter), while local LIRGs and ULIRGs are significantly smaller (0.8 kpc in median diameter); (2) there is a correlation of $L(\mathrm{TIR})$ and $\Sigma_{L(\mathrm{TIR})}$ extending over five orders of magnitude in $L(\mathrm{TIR})$ for normal star-forming galaxies and high-z galaxies. Local LIRGs and ULIRGs have significantly higher $\Sigma_{L(\mathrm{TIR})}$ than high-redshift galaxies with similar $L(\mathrm{TIR})$ and diverge from this correlation.

The fact that we do not find a significant deviation from this relationship in high-redshift galaxies with $L(\mathrm{TIR})$ in the ULIRG range indicates that the local ULIRGs as well as LIRGs belong to a rare population likely driven by a unique process. High-resolution studies of local ULIRGs have pointed out their disturbed morphology, double nuclei, and other signs of merger activity. The correlation we have found, however, suggests that the high $L(\mathrm{TIR})$ of SMGs and ULIRGs at large redshifts can be explained, to first order, by the higher Σ_{SFR} within isolated, quiescent galaxies.

We thank Anita Richards and Tom Muxlow for radio data in the HDF and insightful discussions; Scott Chapman for radio images from Chapman et al. (2004); Kalliopi Dasyra for spectra from Dasyra et al. (2009); Karín Menéndez-Delmestre for spectra published in Menéndez-Delmestre et al. (2009); Benjamin Weiner for his assistance with data compilation and valuable discussions. We also thank Henrik Spoon for his comments that helped us improve the manuscript. This

work is supported by contract 1255094 from Caltech/JPL to the University of Arizona. WR gratefully acknowledges the support from the Thai Government Scholarship.

CHAPTER 3

MID-INFRARED DETERMINATION OF TOTAL INFRARED LUMINOSITY AND STAR
FORMATION RATES OF LOCAL AND HIGH-REDSHIFT GALAXIES

We discuss the accuracy with which the total infrared luminosity, L(TIR), and star formation rate (SFR) of star-forming galaxies at redshift 0 < z < 2.8 can be estimated using single-band 24 μ m observations. By parameterizing the spectral energy distribution (SED) of galaxies as a function of their L(TIR) surface density, we have improved the accuracy of star-forming galaxy bolometric corrections. This method is based on indications that high-z IR luminous star-forming galaxies have extended star formting regions, in contrast to the strongly nuclear concentrated, merger-induced starbursts in local LIRGs and ULIRGs. We estimate L(TIR) using the improved bolometric corrections and compare with the L(TIR)measured with far-IR observations from Herschel, as well as those measured from stacked multi-band far-IR observations at redshift 0 < z < 2.8. Compared to the far-IR L(TIR) measurements, the single-band 24 μ m indicator predicts L(TIR)with a 0.02-dex average agreement; 0.12-dex overall scatter; and with 8% of objects disagreeing more than 0.2 dex. The Gaussian fit to the core distribution has a σ of 0.06 dex, suggesting that the great majority of IR galaxies at 0 < z < 2.8 are indeed much more physically extended than local counterparts of similar L(TIR). In our tests, AGNs were excluded using X-ray and $3.6-8.0~\mu m$ observations. Where these ancillary data are available, this approach therefore enables use of 24 μ m observations to provide the most sensitive unobscured tracer of SFR for star-forming galaxies across the peak of the cosmic star formation history, especially in the *JWST* era.

3.1 Introduction

The mid-infrared (mid-IR) is a unique window to study the evolution of star-forming galaxies, especially at redshift 1 < z < 3 where the cosmic star formation rate (SFR) peaks (e.g., Hopkins & Beacom, 2006). At these redshifts, a majority of star formation took place in obscured environments, where dust reprocesses the UV photons from hot young stars into IR emission (see e.g., Le Floc'h et al., 2005; Pérez-González et al., 2005; Dole et al., 2006; Buat et al., 2007). Star-forming galaxies at these redshifts also exhibit a large spread of extinction values and diverse dust distribution scenarios (Rujopakarn et al., 2012). These factors pose inherent challenges for optical and UV estimators of the SFR, which need to be complemented by IR techniques.

In the past decade, *ISO*, *Spitzer*, *WISE*, *AKARI*, and *Herschel* have allowed us to study star formation from the local Universe out to high z using mid-IR and far-IR observations. Measurements that determine the IR luminosity, L(TIR), from these missions trace the energy absorbed from UV photons emitted by short-lived massive stars (see e.g., Kennicutt, 1998). The most direct approach to measure L(TIR) is to use multi-band mid- and far-IR photometry. Recent examples use Herschel to observe star-forming galaxies at $100-500~\mu m$ and fit galaxy SEDs to measure L(TIR) (e.g., Elbaz et al., 2010; Rex et al., 2010; Elbaz et al., 2011). The complete characterization of the spectral peak of the dust emission provides a good measurement of L(TIR) and SFR. However, the requirement of multi-band photometry for far-IR SED fitting compromises this approach for faint galaxies whose detection is limited by confusion noise, particularly at the longer wavelengths (e.g., Condon, 1974; Dole et al., 2004b). A second approach is to use a monochromatic (single-band) IR luminosity to trace L(TIR) and SFR. Locally, rest-frame single-band 24 μm luminosity has been shown to be one of the best

tracers for L(TIR) and SFR (Calzetti et al., 2007; Rieke et al., 2009). Although the longer wavelengths, such as 70 μ m and 160 μ m, are closer to the peak of the thermal dust emission and thus reduce the size of the bolometric corrections, they are affected more by the cold dust heated by old stars, which increases scatter in the SFR calibration compared to estimates from 24 μ m (Rieke et al., 2009; Kennicutt et al., 2009), particularly in less luminous IR galaxies (Calzetti et al., 2010).

Beyond the local Universe, however, the redshifted 24 μ m band probes wavelengths containing the aromatic emissions (e.g., polycyclic aromatic hydrocarbons, hereafter PAH); the strongest PAH emission complexes at 6.2, 7.7, and 8.6 μ m (e.g., Smith et al., 2007) redshift into the 24 μ m band by $z \sim 2$. Although they help boost the 24 μ m flux and aid detection of galaxies at high z, PAHs pose two challenges to using single-band 24 μ m observations to estimate L(TIR) and SFR. First, the PAH emission is influenced by environment (e.g., UV radiation, optical depth), introducing a ~ 0.3 -dex scatter to the L(TIR) and SFR estimates (Calzetti et al., 2007). Second, the PAH emission appears to strengthen intrinsically at high z compared to that found in local galaxies with the same L(TIR) (Rigby et al., 2008; Farrah et al., 2008; Takagi et al., 2010). Therefore, the bolometric corrections to determine L(TIR) measured from local galaxies in the PAH wavelength regions will not be applicable at high z. Recent studies indicate that applying the local bolometric corrections to high-z galaxies will overestimate their L(TIR) and SFR by up to an order of magnitude. This is reported as the "mid-IR excess" in recent far-IR studies using Spitzer and Herschel (e.g., Papovich et al., 2007; Elbaz et al., 2010; Nordon et al., 2010; Barro et al., 2011; Nordon et al., 2012). The SED evolution causes a *systematic bias* that must be taken into account to use 24 μ m observations as L(TIR) and SFR indicators beyond the local Universe.

Out to $z\sim 2.8$, the *Spitzer* 24 μm observations probe weaker SFR at any given

redshift than is possible with other far-IR bands (see Figure 4 of Elbaz et al., 2011). For JWST, 21 μ m is the longest wavelength band suitable for deep cosmological surveys. Therefore, our understanding of star-forming galaxies at high z will depend critically on mid-IR SFR indicators, where the current state of the art prescription to estimate $L({\rm TIR})$ from single-band 24 μ m observations still presents a 0.4–dex scatter (Nordon et al., 2012). Additionally, the Spitzer 24 μ m data are already available from deep legacy surveys (e.g., GOODS, FIDEL, COSMOS, SpUDS), as well as from large-area surveys (e.g., SWIRE and the Boötes field) that will not be fully surveyed by current facilities to the same depth in terms of SFR. Exploration of means to reduce the current 0.4–dex scatter in $L({\rm TIR})$ estimates will allow utilization of the mid-IR observations to the fullest extent in the upcoming decade.

In this paper, we apply the results from our previous study, Rujopakarn et al. (2011), to take into account the the SED evolution of star-forming galaxies and refine the 24 μ m L(TIR) and SFR indicators. Rujopakarn et al. (2011) find that the IR luminosity surface density, $\Sigma_{L(TIR)}$, affords an accurate description of the SED and subsequently accurate bolometric corrections out to high z, specifically out to z=2.8, the farthest redshift where the Spitzer 24 μ m band traces predominantly PAH emissions. The measurement of $\Sigma_{L(TIR)}$ requires high-resolution imaging of unobscured star-forming regions, which are only available for a small number of galaxies. We use these galaxies as a tool to construct a simple formula to estimate L(TIR) and SFR using only single-band 24 μ m flux and redshift measurements, and then compare the resulting L(TIR) estimates with results using far-IR data.

This paper is organized as follows. We discuss the evolution of the SEDs of star-forming galaxies and the use of $\Sigma_{L(TIR)}$ as a guide to select the appropriate SED for high-z galaxies in Section 3.2. The derivation of the single-band L(TIR)

indicator is described in Section 3.3. We then compare the new $L({\rm TIR})$ indicator with other independent measurements in Section 3.4 and present the $L({\rm TIR})$ SFR indicator in Section 3.5. Lastly, we discuss the validity of rest-frame 8-24 $\mu{\rm m}$ as a tracer of $L({\rm TIR})$ and SFR, along with implications of our results in Section 3.6. Throughout this paper, we assume a $\Lambda{\rm CDM}$ cosmology with $\Omega_m=0.3$, $\Omega_{\Lambda}=0.7$, and $H_0=70~{\rm km~s^{-1}Mpc^{-1}}$. We follow the convention of Rieke et al. (2009) and adopt the definition of $L({\rm TIR})$ of Sanders & Mirabel (1996), although these studies defined $L({\rm TIR})$ slightly differently (i.e., $5-1000~\mu{\rm m}$ and $8-1000~\mu{\rm m}$), the resulting $L({\rm TIR})$ values are closely consistent. We will refer to galaxies with $L({\rm TIR})$ in the range of $10^{11}-10^{12}$ and those with $L({\rm TIR})>10^{12}$ L_{\odot} as Luminous Infrared Galaxies (LIRGs) and Ultraluminous Infrared Galaxies (ULIRGs), respectively, or collectively U/LIRGs.

3.2 Quantifying the IR SED Evolution

In this section, we will discuss the challenges in using *Spitzer* observations at 24 μ m to estimate L(TIR) and SFR. Major issues include the determination of an overall approach for using $\Sigma_{L(TIR)}$ as an indicator of a galaxy SED (Section 3.2.1), and the choice of SED library (Section 3.2.2).

3.2.1 $\Sigma_{L(TIR)}$ as an Indicator of SEDs for Star-Forming Galaxies

Until now, most estimations of the $L({\rm TIR})$ and SFR of galaxies using single-band IR observations rely on an assumption that the SED of a star-forming galaxy does not evolve with redshift, i.e., that bolometric corrections measured from local SED templates can be applied to high-z galaxies. However, local IR galaxies, from which we construct the SED libraries, comprise an inhomogeneous population of both normal star-forming galaxies (quiescent disks) and those with nuclear star-formation induced by galaxy interactions. The contribution of interaction-

induced star formation increases with $L({\rm TIR})$; locally, theoretical studies suggest that ULIRGs must be dominated by interaction-induced starbursts to achieve their of $L({\rm TIR})$ outputs (Hopkins et al., 2010), which is consistent with observations (e.g., Veilleux et al., 2002). The application of local bolometric corrections to high-z galaxies thus carries an implicit assumption that high-z star-forming galaxies are likewise dominated by interaction-induced starbursts.

Observations have shown, however, that actively star-forming galaxies at high z are different from their local counterparts in at least three major aspects. First, the IR SEDs at high z exhibit colder far-IR dust temperatures, T_d , than local galaxies at fixed L(TIR) (Pope et al., 2006; Symeonidis et al., 2009; Muzzin et al., 2010). These galaxies have dust temperatures similar to local galaxies with lower L(TIR). Second is the aforementioned evolution of the strength of the aromatic features, which grow stronger at high z at a fixed L(TIR). Quantitatively, for instance, Rigby et al. (2008) found Abell 2218a, a galaxy with L(TIR) of $10^{11.9}$ L_{\odot} at z=2.5, to exhibit aromatic emission features virtually identical to those of a local galaxy with an order of magnitude lower L(TIR).

Third, Rujopakarn et al. (2011) found that the diameters of the galactic-wide star-forming regions in high-z U/LIRGs are $10-30\times$ larger than those of local U/LIRGs at the same L(TIR). The extent of the star formation found in high-z U/LIRGs is similar to that of local normal star-forming galaxies (sub-LIRG), 4-10 kpc in diameter, but with Σ_{SFR} scaled up by a factor of $100-1000\times$ (Figures 3 and 4 of Rujopakarn et al., 2011). This structural similarity is a manifestation of the "main sequence" of star-forming galaxies, originally defined as a sequence of galaxies in stellar mass vs. SFR space (Noeske et al., 2007), where star-formation occurs at a relatively steady rate rather than in bursts, and in disks or clumps, rather than in merger nuclei (e.g., Genzel et al., 2010; Tacconi et al., 2010;

Narayanan et al., 2010; Daddi et al., 2010b; Elbaz et al., 2010, 2011). In its simplest form, this picture suggests that these galaxies differ among themselves (and from local lower luminosity star-forming galaxies) primarily in the SFR surface density, $\Sigma_{\rm SFR}$, and hence in IR luminosity surface density, $\Sigma_{\rm L(TIR)}$.

In Figure 3.1, adapted from Figure 4 of Rujopakarn et al. (2011), we show $\Sigma_{\rm L(TIR)}$ as a function of $L({\rm TIR})$ along with trend lines describing the relationship in each population, one for local galaxies with $L({\rm TIR})$ above $10^{11}~L_{\odot}$ and another for high-z galaxies. The main sequence can be drawn in this figure from the local normal star-forming galaxies (sub-LIRG galaxies) onto the high-z star-forming galaxies. Both the local and high-z relationships agree below $L({\rm TIR}) \sim 10^{11}~L_{\odot}$. The trends diverge above the LIRG threshold, where the local galaxy sample starts to be dominated by galaxies harboring interaction-induced star formation (see also Totani et al. (2011) for the local relationship).

Rujopakarn et al. (2011) estimated $\Sigma_{\rm L(TIR)}$, defined by $\Sigma_{\rm L(TIR)} = L({\rm TIR})/A$, by measuring the area, A, of the IR-emitting region using radio continuum (e.g., 1.4 GHz), Paschen- α , and 24 μ m observations. Although the emission physics of these size measures is different, they trace a highly consistent physical extent of the star-forming regions and are similarly insensitive to contributions from old stellar populations. Paschen- α and 24 μ m are the two best IR tracers of SFR and are emitted from approximately the same spatial extent. Also, Chanial et al. (2007) found that radio continuum (e.g., 1.4 GHz) and far-IR size measurements are consistent within 15% (their equation 1). For the purpose of determining the surface area of star formation in individual galaxies, we will thus use these three size tracers interchangeably. Among these indicators, only the interferometric observation of the radio synchrotron continuum can resolve individual galaxies at high-z. The main sample of high-z galaxies in the Figure 3.1 was therefore from

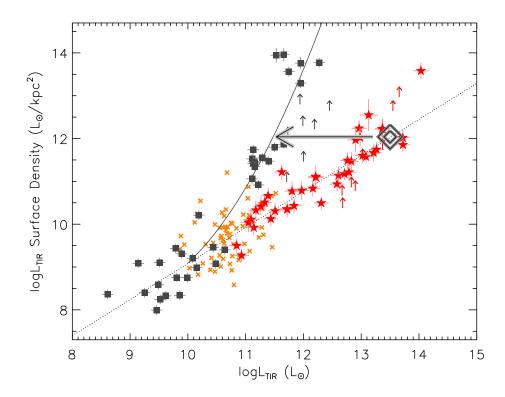


Figure 3.1: The relationships between the L(TIR) and L(TIR) surface density, $\Sigma_{L(\text{TIR})}$, differ for the local and non-local galaxies (grey squares and red stars, respectively). Local galaxies from Chanial et al. (2007) are shown for comparison as orange crosses. The upward arrows represent points derived from CO size measurement, which could be systematically more extended than the other size tracers employed (Rujopakarn et al., 2011) and thus are taken as lower limit in $\Sigma_{L(\text{TIR})}$. The solid and dashed lines are the fits for local and high-z galaxies (excluding the CO lower limits), respectively. Rujopakarn et al. (2011) show that the SEDs of galaxies are to first order indicated solely by their $\Sigma_{L(\text{TIR})}$. For example, a high-z galaxy with L(TIR) of $10^{13.5}$ L_{\odot} will have aromatic emissions and absorption features consistent with a local galaxy with the same $\Sigma_{L(\text{TIR})}$, indicated by the arrow, in this case a local galaxy with L(TIR) of $\sim 10^{11.5}$ L_{\odot} (see Section 3.3). This behavior, plus the tendency of the great majority of high-z galaxies to lie near the main sequence allows a simple approach to associating the appropriate SED with typical high-z galaxies.

the Muxlow et al. (2005) 1.4 GHz VLA+MERLIN survey of the Hubble Deep Field with angular resolution of 0'2-0'5. This is a blind survey that has resolved virtually all of the 92 detected galaxies, which assures that the extended physical sizes at high z are not due to selection bias. The Muxlow et al. sample is augmented by radio observations of sub-mm galaxies from the literature with similarly high angular resolutions. The sample of galaxies with physical size measurements is tabulated in Table 3.1 and 3.2 for the local and high-z samples, respectively.

Table 3.1. Local Galaxies with $\Sigma_{L(\mathrm{TIR})}$ Measurement

ID	IRAS ID	Distance ^a	Diameter	$L(TIR)^{a}$	$\Sigma_{ m L(TIR)}$	$\sigma\Sigma_L$	Ref.b
		Mpc	kpc	$\log(L_{\odot})$	$\log(L_{\odot}/$	kpc ²)	•
							_
NGC2976	F09431+6809	3.8	1.5	8.61	8.36	0.11	1
NGC4826	F12542+2157	6.0	1.2	9.14	9.09	0.11	1
NGC2403	F07320+6543	3.8	3.0	9.25	8.40	0.11	1
NGC925	F02242+3321	9.8	6.1	9.46	7.99	0.11	1
NGC1512		11.3	3.2	9.49	8.58	0.11	1
NGC5866	F15051+5557	13.0	1.8	9.51	9.10	0.11	1
NGC2841		10.5	4.9	9.52	8.24	0.11	1
NGC4559	F12334+2814	11.9	5.0	9.62	8.33	0.11	1
NGC4736	12485+4123	5.7	1.7	9.79	9.43	0.11	1
NGC3198	F10168+4547	14.7	3.8	9.81	8.76	0.11	1
NGC3184	10152+4140	11.9	6.5	9.86	8.34	0.11	1
NGC3351	F10413+1157	10.8	2.2	9.89	9.31	0.11	1
NGC3938	F11502+4423	13.1	4.7	9.99	8.75	0.11	1
NGC4569	F12343+1326	17.8	3.1	10.08	9.20	0.11	1
NGC5055	F13135+4217	8.4	4.3	10.15	8.99	0.11	1
NGC5033	F13111+3651	14.7	1.1	10.19	10.21	0.11	1
NGC3627	F11176+1315	9.3	3.5	10.44	9.46	0.11	1
NGC5194	F13277+4727	8.8	5.7	10.48	9.07	0.11	1
NGC7331	F22347+3409	16.2	4.7	10.64	9.40	0.11	1
NGC23	F00073+2538	63.9	1.2	11.11	11.06	0.11	2
NGC6701	F18425+6036	60.6	0.7	11.11	11.52	0.11	2

Table 3.1 (cont'd)

ID	IRAS ID	Distance ^a	Diameter	$L(TIR)^{a}$	$\Sigma_{ m L(TIR)}$	$\sigma \Sigma_L$	Ref. ^b
		Mpc	kpc	$\log(L_{\odot})$	$\log(L_{\odot}$	'kpc ²)	-
UGC1845	F02208+4744	66.4	0.8	11.13	11.42	0.11	2
NGC5936	F15276+1309	65.1	0.6	11.13	11.74	0.11	2
MCG+02-20-003	F07329+1149	72.4	0.8	11.14	11.46	0.11	2
NGC2369	F07160-6215	47.1	0.8	11.16	11.44	0.11	2
ESO320-G030	F11506-3851	40.4	0.9	11.16	11.35	0.11	2
IC5179	F22132-3705	50.0	1.6	11.22	10.92	0.11	2
NGC2388	F07256+3355	61.9	0.8	11.29	11.55	0.11	2
NGC7771	F23488+1949	61.2	1.0	11.40	11.47	0.11	2
MCG+12-02-001	F00506+7248	68.9	0.8	11.50	11.80	0.11	2
	F03359+1523	146.9	0.1	11.53	13.94	0.17	3
NGC1614	F04315-0840	67.1	0.9	11.66	11.87	0.11	4
UGC2369	F02512+1446	130.7	0.1	11.66	13.96	0.16	3
Arp236	F01053-1746	84.2	2.6	11.71	10.98	0.11	4
Arp193	F13182+3424	107.1	0.8	11.73	12.03	0.11	4
UGC4881	F09126+4432	172.7	0.1	11.75	13.56	0.12	3
Arp299	F11257+5850	51.2	0.4	11.94	12.80	0.11	4
	F17132+5313	218.9	0.1	11.95	13.76	0.15	3
	F15163+4255	180.8	0.2	11.95	13.29	0.11	3
	F10565+2448	188.9	0.8	11.99	12.29	0.11	4
VIIZw31	F05081+7936	230.2	2.1	12.00	11.46	0.11	5
	F23365+3604	269.8	1.1	12.19	12.21	0.11	5

Table 3.1 (cont'd)

ID	<i>IRAS</i> ID	Distance ^a	Diameter	$L(TIR)^{a}$	$\Sigma_{ m L(TIR)}$	$\sigma \Sigma_L$	Ref. ^b
		Mpc	kpc	$\log(L_{\odot})$	$\log(L_{\odot}/$	kpc ²)	
Arp220	F15327+2340	85.6	0.2	12.27	13.77	0.11	6
	F17207-0014	188.2	0.9	12.45	12.65	0.10	4

^aDistance and L(TIR) from Sanders et al. (2003) and adjust to match our cosmology.

^bDiameters references 1. measured from *Spitzer* MIPS 24 μ m imaging taken by SINGS (Calzetti et al., 2007, e.g.,), 2. measured from *Hubble* NIC-MOS Pa- α taken by Alonso-Herrero et al. (2006), 3. 8.4 GHz radio sizes given by Condon et al. (1991), 4. CO (3 – 2) sizes given by Iono et al. (2009), 5. CO (2 – 1) or CO (1 – 0) sizes given by Downes & Solomon (1998), 6. 5 GHz radio size based on Rovilos et al. (2003).

Note. — Reproduced from Table 2 of Rujopakarn et al. (2011). Uncertainties in $L(\mathrm{TIR})$ estimates are dominated by distance measurement uncertainties, which are not published in the Sanders et al. (2003) catalog; we use error bars of 0.1 dex for $L(\mathrm{TIR})$ - $\Sigma_{L(\mathrm{TIR})}$ parameterizations fitting and to estimate the $\sigma\Sigma_L$.

Table 3.2. High-z Galaxies with $\Sigma_{\rm L(TIR)}$ Measurement

ID	z	Diameter	$L(\mathrm{TIR})_{\mathrm{old}}$	σL	$\Sigma_{ m L(TIR)}$	$\sigma\Sigma_L$	Ref. ^a
		kpc	$\log(L_0)$	_☉)	$\log(L_{\odot})$	/kpc ²)	
RGJ105146.61+572033.4	2.383	4.2	13.37	0.135	12.23	0.247	3
SMMJ105151.69+572636.1	1.147	6.1	12.60	0.139	11.14	0.209	4,5
RGJ105154.19+572414.6	0.922	4.0	12.21	0.132	11.11	0.253	3
SMMJ105155.47+572312.8	2.686	2.2	13.13	0.157	12.55	0.372	4,5
SMMJ105158.02+571800.3	2.239	6.7	13.21	0.146	11.67	0.203	4,5
RGJ105159.90+571802.4	1.047	5.4	12.83	0.132	11.47	0.213	3
SMMJ105201.25+572445.8	2.148	3.3	12.90	0.138	11.97	0.295	4,5
J123607+621328	0.435	5.3	10.84	0.131	9.50	0.164	6, 7, 8
J123615+620946	1.263	5.2	12.16	0.133	10.84	0.194	6, 7, 8
SMMJ123616.15+621513.7	2.578	8.0	13.72	0.131	12.02	0.176	2, 6, 7, 8
J123617+621011	0.845	3.6	11.05	0.135	10.04	0.229	6, 7, 8
J123618+621550	1.870	2.6	12.96	0.131	12.24	0.181	6, 7, 8
J123619+621252	0.473	1.8	11.62	0.130	11.22	0.183	6, 7, 8
SMMJ123622.65+621629.7	2.466	9.7	13.72	0.130	11.85	0.160	2, 6, 7, 8
SMMJ123629.13+621045.8	1.013	6.6	12.71	0.130	11.18	0.143	1, 2, 6
J123630+620923	0.953	3.7	11.80	0.131	10.77	0.223	6, 7, 8
J123633+621005	1.016	7.5	12.58	0.130	10.94	0.165	6, 7, 8
J123634+621213	0.456	5.4	11.72	0.130	10.36	0.144	6, 7, 8
J123634+621241	1.219	6.4	13.08	0.130	11.58	0.138	6, 7, 8
J123635+621424	2.011	1.9	14.03	0.130	13.58	0.195	6, 7, 8
J123641+620948	0.518	2.9	11.33	0.130	10.51	0.173	6, 7, 8

Following the Rujopakarn et al. (2011) example, the use of $\Sigma_{\rm L(TIR)}$ as an indicator of SED features can be illustrated by envisioning a horizontal line at a fixed $\Sigma_{\rm L(TIR)}$ in Figure 3.1. As an example, we assume the z=2.5 Abell 2218a with $L({\rm TIR})$ of $10^{11.9}~L_{\odot}$, observed by Rigby et al. (2008), is located on the mainsequence. We then expect it to have spectral features consistent with a galaxy on the local sequence with $L({\rm TIR})$ of $\sim 10^{10.9}~L_{\odot}$ that has the same $\Sigma_{\rm L(TIR)}$. Rujopakarn et al. (2011) further demonstrate the ability of $\Sigma_{\rm L(TIR)}$ to predict SED behavior by predicting the 24 μ m-to-1.4 GHz flux ratios, which are sensitive to PAH features at $z\sim 2$, consistently with the observed ratios (their Figure 5), as well as matching the average observed aromatic spectrum of high-z ULIRGs to a local SED template (their Figure 7). The assumption that $\Sigma_{\rm L(TIR)}$ is the dominant parameter controlling the average SED thus provides a tool to assign an appropriate local SED template to represent the SED of high-z galaxies, a result we will use to construct an indicator for $L({\rm TIR})$ and SFR in this work.

The $\Sigma_{\rm L(TIR)}$ method is physically motivated because the PAH emission emerges from the outer surfaces of the photodissociation regions (PDRs; e.g., Tielens, 2008), so the surface density of the SFR is a controlling factor for the PAH-emitting surface area and thus the PAH emission strength. Additionally, Chakrabarti & McKee (2005) modeled the radiative transfer in centrally heated dusty sources and found a general relation among the luminosity-to-mass ratio, the surface density, and the shape of the SED. They predict that the behavior of SED templates for local galaxies might not extend to high z. Extended sizes and colder SEDs were also shown to be connected through a T_d - $\Sigma_{\rm L(TIR)}$ relation explored by Chanial et al. (2007), who theoretically described the IR-emitting region of a star-forming galaxy as an isothermal cloud optically thick to optical wavelengths and optically thin in the IR. Chanial et al. (2007) show that $L({\rm TIR})$, T_d , and the ex-

Table 3.2 (cont'd)

ID	z	Diameter	$L(\mathrm{TIR})_{\mathrm{old}}$	σL	$\Sigma_{ m L(TIR)}$	$\sigma \Sigma_L$	Ref. ^a
		kpc	$\log(L_0)$	⊙)	$\log(L_{\odot})$	/kpc²)	
RGJ123645.89+620754.1	1.433	4.2	13.36	0.131	12.22	0.193	3, 6
J123646+620833	0.971	4.9	12.76	0.130	11.49	0.192	6, 7, 8
J123649+621313	0.475	4.6	11.14	0.131	9.92	0.179	6, 7, 8
J123650+620801	0.559	3.5	11.09	0.131	10.11	0.213	6, 7, 8
J123651+621030	0.410	5.1	11.44	0.130	10.13	0.165	6, 7, 8
RGJ123653.37+621139.6	1.275	5.8	13.02	0.131	11.60	0.168	3, 6
J123655+620917	0.419	2.6	11.39	0.130	10.66	0.181	6, 7, 8
J123655+620808	0.792	4.1	12.22	0.130	11.09	0.167	6, 7, 8
J123659+621449	0.761	5.7	11.84	0.130	10.43	0.174	6, 7, 8
J123704+620755	1.253	6.5	13.26	0.131	11.74	0.174	6, 7, 8
J123705+621153	0.902	9.1	12.31	0.130	10.49	0.152	6, 7, 8
J123708+621056	0.422	3.0	11.26	0.130	10.42	0.211	6, 7, 8
RGJ123710.60+622234.6	1.522	3.4	12.98	0.171	12.02	0.237	3
SMMJ123711.98+621325.7	1.992	6.9	12.79	0.132	11.22	0.197	1, 2, 6
J123713+621603	0.938	5.5	11.72	0.131	10.34	0.183	6, 7, 8
J123714+621558	0.567	7.6	10.93	0.131	9.27	0.154	6, 8
J123716+621643	0.557	4.5	11.51	0.130	10.31	0.187	6, 7, 8
J123716+621007	0.411	3.0	11.18	0.130	10.33	0.211	6, 7, 8
J123721+621346	1.019	4.4	11.97	0.131	10.79	0.210	6, 7, 8

^a1. Chapman et al. (2004), 2. Chapman et al. (2005), 3. Casey et al. (2009), 4. Biggs & Ivison (2008), 5 Ivison et al. (2007) 6. GOODS *Spitzer* Legacy Data, Dickinson et al., in prep., 7. Muxlow et al. (2005), 8. Morrison et al. (2010)

Note. — Reproduced from Table 1 of Rujopakarn et al. (2011) with omission of objects whose diameters were measured with CO observations, which are excluded from the fit in Section 3.3.

tent of the IR-emitting region are related by a fundamental plane; the L(TIR)- T_d relation (e.g., Soifer et al., 1987) is a manifestation thereof.

3.2.2 The Local Reference for the Galaxy SEDs

The SED libraries most commonly used to represent the spectra of star-forming galaxies are those of Chary & Elbaz (2001), Dale & Helou (2002), and Rieke et al. (2009). The former two libraries were based on spectra taken by *ISO*, preceding the availability of full spectral coverage at $6.3-24~\mu m$, which the $24~\mu m$ band probes at redshift z=2.8-0. The recent infrared spectrograph (IRS) observations from *Spitzer*, covering $5.2-38~\mu m$, show that the Chary & Elbaz (2001) SED templates (hereafter, CE01) have suppressed aromatic features at very high luminosity (Chary & Pope, 2010), but, to a greater extent, do not sufficiently take into account the strong silicate absorption features at $10~\mu m$, resulting in weaker aromatic bands but stronger net emission in the PAH-region comparing to observed galaxies (Armus et al., 2007; Rieke et al., 2009). The Dale & Helou (2002) SED library is optimized to describe moderately-luminous local star-forming galaxies with $L(TIR) < 10^{11}~L_{\odot}$ and hence the lack of silicate absorption becomes more significant at higher L(TIR) with larger typical extinction.

Rieke et al. (2009) developed SED templates (hereafter, R09), which we adopt as the SED reference for local galaxies, separately for normal star-forming galaxies (sub-LIRG) and U/LIRGs to provide a final SED library covering L(TIR) of $10^{9.75}$ to $10^{13.00}~L_{\odot}$. The U/LIRGs SED templates were constructed from a sample of 11 local LIRGs and ULIRGs with high quality *Spitzer* IRS spectra as well as photometric data covering optical to radio wavelengths (see Figures 1, 2, and 3 of Rieke et al. (2009)). These U/LIRGs were chosen such that their IR emission is dominated by star-forming activity. Construction of the SED library is done in two steps. First, these 11 galaxies were used as a basis to assemble 11

archetypal SED templates spanning 0.4 μ m to 30 cm wavelength. Their IRS spectra $(5-38 \mu m)$ were joined to the photospheric emission and far-IR dust emission components in a series of tests to ensure both spectral continuity and appropriate flux calibration. Second, these archetypal templates were combined with different weights to produce the final averaged SED templates. The template weights were optimized by matching synthesized IR colors from the combined template to the average IR colors of observed galaxies as a function of L(TIR) from IRAC and the IRAS RBGS (Sanders et al., 2003). The R09 library construction was extended to star-forming galaxies with sub-LIRG L(TIR) by combining the Dale & Helou (2002) SED library with the mid-IR spectral library based on IRS observations from Smith et al. (2007) using the same IR color fitting technique as in the U/LIRG template construction. The use of IR color to help guide the combination of archetypal templates (i.e., fitting $25/8 \mu m$, $25/12 \mu m$, and $60/25 \mu m$ colors simultaneously) helps ensure that the final templates represent the average properties of real galaxies even though they are constructed from a limited sample. The R09 SED library construction is described in detail in the Appendix of Rieke et al. (2009).

3.3 A Mid-IR Estimator for L(TIR) at 0 < z < 2.8

The construction of a 24 μ m SFR indicator has two steps: (1) construct an $L({\rm TIR})$ estimator using 24 μ m photometry, and then (2) derive a relationship between $L({\rm TIR})$ and SFR. The first step would appear to require measuring $\Sigma_{\rm L(TIR)}$ for each galaxy to determine the appropriate SED template. However, the relatively small scatter of the high-z galaxies around the main sequence in Figure 3.1 suggests that adequate SED template matching can be achieved by assuming a typical surface area. In this Section, we will use the sample with $\Sigma_{\rm L(TIR)}$ measure-

ments in Figure 3.1 to construct a formula that can be applied in the absence of the physical size measurements, based on the Rieke et al. (2009) formalism. We will test the resulting indicator from this Section with other independent L(TIR) measurements in section 3.4 and continue with the second step, deriving the relationship between L(TIR) and SFR, in Section 3.5.

The typical steps employed in the literature to calculate $L({\rm TIR})$ from a single-band observation are to find the best-matched SED for the observed flux at the redshift of the galaxy and then use the SED to determine the required bolometric correction (e.g., Pérez-González et al., 2005; Le Floc'h et al., 2005; Magnelli et al., 2009). This is effectively to fit the SED with a single data point. Rieke et al. (2009) introduce a formalism to improve on this process by first assigning a value of $L({\rm TIR})$ to each SED template and then determining the corresponding SFR as well as the monochromatic luminosity through the desired filter. For the 24 μ m band, in particular, the assignment of the 24 μ m luminosity of a template follows the ratio of $L(24~\mu{\rm m})$ -to- $L({\rm TIR})$ based on the local IRAS data (see Fig. 8, Fig. 15, and formula A6 of Rieke et al., 2009). Once each template has an associated 24 μ m luminosity, it is possible to calculate the k-corrections and subsequently the expected monochromatic flux for each template as a function of redshift. For $L_{\nu} \propto \nu f_{\nu}$, the k-correction, $K_{\rm corr}(z)$, and the flux, $f_{\nu}(24\mu m)$, are related by

$$K_{corr}(z) = (1+z)\frac{f_{\nu}(\nu = (1+z)\nu_{obs})}{f_{\nu}(24\mu m)}$$
 (3.1)

$$4\pi D_L^2 f_{\nu,\text{obs}} = \frac{L_{\nu,\text{rest}}(24\mu m)}{\nu_{24}} K_{\text{corr}}(z)$$
 (3.2)

where D_L is the luminosity distance for an object at redshift z. The $4\pi D_L^2 f_{24,\rm obs}$ for this equation has the unit of Jy cm². The relationship between the observed monochromatic flux from each template and the template's monochromatic lu-

minosity at a given redshift is approximately linear, which allows for a linear fit at each redshift (i.e., for a redshift grid) to determine a set of coefficients that converts the observed flux at a given redshift to the luminosity or any quantity associated with the template (e.g., $L({\rm TIR})$ and SFR). For example, a relationship between $L({\rm TIR})$ and the observed 24 $\mu{\rm m}$ flux, $f_{24,{\rm obs}}$, has the form

$$\log L(\text{TIR})_{z=0} = A(z) + B(z) \left[\log(4\pi D_L^2 f_{24,\text{obs}}) - C \right], \tag{3.3}$$

where A(z) and B(z) are the intercept and the slope from the linear fit, respectively, C is a zero-point to reduce covariance in the fit parameters, and $L(\mathrm{TIR})_{z=0}$ refers to the $L(\mathrm{TIR})$ associated to each of the R09 SED templates. Rieke et al. (2009) use this method to tabulate the coefficients to convert the monochromatic fluxes in various bands to the SFR of galaxies.

The Rieke et al. (2009) formalism successfully estimates L(TIR) and SFR for local galaxies. But, as noted by Rieke et al., a modification is needed to apply the formalism at high z. If we assume that IR star-forming galaxies beyond the local Universe are in the main sequence (discussions on the validity and applicability of this assumption in Section 3.6.2), it is possible to use the corresponding $\Sigma_{L(TIR)}$ as a guide to modify the Rieke et al. (2009) formalism to estimate L(TIR) and SFR at high z without the need for Σ_{SFR} measurements of individual galaxies. Following Rujopakarn et al. (2011), an appropriate choice of SED to use for calculations of the k-correction and bolometric correction beyond the local Universe is the one corresponding to the same $\Sigma_{L(TIR)}$ locally. This is equivalent to reassigning the L(TIR) associated with each of the R09 SED templates to new values determined by the ratio of luminosities with equal $\Sigma_{L(TIR)}$ on the local U/LIRG trend to those on the main sequence. We will refer to this ratio as the *stretching factor*, S_i , for each SED template. From Figure 3.1, S_i is nearly negligible at

 $L({\rm TIR})_{z=0}=10^{11}~L_{\odot}$ and reaches three orders of magnitude at $L({\rm TIR})_{z=0}$ of $10^{14}~L_{\odot}$. To determine S_i quantitatively, we parameterize the relationship by fitting a parabola to the local U/LIRG relation (excluding the lower limits of $\Sigma_{\rm L(TIR)}$ from CO observations) and a linear fit to the main sequence, and then take the ratio of $L({\rm TIR})$ on the main sequence fit to the R09 template $L({\rm TIR})$ at the same $\Sigma_{\rm L(TIR)}$ (see Figure 3.1; the S_i values are tabulated in Table 3.3). Since we effectively increase the luminosity of each template by a factor of S_i , the observed flux will also be increased by the same factor. Equation 3.3 can thus be rewritten as

$$\log L(\text{TIR})_{\text{new}} = \log \left[S_{i} L(\text{TIR})_{z=0} \right] = A'(z) + B'(z) \left[\log(4\pi D_{L}^{2} S_{i} f_{24,\text{obs}}) - C' \right]$$
(3.4)

The new set of coefficients, A'(z), B'(z), and C' that use the appropriate SED templates for main sequence star-forming galaxies at redshift 0 < z < 2.8 can be determined by re-fitting equation 3.4. We have limited the fitting range to only encompass the "stretched" luminosity of $\log L(\mathrm{TIR})_{\mathrm{new}} < 14$ because the stretched luminosities at large S_i are far greater than the luminosity range occupied by real galaxies (the 10^{14} L_{\odot} cut off is chosen because we expect this to be at or beyond the upper luminosity limit of star-forming galaxies). For a given template, the shape as a function of redshift remains the same. The effect of the S_i is to change the spacing between templates. The relationship between luminosity and observed flux remains well approximated as linear, with residuals < 0.05 dex.

The fitting coefficients, A'(z) and B'(z), to relate the observed *Spitzer* 24 μ m flux to L(TIR) as a function of redshift, are shown in Figure 3.2 (as dotted lines) and tabulated in Table 3.4. The zero-point, C', for the formula is 45. Thus the relation is

$$\log L(\text{TIR})_{\text{new}} = A'(z) + B'(z) \left[\log(4\pi D_L^2 f_{24,\text{obs}}) - 45 \right], \tag{3.5}$$

Table 3.3. Stretching Factors and $L({\rm TIR})_{\rm new}$ associated to Rieke et al. (2009) SED Templates

$\log L(\mathrm{TIR})_{z=0}^{\dagger}$	$\log S_i$	$\log L({ m TIR})_{ m new}$
9.75	-0.118	9.63
10.00	0.013	10.01
10.25	0.173	10.42
10.50	0.408	10.91
10.75	0.717	11.47
11.00	1.101	12.10
11.25	1.560	12.81
11.50	2.095	13.59
11.75	2.704	14.45
12.00	3.388	15.39

[†]The Rieke et al. (2009) SED templates with $L({\rm TIR})_{z=0} > 10^{12}~L_{\odot}$ are omitted because their $L({\rm TIR})_{\rm new}$ are higher than luminosities of observed galaxies. These SED template shapes are thus unlikely to represent real galaxies at high z.

Note. — Col. (1) Original L(TIR) associated to each of the Rieke et al. (2009) SED templates; Col. (2) stretch factors from the fit to the L(TIR)- $\Sigma_{L(\text{TIR})}$ relationship of local galaxies (Section 3.3); Col. (3) resulting $L(\text{TIR})_{\text{new}}$ associated to SED template shape from the fit.

Table 3.4. Coefficients of the Fits for the Relation Between Spitzer 24 $\mu \rm m$ Flux and the $L(\rm TIR)$

z	A'(z)	B'(z)
0.0	2.656	0.975
0.2	2.350	1.020
0.4	2.060	1.056
0.6	2.012	1.065
0.8	1.659	1.094
1.0	1.296	1.129
1.2	1.137	1.159
1.4	1.039	1.179
1.6	1.015	1.165
1.8	0.934	1.149
2.0	0.922	1.145
2.2	0.896	1.149
2.4	0.837	1.158
2.6	0.768	1.175
2.8	0.655	1.198

Note. — A'(z) and B'(z) are the coefficients for equation 3.5.

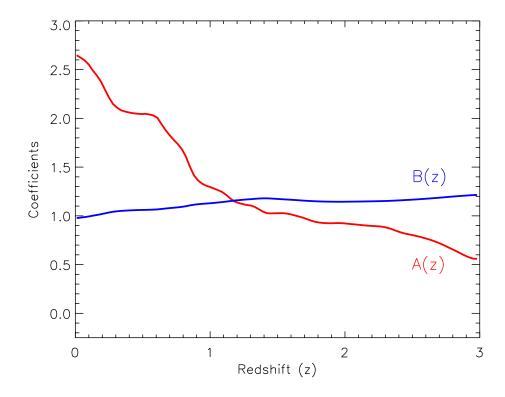


Figure 3.2: The coefficients of the fits for a relationship between the observed *Spitzer* 24 μ m flux and the total IR luminosity (Equation 3.5) as a function of redshift. The coefficients A'(z) and B'(z) are shown by the red and blue lines. These coefficients are tabulated in Table 3.4.

As is the case for Rieke et al. (2009), the feature in A'(z) and B'(z) at $z \sim 1.4$ is due to silicate absorption, which depends on template luminosity.

Apart from the 24 μ m single-band $L({\rm TIR})$ indicator, we also use the local $L({\rm TIR})$ - $\Sigma_{\rm SFR}$ relationship to derive the A(z) and B(z) coefficients to estimate $L({\rm TIR})$ from the 70 μ m observed flux (e.g., Spitzer MIPS or Herschel PACS). The resulting coefficients yield single-band 70 μ m $L({\rm TIR})$ consistent with the values from the original Rieke et al. (2009) estimator at $L({\rm TIR}) < 10^{11} L_{\odot}$ and overestimate the Rieke et al. (2009) $L({\rm TIR})$ by < 0.15 dex at higher luminosities. We do not anticipate strong evolution of the SED in the rest-frame wavelength range probed by the observed 70 μ m band at redshift z = 0 – 2.8 (70 – 18.4 μ m) because it is still in the Wien tail region of the dominant blackbody emission peak, unlike the 24 μ m band. Thus the Rieke et al. (2009) coefficients can be used to estimate $L({\rm TIR})$ and SFR from 70 μ m observations.

3.4 Testing the New 24 μ m L(TIR) Indicator

We conduct two series of tests to verify the performance of the new $24~\mu m~L({\rm TIR})$ indicator. In Section 3.4.1, we test the indicator on individual galaxies in the ECDFS with accurate far-IR photometry from Herschel and spectroscopic redshifts to establish that the method can successfully estimate $L({\rm TIR})$ of star-forming galaxies without systematic biases, as well as to quantify the scatter of $L({\rm TIR})$ estimates for individual galaxies. Individual gravitationally lensed galaxies at 1.0 < z < 2.7 with far-IR and sub-mm $L({\rm TIR})$ measurements are also introduced in this section to test the indicator at high z. In Section 3.4.2, we confirm the applicability of the indicator on the average SED of a wide range of star-forming galaxies in cosmological surveys at 0 < z < 2.8 using the stacked Spitzer far-IR photometry. Additionally, we verify the uncertainty estimate of the $L({\rm TIR})$ val-

ues using an independent sample of individual galaxies that have *Spitzer* far-IR observations and photometric redshifts in Section 3.4.3.

3.4.1 Testing the 24 μ m L(TIR) Indicator with Far-IR L(TIR) Measurements for Individual Galaxies

The individual galaxies used to verify that the new indicator predicts $L({\rm TIR})$ consistent with those from far-IR SED fitting are from the following: (1) the Herschel SPIRE observations in the Extended Chandra Deep Field South (ECDFS), which provide photometry near the peak of dust emission spectrum in addition to a large sample of spectroscopic redshifts and multiwavelength ancillary data for AGN identifications; and (2) the Herschel Lensing Survey (HLS; Egami et al., 2010; Rex et al., 2010) sample, which has high-S/N photometry that spans large $L({\rm TIR})$ and z ranges.

We retrieved the public *Herschel/SPIRE* imaging at 250, 350, and 500 μ m and followed the method described in Kennicutt et al. (2011) to produce the final maps in each band using HIPE release 8.1 (SPIRE pipeline version 8.0.3287). The original observations were from IDs 1342191158 to 1342191176 carried out under the HerMES survey (PI: S. Oliver). Flux measurements on these maps were done with PSF photometry using the DAOPHOT software (Stetson, 1987) on the 24 μ m prior positions from the FIDEL survey (C. Papovich, private communication) with no re-centering allowed. We measure the positional offsets between the prior coordinates and those of the SPIRE maps by stacking SPIRE sources and fit a 2D Gaussian to measure the offset of the resulting centroid of the stacked PSF from the priors. These offsets, $\alpha = -3'3$, $\delta = 0'8$, were applied to the maps before performing PSF photometry.

Since the *Herschel* SPIRE source extraction procedure is designed to yield a sample for the fiducial L(TIR) estimates to test our indicator, an emphasis must

be given to achieving an unbiased sample, rather than maximizing the number of detectable sources. To this end, we develop a figure of merit (FoM) and criteria by which we exclude potentially blended objects. This is important to mitigate the cases of intervening objects contributing additional flux to the object of interest. The FoM is defined by

FoM =
$$\sum_{i} [(R_i/4)^{-1} (d_i/6'')^{-1}]$$
 (3.6)

where R_i is the ratio of the 24 μ m fluxes of the prior object to the 24 μ m fluxes of other nearby objects within the SPIRE beam radius from the prior and d_i is the distance from the prior object to the corresponding nearby objects. The normalizations for R_i and d_i are chosen such that the FoM increases rapidly if other sources that are expected to be in the beam could be in within the same SPIRE pixel (6") or could have comparable SPIRE fluxes to the object at the prior position. The R_i normalization value is determined by inspecting the variation of the ratios of 24 and 250 μ m fluxes for SED templates in the Rieke et al. (2009) library, which gives a \sim 4× variation. That is, if the 24 μ m flux of a nearby object is less than \sim 1/4 that of the prior object, it is unlikely that its 250 μ m flux will be comparable to the prior (and hence cause a blending problem) at redshift 0 – 2.8, assuming the Rieke et al. (2009) SED shape. We emphasize that the exclusion does not depend sensitively on the normalizations in the FoM, and we have adopted a conservative rejection threshold by excluding objects with FoM > 2 from the final catalog, rejecting only the most likely blended objects.

AGNs are excluded from this test by excluding galaxies with $L_{\rm X}[0.5-8.0\,{\rm keV}] > 10^{42}$ erg/s and those exhibiting IR power-law SED (Donley et al., 2008), based on the *Chandra* X-ray and *Spitzer*/IRAC catalogs from Lehmer et al. (2005) and Damen et al. (2011), respectively. The exclusion of AGN using these standard methods does not compromise the integrity of the test of our method because

the goal of our indicator is to provide a deep IR probe for SFR in cosmological surveys, where deep X-ray and/or mid-IR (i.e., *Spitzer*/IRAC) observations are usually available. This is the case in every major deep field at the present, and future deep observational efforts will likely take place in these fields (e.g., ECDFS, GOODS-N, EGS, COSMOS, UDS). Thus, future investigations will be able to exclude AGN much as we have.

We then combine the *Spitzer* MIPS 24 and 70 μ m catalog from FIDEL and our SPIRE catalog to estimate the L(TIR) for galaxies in the ECDFS. We limit our sample to those that have high-quality spectroscopic redshifts from the Arizona CDFS Environment Survey (ACES) that has 5,080 secure redshifts from the Magellan/IMACS survey (Cooper et al., 2011). Specifically, we matched the ACES redshifts with quality flag Q = 3 or 4 to the 24 μ m priors. The final sample for SED fitting is selected at 250 μ m flux > 7 mJy, which yields 91 galaxies that passed all these criteria and the FoM cut (the latter excluded 70 galaxies that are likely blended). The final sample has redshifts ranging from 0.1 - 1.3 with a median redshift z = 0.6. The far-IR L(TIR) in the ECDFS is measured by fitting the Rieke et al. (2009) SED library to the MIPS 24 μ m (and 70 μ m where available) and at least one SPIRE band. We redshift the SED library to the value determined by the spectroscopic redshift of each object and minimize the χ^2 value over the choice of SED and the normalization factor. We inspect each SED fit visually to ensure fitting quality. Given the significantly smaller uncertainties of the MIPS 24 and 70 μ m points compared to those from SPIRE, we mitigate the possibilities that too much weight could have been put into the former two points by adding 3% uncertainties in quadrature to each data point. We experimented with adding up to 25% uncertainties in this way and found that the resulting L(TIR) values do not depend sensitively on the choice of uncertainties added. The final samples, along with their far-IR $L({\rm TIR})$, are reported in Table 3.5.

Table 3.5. Individual Galaxies in the ECDFS with *Herschel/SPIRE* observations and ACES Spectroscopic Redshifts

R.A.	Decl.	z	f_{24}	$L({ m TIR})\log(L_{\odot})$				
(J2000)	(J2000)		mJy	Far-IR	This Work	R09	CE01	
52 49 26.6	-27 35 57.9	0.311	0.197	10.46	10.29	10.27	10.36	
52 50 01.5	-27 49 29.3	0.842	0.412	11.63	11.66	11.92	11.60	
52 50 41.5	-27 47 25.9	0.181	0.810	10.35	10.37	10.38	10.34	
52 50 44.9	-27 37 56.5	0.735	0.248	11.37	11.30	11.46	11.28	
52 51 33.4	-27 41 55.7	0.732	0.550	11.68	11.67	11.88	11.62	
52 51 55.6	-27 58 00.6	0.675	0.206	11.28	11.15	11.27	11.14	
52 51 57.3	-27 56 16.4	0.644	0.274	11.32	11.24	11.37	11.22	
52 52 00.5	-27 41 55.4	0.730	0.318	11.44	11.41	11.58	11.38	
52 52 24.7	-27 34 18.3	0.680	0.366	11.42	11.42	11.58	11.38	
52 52 49.2	-27 59 36.0	0.739	0.305	11.53	11.40	11.58	11.37	
52 55 27.0	-27 56 35.1	0.510	0.642	11.44	11.38	11.51	11.35	
52 56 06.9	-27 42 12.0	0.973	0.421	11.97	11.82	12.25	11.77	
52 56 23.6	-27 42 03.7	0.840	0.193	11.27	11.30	11.49	11.25	
52 56 29.3	-27 51 30.0	0.681	0.789	11.78	11.78	11.98	11.71	
52 56 49.4	-27 46 22.6	0.574	0.291	11.17	11.16	11.26	11.16	
52 57 14.1	-27 39 45.2	0.813	0.415	11.58	11.63	11.87	11.59	
52 57 25.3	-27 43 26.4	0.620	0.935	11.82	11.78	11.95	11.70	
52 57 27.6	-27 43 53.8	0.670	0.367	11.45	11.41	11.56	11.37	
52 58 12.3	-27 51 15.5	0.678	0.145	11.00	10.99	11.09	11.00	
52 58 28.3	-28 03 33.9	0.123	0.738	10.00	9.95	9.95	9.93	
52 59 00.2	-27 54 53.5	0.733	0.088	10.96	10.81	10.91	10.77	

Table 3.5 (cont'd)

R.A.	Decl.	z	f_{24}		$L({ m TIR})$ log	$\operatorname{g}(L_{\odot})$	
(J2000)	(J2000)		mJy	Far-IR	This Work	R09	CE01
_							
53 00 58.2	-27 36 06.0	0.720	0.123	11.07	10.96	11.07	10.97
53 01 29.4	-27 45 07.3	1.067	0.285	11.66	11.77	12.28	11.74
53 01 42.7	-27 38 09.0	0.524	0.223	10.97	10.93	11.01	10.99
53 01 44.8	-28 01 37.0	1.131	0.159	11.78	11.59	12.10	11.56
53 01 53.8	-27 49 26.7	0.469	0.456	11.00	11.13	11.23	11.13
53 02 03.2	-28 03 51.4	0.602	0.165	11.05	10.95	11.04	10.99
53 02 07.7	-27 46 48.1	0.311	0.992	11.02	11.02	11.08	10.99
53 02 26.8	-27 44 42.4	0.085	1.100	9.85	9.78	9.78	9.75
53 02 40.5	-27 48 07.0	0.655	0.448	11.53	11.49	11.64	11.43
53 02 41.4	-27 56 01.0	0.520	0.162	10.82	10.77	10.84	10.81
53 02 42.7	-27 56 38.2	0.674	0.525	11.56	11.58	11.76	11.52
53 02 59.1	-27 38 40.1	0.728	0.566	11.66	11.68	11.89	11.63
53 03 02.9	-27 40 46.7	0.729	0.127	11.03	10.98	11.10	10.99
53 04 23.6	-28 00 44.3	0.228	0.478	10.48	10.37	10.37	10.37
53 04 33.8	-27 52 24.9	0.739	0.199	11.23	11.20	11.35	11.19
53 05 10.2	-27 51 42.2	0.679	0.323	11.35	11.36	11.51	11.33
53 05 13.8	-27 47 05.5	0.670	0.520	11.51	11.58	11.74	11.51
53 05 30.3	-27 54 28.4	0.203	0.935	10.57	10.55	10.56	10.51
53 05 32.2	-28 02 02.7	1.114	0.585	11.94	12.21	12.91	12.19
53 05 56.9	-27 58 45.6	0.124	3.211	10.59	10.60	10.61	10.51
53 06 07.9	-27 54 42.9	0.124	0.671	9.89	9.91	9.91	9.90

Table 3.5 (cont'd)

R.A.	Decl.	z	f_{24}		$L({ m TIR})$ log	$\operatorname{g}(L_{\odot})$	
(J2000)	(J2000)		mJy	Far-IR	This Work	R09	CE01
53 06 16.1	-27 34 11.4	0.502	0.246	10.90	10.92	11.00	10.98
53 06 36.3	-27 34 02.6	0.675	0.337	11.46	11.38	11.53	11.34
53 06 59.5	-27 46 39.2	0.247	0.806	10.75	10.69	10.70	10.64
53 07 21.7	-27 55 38.2	0.659	0.493	11.53	11.54	11.69	11.48
53 08 14.8	-27 50 30.2	0.670	0.350	11.39	11.39	11.54	11.35
53 08 22.7	-28 00 39.9	0.672	0.830	11.76	11.80	11.99	11.72
53 08 38.8	-27 53 24.4	1.101	0.178	11.34	11.60	12.08	11.57
53 09 18.3	-27 57 48.1	0.126	2.427	10.41	10.49	10.50	10.42
53 09 37.7	-27 46 33.7	0.622	0.211	11.13	11.09	11.20	11.10
53 09 41.7	-27 44 48.7	0.733	0.248	11.54	11.30	11.46	11.28
53 09 42.1	-27 49 56.3	0.241	0.504	10.38	10.45	10.45	10.44
53 10 26.0	-28 03 42.7	0.769	0.321	11.64	11.46	11.65	11.43
53 10 38.6	-27 38 25.7	0.250	1.559	11.02	10.99	11.03	10.94
53 11 49.5	-27 42 47.5	0.731	0.461	11.81	11.59	11.78	11.54
53 11 52.4	-27 41 06.4	0.415	0.705	11.07	11.18	11.28	11.16
53 12 20.9	-27 36 36.1	0.628	0.515	11.53	11.52	11.66	11.46
53 12 43.1	-28 03 17.8	0.213	0.956	10.67	10.61	10.62	10.56
53 12 57.1	-27 59 56.1	0.619	0.559	11.54	11.54	11.69	11.48
53 13 05.3	-27 41 52.3	0.605	0.418	11.41	11.39	11.51	11.35
53 13 12.9	-27 44 59.0	1.257	0.138	11.66	11.72	12.37	11.68
53 13 22.7	-28 03 33.9	0.685	0.251	11.23	11.25	11.39	11.23

Table 3.5 (cont'd)

R.A.	Decl.	z	f_{24}		$L({ m TIR})$ log	$\operatorname{g}(L_{\odot})$	
(J2000)	(J2000)		mJy	Far-IR	This Work	R09	CE01
53 13 28.7	-27 41 09.8	0.144	0.871	10.31	10.18	10.18	10.16
53 13 40.8	-27 34 21.2	0.141	1.103	10.34	10.26	10.27	10.25
53 14 23.6	-27 45 52.1	0.534	0.246	10.93	11.00	11.09	11.03
53 16 00.9	-28 02 05.3	0.703	0.253	11.29	11.28	11.42	11.25
53 16 42.6	-27 42 05.5	0.536	0.560	11.28	11.38	11.50	11.34
53 16 48.9	-27 45 51.3	0.217	0.544	10.45	10.38	10.38	10.37
53 17 03.5	-27 52 52.9	0.738	0.396	11.52	11.53	11.71	11.48
53 17 16.9	-27 58 46.1	0.669	0.482	11.56	11.54	11.70	11.48
53 17 32.6	-27 43 38.6	0.147	0.408	10.04	9.86	9.86	9.87
53 17 58.1	-27 53 46.8	0.533	0.754	11.46	11.51	11.65	11.45
53 18 00.0	-27 52 40.5	0.838	0.275	11.46	11.46	11.68	11.41
53 18 08.5	-28 00 16.3	1.089	0.313	11.81	11.86	12.41	11.82
53 18 08.6	-27 51 37.0	0.502	0.232	10.89	10.89	10.97	10.96
53 19 03.3	-28 02 23.1	0.349	0.426	10.79	10.76	10.80	10.74
53 19 10.9	-27 56 30.2	0.685	0.277	11.30	11.30	11.44	11.27
53 19 13.7	-27 41 21.4	0.147	2.499	10.77	10.66	10.68	10.58
53 19 46.2	-28 01 31.7	0.334	0.214	10.45	10.40	10.40	10.46
53 20 02.5	-27 46 12.1	0.978	0.470	11.76	11.88	12.33	11.83
53 20 10.6	-27 49 27.5	0.686	0.672	11.67	11.71	11.90	11.65
53 20 12.0	-27 34 31.9	0.311	0.954	11.01	11.00	11.06	10.98
53 20 22.3	-27 56 44.4	0.603	0.403	11.43	11.37	11.49	11.33

Table 3.5 (cont'd)

R.A.	Decl.	z	f_{24}	$L({ m TIR})\log(L_{\odot})$			
(J2000)	(J2000)		mJy	Far-IR	This Work	R09	CE01
53 20 24.7	-27 43 10.2	0.338	0.332	10.57	10.61	10.64	10.63
53 21 22.1	-27 46 12.1	0.521	0.163	10.83	10.78	10.84	10.81
53 22 37.1	-27 41 37.0	0.148	0.421	9.88	9.89	9.88	9.89
53 22 40.3	-27 44 02.7	0.863	0.841	12.07	12.03	12.37	11.95
53 23 02.7	-27 37 02.6	0.575	0.241	11.25	11.07	11.17	11.09
53 23 18.1	-27 57 04.7	0.618	0.209	11.15	11.08	11.19	11.09
53 23 45.3	-27 51 32.6	0.219	0.744	10.55	10.53	10.53	10.49

Note. — Col. (1) R.A. (J2000); Col. (2) Decl. (J2000); Col. (3) ACES spectroscopic redshifts; Col. (4) *Spitzer*/MIPS 24 μ m flux (mJy); Col. (5) Far-IR SED-fitted L(TIR), see Section 3.4.1 for details; Col. (6) L(TIR) estimated with formula from Equation 3.4; Col. (7) L(TIR) estimated by the Rieke et al. (2009) formulae; Col. (8) L(TIR) estimated by routines provided by Chary & Elbaz (2001).

The HLS sample consists of 19 galaxies located behind the Bullet Cluster at redshifts 0.4 < z < 2.7 (Rex et al., 2010). These sources are detected in at least two *Herschel* bands (at $100 - 500 \ \mu m$) and many are also observed in LABOCA 870 micron and AzTEC 1.1 mm maps of the field (Wilson et al., 2008; Johansson et al., 2010). These measurements tightly constrain the peak of the far-IR SED and therefore provide accurate estimates of L(TIR). We have excluded one object from this sample, HLS18, because its large lensing magnification (54×) is not well constrained due to nearby objects (Rex et al., 2010). Otherwise, the lensing

magnifications are small (median $1.1\times$). The HLS galaxies used in the test are listed in Table 3.6.

We have found from the tests using ECDFS and HLS data that the mid-IR excess issue discussed in the Introduction is nearly completely removed. By using the new indicator, the resulting single-band 24 μ m-derived L(TIR) has an average agreement with the far-IR observations of 0.02 dex and a 1- σ scatter of 0.12 dex, shown in Figure 3.3. The 0.12 dex scatter is consistent with the 0.13—dex scatter of the relationship between $L(24 \mu m)$ and L(TIR) in the local sample found by Rieke et al. (2009). The core distribution of luminosity difference between L(TIR) estimates from Herschel and the new indicator can be fitted by a Gaussian that has a σ of 0.06 dex, reflecting the degree of agreement wherever the extended structure assumption leads to a successful prediction of SED features. We found 8% of the ECDFS and HLS galaxies to have L(TIR) estimates from this method disagreeing by more than 0.2 dex from those of *Herschel*, with 2% and 6% on the over and underestimation sides, respectively. The overestimation is due to enhanced flux at 24 μ m compared to star-forming galaxy SEDs, suggesting a mid-IR emission contribution from unidentified AGNs. SED fits for the 6% of objects where the indicator underestimates L(TIR), indicates warmer far-IR SEDs than that predicted by the indicator, which suggests that their starburst structures are more compact, similar to local U/LIRGs, and inconsistent with our extended structure assumption. This is illustrated by lines in the bottom panel of Figure 3.3 (color-coded by z) that show where the compact local U/LIRGs would be if the extended structure assumption is applied. Figure 3.3 indicate that although some U/LIRGs at high z could be compact, these are in the minority at a < 10%level.

Table 3.6. Galaxies with Far-IR $L({
m TIR})$ Measurement for $L({
m TIR})$ Indicator Calibration

ID	z	f_{24}		$L({ m TIR}) \log$	Lensing Mag		
		mJy	Far-IR	This Work	R09	CE01	×
HLS01	0.610	0.400	11.41	11.36	11.45	11.30	1.10
HLS02	2.700	0.150	12.60	12.65	13.41	13.36	1.00
HLS03	0.720	0.390	11.49	11.54	11.68	11.46	1.00
HLS04	0.820	0.390	11.61	11.66	11.85	11.56	1.00
HLS05	1.600	0.710	13.20	12.80	13.57	12.87	1.16
HLS06	1.800	0.400	12.70	12.41	13.00	12.78	1.11
HLS07	0.660	0.290	11.20	11.28	11.37	11.22	1.10
HLS08	0.430	0.135	10.38	10.39	10.41	10.50	1.20
HLS09	0.820	0.650	11.92	11.86	12.08	11.75	1.10
HLS10	0.600	0.530	11.49	11.48	11.58	11.40	1.10
HLS11	1.070	0.470	11.92	11.95	12.40	11.82	1.40
HLS14	0.570	0.136	10.78	10.78	10.82	10.78	1.10
HLS15	1.170	0.160	11.67	11.70	12.15	11.57	1.10
HLS16	0.450	0.830	11.40	11.22	11.31	11.18	1.40
HLS17	0.400	0.710	11.43	11.12	11.19	11.09	1.10
HLS19	0.710	1.100	12.04	11.98	12.16	11.85	1.10

Note. — See Section 3.4 for details on the HLS (Rex et al., 2010) sample.

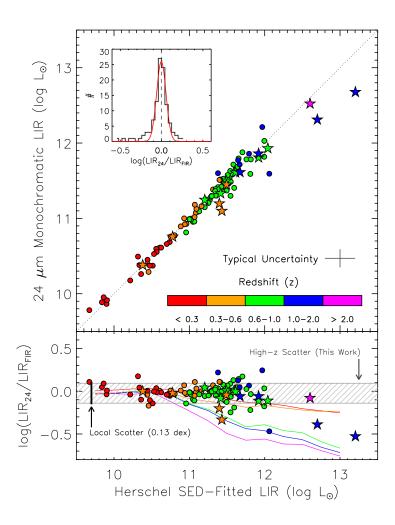


Figure 3.3: Comparison of $L(\mathrm{TIR})$ derived from this work to $L(\mathrm{TIR})$ measured by integrating the SED fitted to far-IR multi-band photometry for individual galaxies from $\mathit{Herschel}$ in the Extend Chandra Deep Field South (ECDFS) that have secure spectroscopic redshifts (circles); and in the $\mathit{Herschel}$ Lensing Survey (HLS; stars). The bottom plot shows the ratio of $L(\mathrm{TIR})$ from our single-band 24 $\mu \mathrm{m}$ indicator to the far-IR $L(\mathrm{TIR})$. The overall scatter is 0.12 dex (shaded region), which is comparable to the scatter of the relationship between $L(24~\mu \mathrm{m})$ and $L(\mathrm{TIR})$ found locally (0.13 dex; illustrated by a vertical bar on the left). The lines in the bottom panel (color-coded by z) indicate the ratios that would result if the star-forming regions in high-z IR galaxies are as compact as those found locally (i.e., if our extended structure assumption fails), which is the case for 6% of galaxies; each line corresponds to the upper-end of each z bin in the top panel. The inset shows a Gaussian fit to the distribution, which has a σ of 0.06 dex, indicating the degree of agreement where our extended structure assumption applies.

Figure 3.4 illustrates the extent of the mid-IR excess due to the assumption of local bolometric corrections that result in overestimation of $L(\mathrm{TIR})$ compared to far-IR measurements, as in the Rieke et al. (2009) formulae. The results from the improved bolometric corrections are shown in comparison, which indicate that the overestimation problem is no longer present.

We tabulated the luminosity of the appropriate R09 SED template that should be used to describe star-forming galaxies given their 24 μ m observed flux and redshift in Table 3.7. Even at the bright-end of the flux range at high-z (e.g., $f_{24}=3.0$ mJy at z=2.8, which corresponds to $L({\rm TIR})$ of $10^{14.2}~L_{\odot}$), the appropriate R09 templates are those of local LIRGs with $L({\rm TIR})$ of no more than $10^{11.7}~L_{\odot}$. In fact, it is evident from the table that most IR-luminous star-forming galaxies at 0 < z < 2.8 exhibit spectral characteristics of local galaxies with $L({\rm TIR})$ in the range of $10^{10}-3\times10^{11}~L_{\odot}$.

We also tested the indicator on individual star-forming galaxies at 1.0 < z < 2.7 using a sample of gravitationally lensed galaxies for which we obtained near-IR and mid-IR spectroscopic observations with the Large Binocular Telescope and *Spitzer*, and far-IR/sub-mm observations from the literature (Rujopakarn et al., 2012). The sample was augmented by two additional objects that have a similar suite of data from the literature. Rujopakarn et al. (2012) find that the indicator from this work estimates L(TIR) in good agreement with their far-IR L(TIR) values, with an average difference of 0.07 dex (although there is one outlier whose difference is 0.18 dex). The data points from (Rujopakarn et al., 2012) are also reproduced in Figure 3.5.

This agreement of L(TIR) values from the new indicator and those from far-IR measurements indicates that our assumption that high-z star-forming galaxies indeed have extended star formation (i.e., that they are dominated by main-

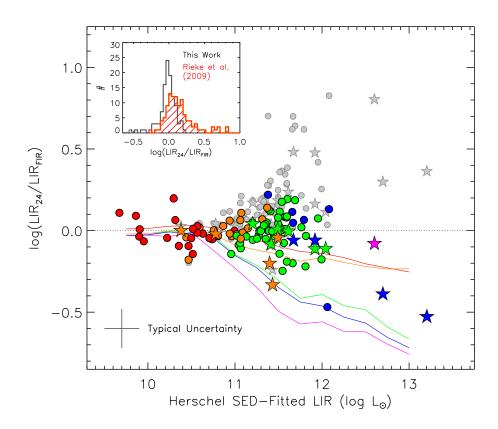


Figure 3.4: Same as Figure 3.3 but with the $L({\rm TIR})$ values from the Rieke et al. (2009) indicator shown as a comparison in grey. Color coding is identical to Figure 3.3 (color coding for the Rieke et al. indicator is omitted for clarity). The inset shows the histogram of the ratio, with values from the new indicator and those of Rieke et al. (2009) shown in black and red histograms, respectively. While the Rieke et al. (2009) indicator overestimates $L({\rm TIR})$ values compared to Herschel $L({\rm TIR})$, this overestimation and the "mid-IR excess problem" (Section 3.4.1) are shown to be alleviated by the new $L({\rm TIR})$ indicator.

Table 3.7. The Luminosity of the Appropriate Rieke et al. (2009) SED Template to Describe SED of a Star-Forming Galaxy for a Given 24 μ m Flux and Redshift

f_{24}					Redsh	$\operatorname{nift}(z)$				
(mJy)	0.10	0.50	0.75	1.00	1.25	1.50	1.75	2.00	2.50	2.80
0.02		9.9	10.1	10.2	10.4	10.5	10.5	10.5	10.6	10.8
0.05		10.1	10.3	10.4	10.6	10.7	10.7	10.7	10.8	11.0
0.1		10.3	10.5	10.6	10.8	10.9	10.8	10.8	11.0	11.1
0.2		10.4	10.6	10.7	10.9	11.0	11.0	11.0	11.1	11.2
0.4	9.7	10.6	10.8	10.9	11.1	11.1	11.1	11.1	11.3	11.4
0.8	9.9	10.7	10.9	11.0	11.2	11.3	11.2	11.2	11.4	11.5
1.5	10.0	10.9	11.0	11.1	11.3	11.4	11.3	11.3	11.5	11.6
3.0	10.2	11.0	11.1	11.3	11.4	11.5	11.4	11.5	11.6	11.7

Note. — Dots indicate that the combination of flux and redshift would yield a SED template that is outside the luminosity range of the Rieke et al. (2009) SED library, $L({\rm TIR})=10^{9.75}-10^{13}~L_{\odot}$. As a reference, the $\log(L({\rm TIR})/L_{\odot})$ values for the archetypal local IR galaxies M82 and Arp 220 are 10.77 and 12.21, respectively.

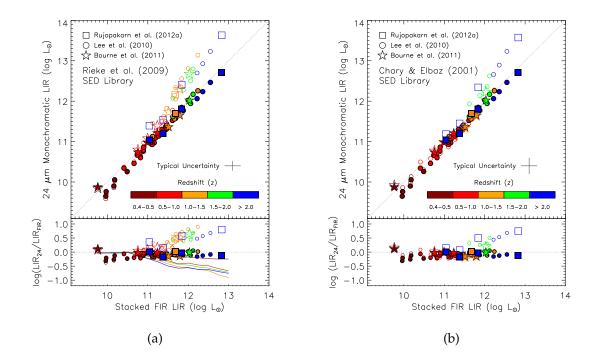


Figure 3.5: Comparison of L(TIR) from our single-band 24 μm indicator to L(TIR) measured from stacked and gravitationally lensed galaxies with far-IR observations. The comparison samples are from Lee et al. (2010) who determined L(TIR) at 0 < z < 3 by stacking 70 μ m and 160 μ m observations of over 35,000 COSMOS galaxies; from Bourne et al. (2011) whose L(TIR) was determined from stacking a broad range of observation from 24 μ m to 610 MHz of 3,172 galaxies at 0 < z < 2 in the ECDFS-FIDEL sample; and from Rujopakarn et al. (2012) whose sample comprise gravitationally lensed galaxies at 1.0 < z < 2.7 that allows high-z, low-luminosity LIRGs into this comparison. In the left and right panels, we show L(TIR) estimates from the new indicator as filled symbols in comparison to L(TIR) estimates from the R09 and CE01 SED library (open symbols in each panel). The lines in the bottom plot of the left panel illustrate the ratios that would result if the star-forming regions in high-z IR galaxies are as compact as those found locally (see also, Figures 3.3 and 3.4). The right panel also illustrates our findings discussed in Section 3.4.2 that the mid-IR excess problem does not become apparent for the CE01 estimates until $z \sim 1.5$ because their overestimation of the PAH-region fluxes compared to local galaxies helps compensate the evolution of PAH strength at high z.

sequence star formation) is consistent with the properties of individual galaxies in the ECDFS and HLS, and with lensed galaxies of lower intrinsic luminosity.

3.4.2 Tests of the 24 μ m L(TIR) Indicator on Average SEDs

Next, we explore the applicability of the new indicator for large samples using stacked photometry to represent the average properties of galaxies. We adopt two samples for these tests: (1) the stacked 70 μ m and 160 μ m photometry of a 24 μ m-selected sample from Lee et al. (2010) in COSMOS; and (2) the stacked 24 μ m, 70 μ m, 160 μ m, 1.4 GHz, and 610 MHz observations of a NIR-selected sample from the Extended Chandra Deep Field-South survey (ECDFS) (Bourne et al., 2011). Unlike the earlier ECDFS and HLS samples, these L(TIR) estimates rely to a greater extent on extrapolating a fitted-SED to the dust emission peak. The goal of this section is thus not to determine the scatter for individual galaxies, but to test the indicator on a large sample across a broad redshift range.

The Lee et al. (2010) sample stacks 70 μ m and 160 μ m observations of galaxies selected at 24 μ m in COSMOS and represents the average SED properties of over 35000 galaxies. The stacks were done in bins of 24 μ m flux (0.06 < f_{24} < 3.00 mJy) and redshift (0 < z < 3). Lee et al. then fit SEDs to the average 24 μ m, 70 μ m and 160 μ m fluxes in each stacked bin to estimate L(TIR). We have excluded bins where the fraction of X-ray sources (i.e., AGN) exceeds 10% based on their Figure 3. For the actual L(TIR) calculation we use the average value of 24 μ m flux and redshift in each bin (N. Lee, 2011, private communication) to calculate the average L(TIR) of the bin, which can be compared with the estimates from Lee et al. (2010).

The Bourne et al. (2011) stacked sample of 3172 galaxies was selected using *Spitzer* IRAC 3.6 μ m and 4.5 μ m photometry (i.e., a stellar mass selected sample) in ECDFS. The selection in the near-IR provides an independent sample that has a

potential to reveal selection effects (if any) inherent to mid- and far-IR selections (e.g., the Lee et al. (2010) and Kartaltepe et al. (2010) samples). Bourne et al. stacked observations of the sample in 7 redshift bins from 0 < z < 2.0. These observations include 24 μ m, 70 μ m, 160 μ m, 1.4 GHz and 610 MHz; the stacked fluxes of the *Spitzer* MIPS bands were then used to fit a M51 SED to estimate $L({\rm TIR})$.

We compare with Lee et al. (2010) and Bourne et al. (2011) for our indicator and for the R09 and CE01 SED libraries separately in the left and right panels of Figure 3.5, respectively. A difference between the two panels is that the mid-IR excess becomes a problem for the R09 library well below z = 1 while only becomes noticeable for CE01 at z > 1.5 (see also, Elbaz et al. (2010), Figure 1), as is observed in Figure 3.3. This is because the omission of silicate absorption features in the CE01 SED templates results in an overestimation of PAH-region flux in the local SED templates that coincidentally helps compensate for the evolution of PAH strength and delays the emergence of the mid-IR excess problem until beyond $z \sim 1.5$. The R09 templates correctly include the silicate absorption locally, and hence suffer a larger overestimation of L(TIR). We have now shown that the R09 templates can be used to describe the SED of galaxies and estimate the bolometric corrections out to $z\sim2.8$ given an appropriate choice of SED template based on the $\Sigma_{L(TIR)}$. There is no indication of systematic trends emerging at $z\sim 1$ and $z\sim 2$ where the 11 μ m and 7 μ m aromatic complexes redshift into the 24 μ m band.

3.4.3 Verifying the Uncertainty Estimate for Individual Galaxies with an Independent Sample

Having established that the scatter of the L(TIR) estimates from our indicator is roughly 0.12 dex compared to far-IR L(TIR) measurements based on the ECDFS

and HLS data (Section 3.4.1), we now seek to verify this scatter estimate using a larger sample selected at a different wavelength.

We compare the new L(TIR) indicator to the L(TIR) estimates from the 70 μ m-selected COSMOS sample (Kartaltepe et al., 2010). The entire sample contains 1503 galaxies at 0 < z < 3.5 (median z = 0.5) with L(TIR) estimated by fitting IR photometry from *Spitzer* at the 8, 24, 70, and 160 μ m bands to a collection of SED libraries, with the best fit selected via χ^2 minimization among the Chary & Elbaz (2001), Dale & Helou (2002), Lagache et al. (2003), and Siebenmorgen & Krügel (2007) templates. For our comparison, we exclude sources with X-ray luminosity $> 10^{42}$ erg/s and those with radio-excess. The sample is complete at 70 μ m, by definition, and also at 24 μ m, which allows the 70 and 24 μ m color to be used as a criterion to select AGN that dominate the mid-IR emission. Specifically, we exclude objects with $log(f_{70}/f_{24}) < 0.2z + 0.7$ (i.e., objects with enhanced 24 μ m flux for a given 70 μ m flux compared to the SEDs of star-formating galaxies), which removes 86 galaxies. Above $10^{12.5} L_{\odot}$, the Kartaltepe et al. (2010) sample contains very few sources that do not harbor AGN or QSO. We limit our comparison sample to those with uncertainties in SED-fitted L(TIR) < 0.35 dex to avoid comparing to objects with uncertain luminosity.

Among the 1503 galaxies selected at 70 μ m, 463 are detected at 160 μ m and their fluxes have been included in the SED fitting by Kartaltepe et al. (2010); 410 of these pass our AGN and uncertainty criteria. However, the 160 μ m detections for these sources are of low significance: 236/410 galaxies (57%) are below 5 σ , where the σ value includes the confusion noise of 10 mJy for the survey (Frayer et al., 2009). Kartaltepe et al. (2010) report that including the 160 μ m photometry in the SED fitting to measure L(TIR) causes the L(TIR) values to be overestimated by 0.2 dex compared to the values from fitting SEDs without the 160 μ m point.

This problem is consistent with Hogg & Turner (1998), who show that detections below $4-5\sigma$ are dominated by spurious sources or are significantly biased towards brighter fluxes than their true values; see their Figure 2. This is commonly known as the Eddington bias, in agreement with this explanation, the overestimation is alleviated if the stacked 160 μ m flux is used for SED fitting instead of fluxes from individual objects. More than 85% of the 160 μ m detections are below 8σ ; therefore, based on Hogg & Turner (1998), they are likely to be heavily contaminated by false detections. The remaining 15% with relatively secure detections at 160 μ m have a median redshift of 0.17 and thus will not provide a discriminating test for the quality of the SED mapping at high z. We therefore exclude the 160 μ m-detected objects to avoid the spurious detections associated with the Eddington bias as well as flux measurement errors due to confusion.

After applying the cuts discussed at the beginning of this section, we have 751 sources left. These sources have redshifts ranging from z=0.07 to 1.81 with a mean and median redshift of 0.52 and 0.43. The luminosity of this subsample ranges from $L({\rm TIR})$ of $10^{9.5}$ to $10^{12.5}$ L_{\odot} and the mean and median $L({\rm TIR})$ s are $10^{11.1}$ and $10^{11.2}$ L_{\odot} , respectively.

The comparison with $L({\rm TIR})$ estimated from the 24 $\mu{\rm m}$ fluxes alone indicates an average scatter of 0.25 dex. Some fraction of this scatter must arise in the assignment of $L({\rm TIR})$ by Kartaltepe et al. (2010); the median luminosity uncertainty within their work is 0.23 dex. That is, the 24 $\mu{\rm m}$ -only calculation agrees with their multi-wavelengths fits virtually within the internal scatter of these fits. We quantify the contribution of uncertainties intrinsic to the new indicator in this test by conducting a Monte Carlo experiment to determine the scatter that must arise from our estimation of Kartaltepe et al. (2010) luminosities. We simulate a sample ($n=10^4$) with a scatter of 0.23 dex and re-measure the values, introducing

measurement errors in the process, which shows that an uncertainty of \sim 0.1 dex associated to the new indicator will broaden the intrinsic scatter of the Kartaltepe et al. (2010) sample to the 0.25 dex measured. This result is consistent with the 0.12 dex scatter found in Section 3.4.1.

3.5 L(TIR)-SFR Relation

Finally, SFRs can be determined by making use of the relationship between $L({\rm TIR})$ and the rest-frame $L(24~\mu{\rm m})$, and subsequently the $L(24~\mu{\rm m})$ and SFR, originally given by Rieke et al. (2009). The introduction of the stretching factor, which is effectively to re-normalize the SED templates, requires a modification of the relationship between $L({\rm TIR})$ and $L(24~\mu{\rm m})$. The original fit as given in equation A6 of Rieke et al. (2009) is

$$\log L(\text{TIR})_{z=0} = 1.445 + 0.945 \log L(24) \tag{3.7}$$

The modified relationship is obtained by re-fitting equation 3.7 with the stretching factor, S_i , multiplying both L(TIR) and $L(24 \, \mu\text{m})$ for each template i. The re-fitted relation allows $L(24 \, \mu\text{m})$ to be calculated from $L(\text{TIR})_{\text{new}}$ from equation 3.5 as following

$$\log L(24) = \frac{1}{0.982} \left[\log L(\text{TIR})_{\text{new}} - 1.096 \right]$$
 (3.8)

To determine the SFR from $L(24~\mu\text{m})$, the calibration given by Rieke et al. (2009) remains valid. However, that calibration has a term that corrects for a decrease in $L(24~\mu\text{m})/L(\text{TIR})$ ratio above $L(\text{TIR})=10^{11}~L_{\odot}$. Since the correction is motivated by an increase of the optical depth at high L(TIR) that prevents the mid-IR emission from escaping, the threshold at which optical depth becomes

significant depends directly on the geometry of the galaxy. In the same way that the extended structure of the galaxy beyond the local Universe affects the IR-emitting environment, the optical depth will consequently be lower for a given $L({\rm TIR})$ and the luminosity threshold where the optical depth should apply has to be scaled up by a stretching factor as well. The S_i corresponding to the original threshold is $12.6\times$ (referring to Table 3.3), yielding a luminosity threshold of $1.3\times 10^{12}~L_{\odot}$. This is equivalent to $L(24~\mu{\rm m})$ of $1.6\times 10^{11}~L_{\odot}$. Therefore the relationship between SFR and $L(24~\mu{\rm m})$ is given by

$$SFR(M_{\odot} \text{ yr}^{-1}) = 7.8 \times 10^{-10} \text{ L}(24 \,\mu\text{m}, L_{\odot})$$

for $5 \times 10^9 \ L_{\odot} \le L(\text{TIR}) \le 1.3 \times 10^{12} \ L_{\odot}$ or $6 \times 10^8 \ L_{\odot} \le L(24 \ \mu\text{m}) \le 1.6 \times 10^{11} \ L_{\odot}$. For $L(\text{TIR}) > 1.3 \times 10^{12} \ L_{\odot}$ or $L(24 \ \mu\text{m}) > 1.6 \times 10^{11} \ L_{\odot}$,

$$SFR(M_{\odot} \text{ yr}^{-1}) = 7.8 \times 10^{-10} \text{ L}(24 \,\mu\text{m}, L_{\odot}) \times \left[6.2 \times 10^{-12} \text{ L}(24 \,\mu\text{m}, L_{\odot})\right]^{0.048} (3.9)$$

This calibration is based on that of Kennicutt (1998) but with the Kroupa (2002) IMF, which yields SFRs a factor of 0.66 of those assuming the Salpeter (1955) IMF. A library of IDL routines for the L(TIR) and SFR indicator is available at our website¹.

3.6 Discussion

Here we discuss the validity of using 24 μ m observation at 0 < z < 2.8 to derive $L({\rm TIR})$ and SFR in Section 3.6.1, and in Section 3.6.2, the implications of the $L({\rm TIR})$ indicator in light of the test results from Section 3.4. In addition, we will discuss the implications of the new indicator on the maximum typical $L({\rm TIR})$ for high-z ULIRGs in Section 3.6.3.

¹http://ircamera.as.arizona.edu/rujopakarn2011

3.6.1 Validity of the Aromatic Emission as a L(TIR) and SFR Indicator

The new indicator utilizes the luminosity at rest-frame wavelengths of 24 μ m to 6 μ m at z=0 to 2.8. This necessitates an investigation of the validity of using the aromatic features that contribute significantly to the emission at this wavelength region as a tracer for L(TIR). We discuss two major factors affecting the aromatic feature strength: the metallicity dependence and the presence of AGN.

The correlation of the aromatic luminosity to $L({\rm TIR})$ was studied by Rigopoulou et al. (1999), Roussel et al. (2001) and Elbaz et al. (2002) using ISO; later by Wu et al. (2005) with Spitzer; and recently by Elbaz et al. (2011) with Herschel. Calzetti et al. (2007) used the SINGS sample to show that the scatter and the non-linearity of the relationship between the extinction-corrected 8 μ m luminosity and the extinction-corrected Pa α luminosity (which is a good tracer for SFR) is unsatisfactorily large for the former to serve as a SFR indicator. However, their Figure 10 suggests that the largest source of scatter is due to the metallicity differences among the subsamples. For high-metallicity systems (Z > 1/3 Z_{\odot} , which is equivalent to $12+\log({\rm O/H}) \gtrsim 8.2$), Calzetti (2010b) reports that the stellar-continuum-subtracted PAH emission shows a good correlation with the SFR. Furthermore, Engelbracht et al. (2008) and Smith et al. (2007) find that the ratio of aromatic luminosity to $L({\rm TIR})$ does not vary significantly at metallicity $\gtrsim 1/3$ Z_{\odot} .

Smith et al. (2007) found that AGN can significantly suppress the PAH emission (see also, Moorwood, 1986; Roche et al., 1991; Genzel et al., 1998). The suppression of PAH luminosity is shown in Figure 3.6 using the total PAH luminosities measured by Smith et al. (2007) and a metallicity measurement from Moustakas et al. (2010). Moderate luminosity AGN, however, do not affect the PAH emission of the entire host galaxy. Diamond-Stanic & Rieke (2010) use *Spitzer* IRS to compare nuclear and non-nuclear spectra of nearby Seyfert galaxies and

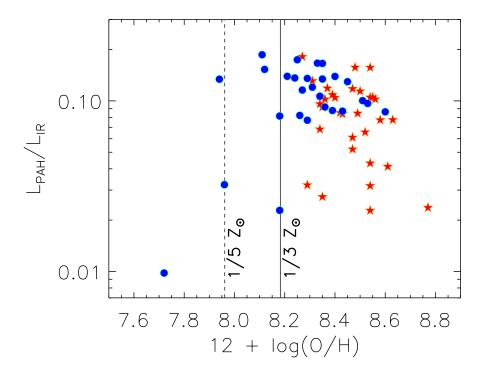


Figure 3.6: The sources of scatter in using aromatic emissions (e.g., PAH) to predict $L(\mathrm{TIR})$ and SFR are primarily the metallicity dependence and the presence of AGN. Blue dots and red stars show the ratios of aromatic luminosity to $L(\mathrm{TIR})$ as a function of metallicity for HII and AGN dominated local galaxies, respectively (Smith et al., 2007). For HII-dominated galaxies with metallicity greater than $1/3~Z_{\odot}$ (solid vertical line), which is similar to the environment of high-z star-forming galaxies, the correlation of aromatic luminosity, L_{PAH} , and $L(\mathrm{TIR})$ has a ~ 0.1 dex scatter, suggesting that aromatic emission could serve as a good $L(\mathrm{TIR})$ and SFR indicators at high z.

found that while the PAH features in the nuclear spectra are clearly suppressed, the features are of normal strength in the outer disk. Therefore, with regard to using PAH emission to trace $L({\rm TIR})$: (1) the PAH suppression effect due to AGN is likely limited to the nuclear region and PAH emission arising from the rest of the galaxy should still provide a good tracer of the SFR; and (2) the longer wavelength emission such as the 11.3 μ m PAH emission complex, which the 24 μ m observation probes at $z\sim 1$, could still serve as a SFR indicator despite the presence of low-luminosity AGN (Diamond-Stanic & Rieke, 2010).

Galaxies at $z\sim 2$ have on average 0.3 dex lower metallicity than local galaxies (Erb et al., 2006). Therefore, galaxies more massive than $3\times 10^9~{\rm M}_\odot$ should be sufficiently metal rich (> $1/3~Z_\odot$) that the $L({\rm TIR})/{\rm PAH}$ calibration is valid. If we consider the ratio of aromatic-luminosity-to- $L({\rm TIR})$ as a function of metallicity in Figure 3.6 within the range of metallicity expected at high-z, the scatter of the relationship between aromatic luminosity and $L({\rm TIR})$ is in fact about $0.1~{\rm dex}$ in the non-Seyfert/LINER sample. This suggests aromatic luminosity to be a good indicator for $L({\rm TIR})$ at high-z given that an effort is made to exclude AGN from the sample (such as the AGN exclusion criteria employed in tests in Sections 3.4.1 and 3.4.2).

We further test the validity of aromatic emission (e.g., 8 μ m rest-frame observation) as a measure of L(TIR) in a sample of HII-dominated galaxies with moderate to high metallicity in Figure 3.7. In this Figure, the 8 μ m observations are from *Spitzer* and the L(TIR) estimates are based on the *IRAS* all-sky survey using 12, 25, 60, and 100 μ m observations (Sanders et al., 2003). This sample is chosen such that it mimics the population of star-forming galaxies expected at high z: high-metallicity normal star-forming galaxies without AGN. The scatter of the relationship between L(8 μ m) and L(TIR) in Figure 3.7 is 0.14 dex with the ratio

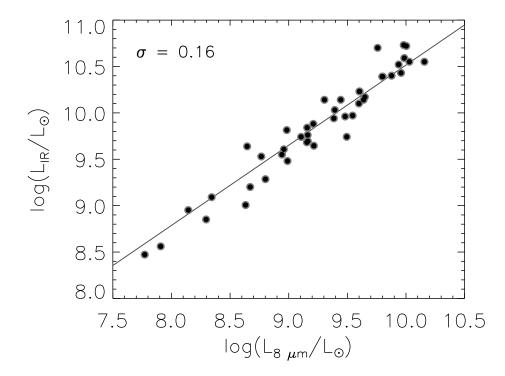


Figure 3.7: The correlation between the rest-frame L(8 μ m) and L(TIR) for local star-forming galaxies that are dominated by HII-emission and have high metallicity, similar to those expected at high z, has a scatter of 0.14 dex. The small scatter underlines the potential of using aromatic emission as a L(TIR) and SFR indicator.

 $L(\text{TIR})/\text{L}(8 \,\mu\text{m})$ of 4.3 ± 1.6 . Elbaz et al. (2011) reports a similar $L(\text{TIR})/\text{L}(8 \,\mu\text{m})$ of $4.9^{+2.9}_{-2.2}$ for their GOODS-Herschel sample out to $z \sim 3$, which, along with the result of Nordon et al. (2012) that $L(8 \,\mu\text{m})$ traces L(TIR) for high-z galaxies in GOODS-Herschel (see, e.g., their Equation 5), further reinforces the applicability of aromatic emissions as L(TIR) and SFR indicator.

3.6.2 Modes of Star Formation and the Validity of the Main Sequence Assumption

In the process of constructing our $L({\rm TIR})$ indicator, we have assumed that all non-local star-forming galaxies lie in the main-sequence, i.e., have extended star formation; in other words, that the star formation beyond the local Universe is not dominated by compact, merger-induced, nuclear-concentrated starbursts. The results from Sections 3.4.1 and 3.4.2 indicate that our assumption is consistent with the nature of high-z galaxies: (1) the potentially compact starbursts, whose $L({\rm TIR})$ are underestimated compared to their far-IR $L({\rm TIR})$, comprise only 6% of the sample, and (2) the comparison of stacked samples shows no systematic discrepancies. In this section, we will discuss other evidence from morphological studies and recent observations that also point to the extended mode of star formation at high-z.

At intermediate and high z, the precise fractions of galaxies that form stars in the extended and compact merger-induced modes remain a subject of controversy. A tracer for merger-induced starbursts is the galaxy merger fraction, which can be estimated from morphological studies. Lotz et al. (2008) report a relatively constant major merger (i.e., mass ratio >1:3) fraction of $10\%\pm2\%$ for all galaxies in their sample at 0.2 < z < 1.2 and $\sim 15\%$ for U/LIRGs. Shi et al. (2009) find that the fraction of galaxies exhibiting asymmetric morphologies in the same redshift range is 20%-30% and as many as $\sim 50\%$ for LIRGs. The Lotz et al. (2008)

figures represent a conservative estimate by limiting mergers to major mergers while Shi et al. (2009) provide an upper limit, since not all asymmetric galaxies are mergers. For ULIRG and LIRG populations at z < 1, Kartaltepe et al. (2010) find that the merger fractions are $\sim 50\% - 80\%$ and $\sim 25\% - 40\%$, respectively. However, morphological studies are increasingly compromised by the limited angular resolution and surface brightness sensitivity at higher redshifts. More importantly, disturbed morphologies found at high z are not necessary a result of mergers but could also be due to clumpy or asymmetric star-formation in gasrich environments such as those recently observed by Swinbank et al. (2010b) and Hailey-Dunsheath et al. (2010) as well as those emerging in cosmological simulations by Agertz et al. (2009) and Davé et al. (2010). The range of 15% - 50% can be taken as a broad constraint on the fraction of merging systems up to $z \sim 1.2$, depending on how merger is defined. These merger fraction estimates imply that the interaction-induced starburst mode is a significant yet unlikely a dominant mode of star formation at intermediate and high z.

Many recent observations support the scenario of extended, non nuclear-concentrated SF at intermediate and high z, specifically that high-z star-forming galaxies lack evidence for interactions and that these galaxies have extended star-forming regions. Targett et al. (2010) find that 95% of optical morphologies of radio/submm galaxies at $z\sim 2$ are consistent with normal disk galaxies, well described by axi-symmetric disk-like models. Similarly, Yuma et al. (2011) find that the UV morphologies of BzK galaxies at $z\sim 2$ that have a single component also show consistent Sérsic indices with those of normal disks. However, we must note that the optical morphological study of galaxies at high-z is a controversial area with contradictory results, such as that of Swinbank et al. (2010a) who find that $z\sim 2$ SMGs have light profiles consistent with a spheroid/elliptical galaxy

light distribution rather than that of exponential disks. Using radio, sub-mm, or mm-wave observations, which are not affected by extinction and old stellar light, various groups also report extended physical sizes for high-*z* star-forming galaxies, U/LIRGs, and submillimeter galaxies (Chapman et al., 2004; Muxlow et al., 2005; Biggs & Ivison, 2008; Bothwell et al., 2010; Casey et al., 2009; Iono et al., 2009; Lehnert et al., 2009; Carilli et al., 2010; Swinbank et al., 2010b; Tacconi et al., 2010; Younger et al., 2010).

Apart from the tests of our L(TIR) indicator in Section 3.4.2, which support our initial assumption that a majority of star-forming galaxies beyond the local Universe reside in the main sequence of star-forming galaxies, the main sequence picture for IR galaxies is also advocated by Elbaz et al. (2011) who find that nearly 80% of IR star-forming galaxies studied by Herschel have the ratio of the 8 μ m luminosity to L(TIR) consistent with being in the extended mode of star formation. A remaining issue is the precise transition scheme from the merger-induced mode of star formation found locally to the extended mode of star formation at high z, which is actually among the fundamental questions in galaxy evolution as it is closely tied to the mechanism of the decline of SFR since $z\sim 1.5$. A theoretical interpretation was provided by Hopkins et al. (2010), but future observations will be required to study this transition definitively.

3.6.3 The Eddington Luminosity of ULIRGs

It has been suggested that local ULIRGs are optically thick to mid-IR photons and radiation pressure may play a role in limiting their maximum luminosity (Thompson et al., 2005; Younger et al., 2008; Thompson, 2009). If the degree of compactness is assumed to be similar for both the local and high-z ULIRGs, the IR emission of high-z ULIRGs with $L({\rm TIR})$ commonly found far above their local counterparts might exceed the Eddington luminosity. Our results ease the con-

cerns about the Eddington limit of ULIRGs at high z for two reasons. First, galaxies at higher L(TIR) are affected by the mid-IR excess to a greater extent. The new indicator would therefore lower the L(TIR) estimates especially for highluminosity galaxies. To test the effects of L(TIR) reduction to the luminosity functions of galaxies, we construct a set of IR LFs of 24 μ m sources at 0 < z < 2.5using the 24 μ m observations from COSMOS (e.g., Sanders et al., 2007) and find that the bright-ends of the LFs in all redshift bins are below $L({\rm TIR})$ of $\sim 10^{13}~L_{\odot}$ (quantitatively, galaxies with L(TIR) above $10^{13} L_{\odot}$ are rarer than $10^{-6}/Mpc^3/dex$ in all redshift bins), which suggests that the maximum L(TIR) of star-forming galaxies is in general less than $10^{13}~L_{\odot}$. Second, the success of the corrections for the size evolution described in Rujopakarn et al. (2011) as well as this work to account for the general IR SED evolution indicate that the great majority of high-z IR galaxies are physically extended, which lowers the optical depth of the galaxy. Both the lower L(TIR) and extended structure imply that high-z ULIRGs are emitting below the Eddington limit and that the maximum L(TIR) of these galaxies is not governed by radiation pressure.

3.7 Chapter Conclusions

The use of single-band mid-IR indicators (such as 24 μ m observations) to estimate $L({\rm TIR})$ has previously been affected by the differences between the structure of local U/LIRGs, upon which the SED templates were constructed, and those of the galaxies in the cosmological surveys being studied. Starbursts in the local U/LIRGs are almost invariably interaction-induced and very compact, while U/LIRGs at high z are typically much more extended, with surface areas $\sim 100 \times {\rm larger}$ than their local counterparts. The resulting larger surface area of the photodissociation regions harboring aromatic emission leads to stronger aro-

matic features at high z mimicking an evolution in aromatic strength as a function of redshift. The ultimate implication of this morphological difference is that single-band mid-IR observations, which at z>1 probe the aromatic-dominated SED region, will overpredict $L({\rm TIR})$ and SFR compared to far-IR measurements if the relationship of local SED templates to $L({\rm TIR})$ is assumed for the calculation of the k- and bolometric corrections.

Following the Rujopakarn et al. (2011) result that $\Sigma_{\rm L(TIR)}$ can serve as a good predictor for the appropriate SED of star-forming galaxies, we determine a new 24 $\mu{\rm m}$ single-band $L({\rm TIR})$ and SFR indicator valid for star-forming galaxies at redshift 0 < z < 2.8 (Equation 3.5 with coefficients in Table 3.4). The resulting 0.02 dex average agreement between $L({\rm TIR})$ estimates from the new single-band 24 $\mu{\rm m}$ indicator and those from multi-band far-IR SED fitting supports the Rujopakarn et al. (2011) result that $\Sigma_{\rm L(TIR)}$ is indeed the dominant factor affecting the SED shapes of star-forming galaxies. Once the $L({\rm TIR})$ is determined, the SFR can be estimated by equations 3.8 and 3.9, respectively.

For the purpose of estimating $L({\rm TIR})$, we recommend the following guidelines. At z<0.1, the indicator presented in this work yields identical $L({\rm TIR})$ estimates to that of Rieke et al. (2009) at all applicable $L({\rm TIR})$, $10^{9.75}-10^{13.00}~L_{\odot}$, and thus either indicator can be used interchangeably. The modifications made in this work only become noticeable at z>0.3. As illustrated by the bottom panel of Figure 3.3, the new indicator carries the extended structure assumption and could underestimate $L({\rm TIR})$ for the minority cases of high-z compact starbursts. If an object is known a priori to be a compact starburst, like local U/LIRGs (e.g., from high-resolution optical or radio interferometric imaging), we therefore recommend readers to apply the bolometric correction factor given by Rieke et al. (2009) in their Equation 14. On the other hand, where the structure of the star-

forming region is not known a priori, we quote an overall scatter of 0.12 dex, given that AGNs are identified and excluded from the sample using X-ray and $3.6-8.0 \mu m$ (i.e. *Spitzer/IRAC*) observations.

We stress that the success of 24 μ m observations as an indicator for L(TIR) and SFR at high z relies on ancillary data (e.g., X-ray and Spitzer/IRAC) to exclude AGN. But given the availability of these data in the current and future deep cosmological surveys where 24 μ m will uniquely provide the deepest unobscured probe of SFR, we do not expect this dependence to be a major limitation.

The new indicator carries an assumption that high z IR star-forming galaxies have extended star-forming region on the order of 4-10 kpc, which is applicable to most galaxies, as indicated by the small, 0.12 dex, scatter. We estimate that only 6% of galaxies out to z=2.8 that do not host AGNs identifiable in X-ray and Spitzer/IRAC observations have nuclear-concentrated starbursts like those found in local U/LIRGs.

We thank Daniel Eisenstein and Pablo Pérez-González for insightful discussions, and J. D. Smith for the $L_{\rm PAH}/L({\rm TIR})$ data. This work is supported by contract 1255094 from Caltech/JPL to the University of Arizona. WR gratefully acknowledges the support from the Thai Government Scholarship.

CHAPTER 4

LBT and Spitzer Spectroscopy of Star-Forming Galaxies at 1 < z < 3: Extinction and Star Formation Rate Indicators¹

We present spectroscopic observations in the rest-frame optical and near- to midinfrared wavelengths of four gravitationally lensed infrared (IR) luminous starforming galaxies at redshift 1 < z < 3 from the LUCIFER instrument on the Large Binocular Telescope and the Infrared Spectrograph on Spitzer. The sample was selected to represent pure, actively star-forming systems, absent of active galactic nuclei. The large lensing magnifications result in high signal-to-noise spectra that can probe faint IR recombination lines, including Pa α and Br α at high redshifts. The sample was augmented by three lensed galaxies with similar suites of unpublished data and observations from the literature, resulting in the final sample of seven galaxies. We use the IR recombination lines in conjunction with $H\alpha$ observations to probe the extinction, A_v , of these systems, as well as testing star formation rate (SFR) indicators against the SFR measured by fitting spectral energy distributions to far-IR photometry. Our galaxies occupy a range of $A_{\rm v}$ from ~ 0 to 5.9 mag, larger than previously known for a similar range of IR luminosities at these redshifts. Thus, estimates of SFR even at $z\sim 2$ must take careful count of extinction in the most IR luminous galaxies. We also measure extinction by comparing SFR estimates from optical emission lines with those from far-IR measurements. The comparison of results from these two independent methods indicates a large variety of dust distribution scenarios at 1 < z < 3. Without correcting for dust extinction, the H α SFR indicator underestimates the SFR; the size

 $^{^1\}mathrm{Originally}$ appeared as Rujopakarn et al. 2012, The Astrophysical Journal, 755, 168

of the necessary correction depends on the IR luminosity and dust distribution scenario. Individual SFR estimates based on the 6.2 μ m polycyclic aromatic hydrocarbon emission line luminosity do not show a systematic discrepancy with extinction, although a considerable, \sim 0.2 dex scatter is observed.

4.1 Introduction

The evolution of the star formation rate (SFR) of galaxies is a central topic to the study of galaxy evolution. It is generally agreed that the SFR density of the Universe has declined by an order of magnitude since $z\sim 1$ to the present (e.g., Le Floc'h et al., 2005; Rujopakarn et al., 2010; Magnelli et al., 2011). The exact epoch of the peak of the SFR history is not known precisely, although it appears to be constrained to be within 1< z<3 (e.g., Pérez-González et al., 2005; Reddy et al., 2008; Rodighiero et al., 2010; Magnelli et al., 2011).

At this redshift range, the primary SFR indicators are based on infrared (IR), optical, and extinction-corrected ultraviolet (UV) observations; the resulting SFR estimates commonly disagree with each other by more than a factor of two (e.g., Reddy et al., 2008). The majority of star formation at these redshifts is known to occur in optically extincted star-forming regions in IR luminous galaxies (e.g., Le Floc'h et al., 2005; Dole et al., 2006; Berta et al., 2011), and the uncertainties resulting from the extinction undermine our ability to understand the SFR history during this era. A better understanding of the SFR history will have important implications on the cosmic stellar mass build-up and metal production. For example, there is a significant discrepancy between the expected metal abundance derived from the SFR history and the observed abundance (Bouché et al., 2007), with some studies indicating the difference to be nearly an order of magnitude, and as a result placing the peak of the SFR history as far back as $z \sim 4$ (Kobayashi

et al., 2007).

The situation necessitates more efforts into exploring the nature of optical extinction in high redshift galaxies using unbiased measures as well as studying the effect of extinction on various SFR indicators.

Extinction measurements based on optical emission lines could be biased in highly obscured environments because the indicator only probes the outer layer of the star-forming regions, where the extinction is relatively low. This effect is observed locally (e.g., Alonso-Herrero et al., 2006), but only because observations are available for longer wavelength IR recombination lines (e.g., $Pa\alpha$ and $Br\alpha$) that are less affected by extinction. In this work, we extend this technique out to z=3 by comparing the strength of the $H\alpha$ line with those of $Pa\alpha$ and $Br\alpha$. Since the latter are in wavelength regions with 10-20 times less extinction than $H\alpha$, they provide a measurement of extinction through the entire star-forming region. With an unbiased estimate of extinction, we can address its effects on SFR indicators in this critical redshift range.

In this paper, we study a wide range of star formation diagnostics in seven gravitationally lensed star-forming galaxies at 1 < z < 3. We observed four of these galaxies spectroscopically with the LUCIFER1 near-IR imaging spectrograph on the Large Binocular Telescope (LBT) to measure the H α line flux in the near-IR, and with the Infrared Spectrograph (IRS, $5-38~\mu m$) on the *Spitzer Space Telescope* to observe the wavelength regions covering Pa α and/or Br α lines as well as aromatic emission lines and emission complexes (commonly attributed to, and hereafter, polycyclic aromatic hydrocarbons or PAH). The sample comprises Abell 2218b, Abell 2667a, Abell 2218a, and Abell 1835a at redshift 1.03, 1.03, 2.52, and 2.57, respectively (magnification $6 \times -27 \times$). The IRS observations at longer wavelengths are further used to compare SFR estimates from the 6.2 μ m

PAH feature. They were carried out under *Spitzer* program ID 82, 30775, 50586 (PI: G. Rieke); and 40443, and 50372 (PI: C. Papovich). Our sample is augmented by three galaxies with similar suites of observations from unpublished data and the literature: SDSSJ120601+5142 (hereafter the Clone), the Lyman break galaxy LBG MS 1512-cB58 (hereafter cB58), and the 8 O'clock arc, at redshift 2.00, 2.73, and 2.73, respectively. Our galaxies were also observed with the MIPS instrument (Rieke et al., 2004) on *Spitzer* at 24 and 70 μ m by Rigby et al. (2008), allowing us to combine the MIPS data with far-IR photometry from the literature to estimate SFR via L(TIR) obtained by fitting the spectral energy distribution (SED) across the peak of the far-IR emission. In addition, we used the 24 μ m monochromatic indicator (Rujopakarn et al., 2012) to estimate L(TIR).

This paper is organized as follows. We discuss the LBT and *Spitzer* observations and data reduction in Section 4.2; extinction, metallicity, L(TIR), and SFR measurements in Section 4.3; compare SFR indicators in Section 4.4; and make concluding remarks in Section 4.5. We assume a Λ CDM cosmology with $\Omega_m = 0.3$, $\Omega_{\Lambda} = 0.7$, and $H_0 = 70 \text{ km s}^{-1}\text{Mpc}^{-1}$ throughout this paper.

4.2 Observations and Data Reduction

Here we describe the selection of our sample (Section 4.2.1); the spectroscopic observations with LBT/LUCIFER along with the near-IR data reduction (Sections 4.2.2 and 4.2.3) and with *Spitzer* (Section 4.2.4); data compilation from the literature (Section 4.2.5); additional photometric observations with *Spitzer* MIPS and the respective data reduction procedure (Section 4.2.6) that results in the final data set for our sample of galaxies.

4.2.1 Sample Selection

To measure extinction and study its implication on the SFR indicators, we need a sample of star-forming galaxies that we understand very well. Gravitationally lensed galaxies are outstanding candidates because their amplified fluxes and images enable high signal-to-noise (S/N) spectroscopy. The candidates for our new observations were drawn from the pool of objects studied by Rigby et al. (2008). Briefly, the Rigby et al. (2008) selection requires that objects have (1) *Spitzer* MIPS 24 μ m flux above 0.4 mJy to be observed efficiently with IRS, (2) morphologies in the optical *Hubble Space Telescope* imaging that exclude members of the lensing cluster, (3) spectroscopic or probable photometric redshift above 1, and (4) lensing magnification above $3\times$. From the Rigby et al. (2008) sample, we further require that candidates are absent of active galactic nucleus (AGN) activity based on X-ray luminosity below 10⁴² erg/s/cm² and the lack of mid-IR power-law SEDs, indicating that their 24 μ m fluxes are not dominated by AGN emission. Apart from the objects selected from the Rigby et al. (2008) sample, we include three additional objects that match the selection criteria; cB58, the Clone, and the 8 O'clock arc. We will discuss these objects in Section 4.2.5.

The galaxies in our sample are located behind galaxy clusters that are well-modeled for mass distribution. The mass model of the Abell 2218 cluster (Kneib et al., 1996) indicates a magnification value for Abell 2218a of 22 ± 2 (Kneib et al., 2004). For Abell 2218b and Abell 2667a, magnification estimates of 6.1 and 17, respectively, are modeled by Rigby et al. (2008). For Abell 1835a, we adopt the magnification estimate from Smail et al. (2005), 3.5 ± 0.5 . The sample is listed in Table 4.1.

Table 4.1. The Sample of High-Redshift Strongly-Lensed Star-Forming Galaxies

Source	z	R.A. (J2000)	Decl. (J2000)	Lensing Magnification	Reference	
Abell 2218b	1.034	16 35 55.16	+66 11 50.8	6.1	1, 2	
Abell 2667a	1.035	23 51 40.00	-26 04 52.0	17	1, 2	
The Clone	2.003	12 06 01.80	+51 42 30.7	27 ± 1	3,5	
Abell 2218a	2.520	16 35 54.18	+66 12 24.8	22 ± 2	1, 2	
Abell 1835a	2.566	14 01 04.96	+02 52 24.8	3.5 ± 0.5	1, 2, 6	
cB58	2.729	15 14 22.29	+36 36 25.7	~ 30	4,7	
8 O'clock	2.731	00 22 40.97	+14 31 14.0	~ 8	8,9	

Note. — References: (1) redshifts from our LBT H α spectroscopy; (2) Rigby et al. (2008); (3) Hainline et al. (2009); (4) Teplitz et al. (2000); (5) Lin et al. (2009); (6) Smail et al. (2005); (7) Seitz et al. (1998); (8) Allam et al. (2007); (9) Finkelstein et al. (2009)

4.2.2 LBT/LUCIFER Near-infrared Spectroscopy

Our near-IR spectroscopy was obtained in three campaigns during 2010 October and 2011 May using the LUCIFER1 instrument on the LBT (Mandel et al., 2007). The common aspects of all these observations are that we use the N1.8 camera with plate scale of 0′25 per pixel and with the 210 lines/mm high-resolution grating, resulting in spectral resolution of 5.0 Å. A-stars were observed for spectrophotometric calibration for each target (details on spectral type below) at similar airmass as the science exposure, either immediately before or after the science exposures. Positions of the LUCIFER slit for each of our observations are shown in Figure 4.1.

Abell 2667a was observed on 2010 November 3 in the longslit spectroscopy mode using a slit of 1″5 by 3.9 arcmin under variable seeing of 1″2 – 2″5. The slit was rotated to P.A. = 320° to place it along the length of the lensed arc. The total integration time was 12×300 s with the telescope nodded 50'' along the slit. The unusually long nodding was required by the $\sim 25''$ length of the arc. For calibration, we observed HD 223466, an A3V calibration star with V = 6.42 mag, through the same setup using a total integration time of 2×20 s in two nodding positions.

Abell 2218b was observed on 2011 March 10 in the longslit spectroscopy mode using a slit of 1″0 by 3.9 arcmin under 0″4 – 0″5 seeing. The slit was rotated to P.A. = 42.5° to place it along the lensed arc, which is $\sim 20''$ long. The arc is 1″9 wide in the widest region; thus we took the spectra at the central position and another position shifted by 0″9, with the 0″1 overlapping allowing for possible pointing errors to prevent a gap in the slit mapping. We will refer to these positions as the "Central" and the "Central+0″9" positions, respectively. The total integration time was 6×300 s at the Central position and 5×300 s at the Central+0″9 position,

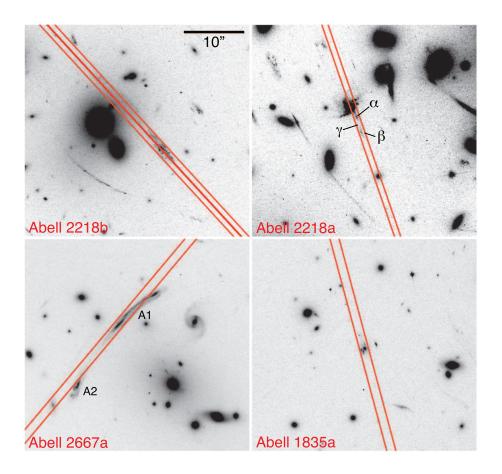


Figure 4.1: Images of the lensed galaxies in our sample from the *Hubble* Space Telescope Advanced Camera for Survey (ACS). The positions of our LBT/LUCIFER slit for NIR spectroscopy shown in red. Clockwise from top-left are Abell 2218b, Abell 2218a, Abell 1835a, and Abell 2667a. The ACS filter for Abell 2218a and Abell 2218b is F625W; Abell 1835 and Abell 2667 images were taken in F850LP. Each image is 37" wide (identical scale in all four panels), north is up, east is left. For Abell 2218a and Abell 2667a, each lensed component is labeled following Kneib et al. (2004) and Sand et al. (2005), respectively

totalling 55 minutes, with the telescope nodded 40'' along the slit for both. An A0V calibration star, HD 145454, with V = 5.43 mag was observed using a total integration time of 2×20 s in two nodding positions.

Abell 2218a was observed on 2011 March 11 in the longslit spectroscopy mode using a slit of 1″0 by 3.9 arcmin under 0″9 - 1″.1 seeing. The slit was rotated to P.A. $= 18.9^{\circ}$ to place it along the lensed arc. The total integration time was 10×300 s with the telescope nodded 20″ along the slit. We observed the same calibration star as for Abell 2218b.

Abell 1835a was observed on 2011 May 7 in the longslit spectroscopy mode using a slit of 1″5 by 3.9 arcmin under 1″0 - 1″1 seeing. The slit was rotated to P.A. $= 15.0^{\circ}$ to place it along the length of Abell 1835a. The total integration time was 12×300 s with the telescope nodded 20″ along the slit. An A2V calibration star, HD 122365, with V = 5.98 mag was observed using a total integration time of 2×20 s in two nodding positions.

We took Ar lamp exposures for wavelength calibration along with dark and flat exposures during daytime.

4.2.3 LBT/LUCIFER Data Reduction

Our near-IR spectral reduction has four steps: sky subtraction, spectral extraction, flux calibration, and line flux measurements. We first use a modified version of an IDL longslit reduction package written by G. D. Becker for NIRSPEC (Becker et al., 2009) to perform sky subtraction following the prescription of Bian et al. (2010). The sky-subtracted 2-dimensional spectra are corrected for the 2D dispersion distortions, wavelength calibrated, and extracted using IRAF. We note that the flexure compensation mechanism of LUCIFER1 was not available during our campaigns, but clean sky subtraction was achieved with the reduction procedure. We combine spectra for each object by averaging values within each

wavelength element with sigma clipping at 2.5σ and then flux calibrate using the xtellcor_general tool (Vacca et al., 2003) and the A-star calibrators described in the previous section. Line fluxes for our objects are measured by integrating the line and subtracting the background estimated from the mean continuum in the spectral range. We estimate the line flux uncertainties by a Monte Carlo simulation done by repeatedly ($n=10^4$) simulating the object's spectrum using random values drawn from the Gaussian distribution centered at the observed flux and σ equal to the observed uncertainties and repeat the line measurement. We take the resulting 1- σ distribution of the simulated line flux values to be the uncertainties for the line flux.

4.2.4 Spitzer IRS Mid-infrared Spectroscopy and Data Reduction

Unpublished *Spitzer* IRS spectroscopy in this work is from: (1) *Spitzer* program 50586 (PI: G. Rieke) to take deep (integration times \sim 15 ks) first order Short-Low spectra (SL1; 7.4 - 14.5 μ m) in the Br α wavelength regions of Abell 2667a and Abell 2218b; (2) *Spitzer* program 40443 (PI: C. Papovich) to take deep (integration time 7 - 14 ks) second order Short-Low spectra (SL2; 5.2 - 7.7 μ m) in the Pa α wavelength regions of Abell 2218a and Abell 1835a. For each of the four objects, the IRS first order Long-Low spectra (LL1; 19.5 - 38.0 μ m) were from GTO programs 82 (Abell 2218a and Abell 1835a) and 30775 (Abell 2218b and Abell 2667a), PI: G. Rieke. The IRS second order Long-Low spectra (LL2; 14.0 - 21.3 μ m) are available for Abell 2218b and Abell 2667a from program 30775, and Abell 1835a from program 82. These data are published in Rigby et al. (2008). The details of IRS observations for our sample are summarized in Table 4.2.

We have reduced all archival spectroscopic data for objects in our sample using the most updated version of the processing software from Level-1 data (BCD)

Table 4.2. Near- and Mid-Infrared Spectroscopic Observations

Source	IRS Exposure Time (ks)				IRS Program ID	Near-IR Spectroscopy	
	SL2 SL1		LL2	LL1			
Abell 2218b		15.1	3.6^{a}	3.6^{a}	30775, 50586	This Work	
Abell 2667a		16.1	$1.9^{\rm a}$	1.9^{a}	30775, 50586	This Work	
The Clone	8.6		$21.6^{\rm b}$	$20.9^{\rm b}$	40430, 50372	Hainline et al. (2009)	
Abell 2218a	14.4 ^c			3.6^{a}	82, 40443	This Work	
Abell 1835a	7.7			3.6^{a}	82, 40443	This Work	
cB58	6.8^{d}	6.8^{d}	14.6°	34.1^{c}	30832	Teplitz et al. (2000)	
8 O'clock	14.4		•••	22.1	40443	Finkelstein et al. (2009)	

Note. — *Spitzer* IRS spectra previously published in (a) Rigby et al. (2008); (b) Fadely et al. (2010); (c) Papovich et al. (2009); (d) Siana et al. (2008)

for IRS by following the prescription of Teplitz et al. (2007). Briefly, first we use IRAF to fit the background slope with time for each row and subtract that fitted value row by row to remove latent charge. Second, we interpolate over bad and/or hot ("rogue") pixels using the IDL routine IRSCLEAN (version 2.1) provided by the SSC based on the known hot pixel mask for the corresponding campaign, plus manual identification. Third, we subtract sky using a sky image constructed from a median of other map positions. Then we co-add each map position into a 2-dimensional (2D) spectrum and use the SPICE software (version 2.4) provided by the SSC to extract a 1-dimensional (1D) spectrum using the optimal extraction template for point sources for each map position. The 1D spectra are combined with sigma clipping at 2.5σ into the final 1D spectra shown in Figures 4.2 and 4.3.

We use the PAHFIT package (Smith et al., 2007) to measure PAH feature fluxes. PAHFIT uses χ^2 minimization to simultaneously fit the PAH and nebular emission lines, stellar and dust continua, as well as the silicate absorption feature. We report the PAH flux measurements in Table 4.3. To define the dust and stellar continuum for the measurement of Pa α and/or Br α line fluxes, we iteratively fit the IRS spectra with PAHFIT and interpolate over points with fit residuals greater than 3σ . This process is repeated until there are no remaining outliers (usually within the $3^{\rm rd}$ iteration) and the final fit, which is effectively a noise-free template representing the object's spectrum, is adopted as a continuum estimate. The actual line flux measurements for both the PAH emissions and recombination lines are done on the original spectra, i.e. only the continua for IR recombination line measurements are determined with this iterative fitting procedure. This method of continuum estimation allows construction of a mid-IR spectral template that best matches each galaxy in a non-parametric manner. In other words, it pro-

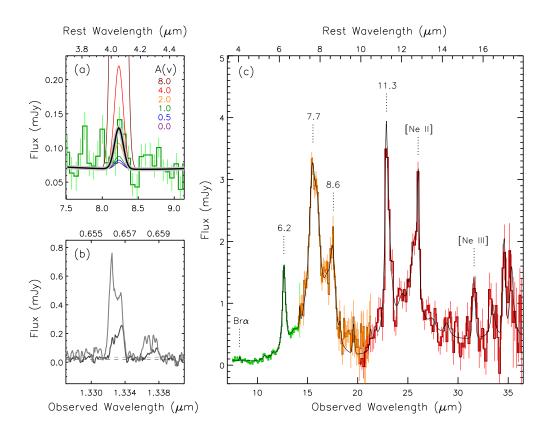


Figure 4.2: Spitzer/IRS mid-IR and LBT/LUCIFER near-IR spectra of Abell 2218b. Panel (a) is the magnified region of IRS SL1 spectrum at the Br α wavelength. The best Gaussian fit to the Br α emission line is the thick black line. The color-coded Gaussians at the Br α line wavelength illustrate the expected Br α line flux for each extinction scenario from $A_{\rm v}$ of 0 to 8.0 mag given the observed H α flux. Panel (b) shows the H α emission line from LBT/LUCIFER. The light and dark gray spectra are extracted from the two parallel slit positions shown in Figure 4.1. A double-peak line profile is clearly visible. The continuum level for each aperture is shown as dashed lines. Panel (c) presents the overall IRS spectra with the green, orange, and red lines representing spectrum from the IRS SL1, LL2, and LL1 modules, respectively.

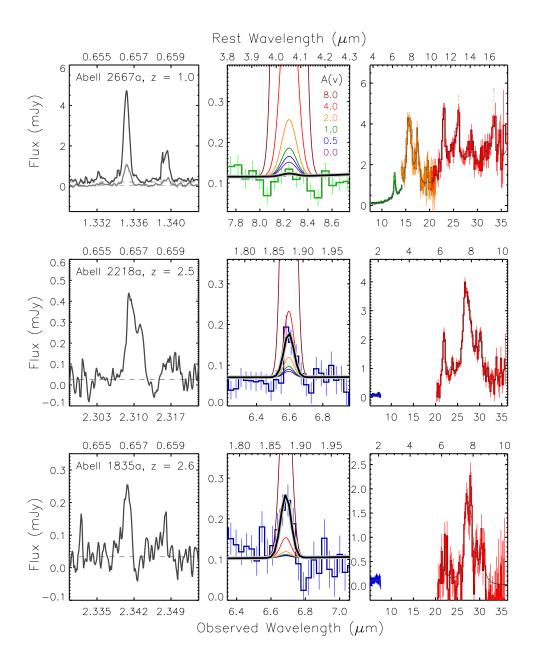


Figure 4.3: Same as Figure 4.2 but for Abell 2667a, Abell 2218a, and Abell 1835a, from top to bottom, respectively. The IRS SL2 module spectra (not available for Abell 2218b in the previous figure), which cover $Pa\alpha$ lines for Abell 2218a and Abell 1835a, are shown in blue. There is no SL1 and LL2 coverage for Abell 2218a and Abell 1835a.

Table 4.3. Measured PAH Fluxes

Source	f(PAH _{6.2})	f(PAH _{7.7 Complex})	f(PAH _{8.6})	f(PAH _{11.3 Complex})	f(PAH _{12.6})
Abell 2218b	15.9 ± 0.2	72.2 ± 1.8	13.2 ± 1.0	17.3 ± 0.7	12.7 ± 0.9
Abell 2667a	13.0 ± 0.2	82.1 ± 3.0	19.9 ± 2.2	21.6 ± 1.3	11.7 ± 1.6
The Clone	7.5 ± 0.3	15.9 ± 0.4	4.2 ± 0.3	4.5 ± 0.7	
Abell 2218a	16.0 ± 0.8	54.4 ± 1.3	10.3 ± 0.8		
Abell 1835a	7.5 ± 1.4	26.1 ± 1.6	7.5 ± 1.9		
cB58	2.9 ± 0.2	9.7 ± 0.5	2.5 ± 0.4		

Note. — PAH emission lines and emission complexes fluxes measured by PAHFIT in 10^{-15} erg/s/cm². These values are not corrected for lensing magnification. Dots indicate that the feature is outside spectral coverage. The 7.7 μ m and 11.3 μ m complexes are the sum of fluxes at wavelength $7.3-7.9~\mu$ m and $11.2-11.4~\mu$ m, respectively. The LL2 spectrum of the 8 O'clock arc does not have sufficient S/N to measure PAH line fluxes consistently.

vides continuum estimates in the $Pa\alpha$ and $Br\alpha$ wavelength regions that are not only constrained by photometric observations (e.g.,, from *Spitzer/IRAC*), but also by PAH-region information. These continuum estimates are shown for each object in Figures 4.2, 4.3, and 4.4.

Br α and Pa α lines are measured by fitting Gaussian profiles with widths fixed at the resolution of the IRS module covering the line, the central wavelengths fixed at the expected line wavelengths based on the optical spectroscopic redshift, and the Gaussian base given by the continuum under the expected wavelength range of the line; the line peak is the only free parameter to fit. The line flux uncertainties are estimated by a procedure similar to that of the H α line flux uncertainties: (1) a series of spectra ($n = 10^4$) were generated randomly based on

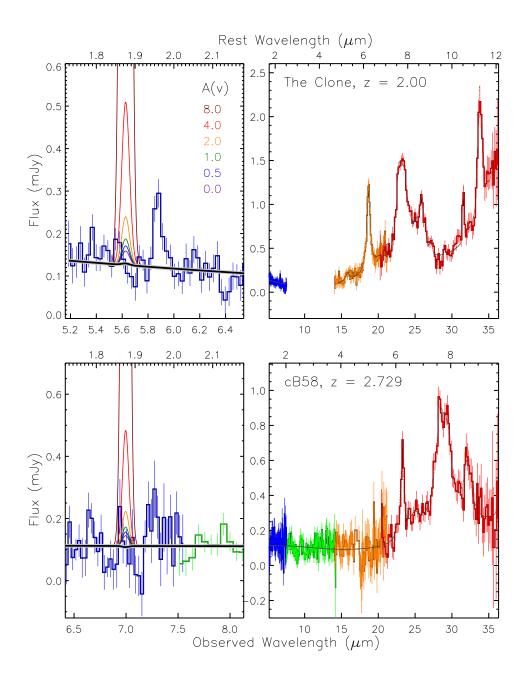


Figure 4.4: Our reduction of the *Spitzer* IRS spectra for the Clone (SDSSJ1206+5142) and cB58 (cf. Fadely et al. (2010) and Siana et al. (2008), respectively). The color coding for IRS modules the line fluxes for each $A_{\rm v}$ scenario is the same as Figures 4.2 and 4.3. We note that the apparent spectral feature at $\sim 5.9 \mu {\rm m}$ (observed frame) in the SL2 spectrum of the Clone cannot be interpreted as a Pa α line at the redshift z=2.00, which has been measured from multiple optical lines (see discussion in Section 4.3.1).

the actual spectra and the σ uncertainties; (2) line flux measurements are carried out on them; and (3) we take the 1- σ value of the simulated flux distribution to be the uncertainties for the line flux. If the formal fit to the line yields negative line flux due to non-detection (occurring in two cases, cB58 and The Clone), we adopt the 1- σ value as an upper limit to the line flux. The measurements are reported in Table 4.4.

4.2.5 Archival and Literature Data

We augmented our sample with three additional objects: The Clone, cB58, and the 8 O'clock arc. These objects have suites of data similar to our sample: rest-frame optical spectroscopy covering $H\alpha$ and deep IRS spectroscopy covering $Pa\alpha$ (Table 4.1).

cB58 (Yee et al., 1996), at redshift z=2.729, is the first lensed LBG known with high magnification (\sim 30×); it has been studied extensively from UV to millimeter wavelengths (Siana et al. 2008, and references therein). Rest-frame optical spectroscopy was obtained by Teplitz et al. (2000). Siana et al. (2008) present a full suite of IRS observation (SL2, SL1, LL2, and LL1) for the galaxy. We re-reduced these IRS data using our procedure above and found the result to be consistent with the original reduction published in Siana et al. (2008); details are given in Section 4.3.1. The lensing magnification of cB58, \sim 30×, was from Seitz et al. (1998).

The Clone, at redshift z=2.0026 was discovered from SDSS imaging (Lin et al., 2009). Its rest-frame optical spectroscopy was obtained by Hainline et al. (2009). IRS observations in the LL2 and LL1 bands were obtained by Fadely et al. (2010), who concluded that the Clone's IR emission is dominated by a starburst based on the strength of the 6.2 μ m PAH feature, despite the object showing a

Table 4.4. Measured Fluxes

Source	f (24 μ m)	f(70 μm)	$f(\mathrm{H}lpha)$	f([NII] 6583)	$f(\mathrm{Pa}lpha)$	$f({ m Br}lpha)$	f[Ne II 12.8]	f[Ne III 15.5]
	(1)	(2)	(3)	(4)	(5)	(6)	(7)	(8)
Abell 2218b	1.67	7.4 ± 1.5	21.2 ± 0.6	5.2 ± 0.5		4.3 ± 0.9	1.8 ± 0.2	0.9 ± 0.2
Abell 2667a	4.52	19.4 ± 3.9	78.7 ± 1.5	31.1 ± 3.2		0.4 ± 1.0	2.8 ± 0.4	0.9 ± 0.3
The Clone	0.88	8.8 ± 1.8	$20.2\pm0.5^{\mathrm{a}}$	$3.9 \pm 0.2^{\rm a}$	< 1.3			
Abell 2218a	1.16	< 7	6.2 ± 0.3	1.5 ± 0.3	5.7 ± 1.2			
Abell 1835a	0.99	< 13	1.8 ± 0.3	1.0 ± 0.3	7.9 ± 1.5		•••	•••
cB58	$0.24^{ m b}$	$1.7\pm1.0^{\rm b}$	$12.6\pm0.4^{\rm c}$	$1.1\pm0.3^{\rm c}$	< 2.3	< 1.3		•••
8 O'clock	0.57		$17.6 \pm 0.5^{\rm d}$	$4.8 \pm 0.4^{\rm d}$	11.5 ± 2.2			•••

Note. — Col. (1) 24 μ m flux in mJy. $f(24~\mu\text{m})$ of Abell galaxies except Abell 2667a are from Rigby et al. (2008), who noted that DAOPHOT errors of the flux are overly optimistic and thus not reported. A nominal uncertainty of 0.1 mJy is adopted for SED fitting for L(TIR). Rigby et al. (2008) mistakingly reported a $f(24~\mu\text{m})$ for only one component of the A2667 arc. A correct value is reported here; Col. (2) 70 μ m flux in mJy; Col. (3)-(4) optical line fluxes in $10^{-16}~\text{erg/s/cm}^2$; Col. (5)-(6) IR recombination lines fluxes in $10^{-16}~\text{erg/s/cm}^2$. The formal fit to the Br α line of cB58 yields a flux value of $(-0.4 \pm 1.3) \times 10^{-16}~\text{erg/s/cm}^2$ and hence a 1σ limit is reported in the Table. Also for the Pa α line, the formal fit yields $(-0.2 \pm 2.3) \times 10^{-16}~\text{erg/s/cm}^2$ and hence the 1σ limit is reported. Likewise, a 1σ limit is reported for the Pa α line flux of The Clone, where a formal fit yields $(0.3 \pm 1.3) \times 10^{-16}$; Col. (7)-(8) Line fluxes of [Ne II] 12.8 μ m and [Ne III] 15.5 μ m in $10^{-15}~\text{erg/s/cm}^2$ measured by PAHFIT. Dots indicate no spectral coverage. These values are not corrected for lensing magnification. Flux references: (a) Hainline et al. (2009); (b) Siana et al. (2008); (c) Teplitz et al. (2000); (d) Finkelstein et al. (2009).

very strong [SIV] emission line. The Clone's deep IRS SL2 observation is a part of *Spitzer* program 50372 (PI: C. Papovich) with an integration time of 8.6 ks. As with cB58, we re-reduced all IRS data using our procedure and software to ensure consistency. We present our reduction of these archival data in Figure 4.4. The lensing magnification for the Clone, $27 \pm 1 \times$, was reported by Lin et al. (2009).

The 8 O'clock arc, at redshift z=2.7308 was discovered serendipitously from SDSS imaging by Allam et al. (2007). Finkelstein et al. (2009) obtained the restframe spectroscopy of components 'A2' and 'A3' in the nomenclature of Allam et al. (2007). The arc was observed as a part of *Spitzer* program 40443 (PI: C. Papovich) with an SL2 integration time of 14.4 ks. The slit for the SL2 observation is centered on the 'A2' component and covered significant parts of both the 'A1' and 'A3' components such that any bias due to spatial variation of recombination lines along the lensed arc will be negligible. The PAH spectrum of the 8 O'clock arc shows $6.2~\mu m$ and $7.7~\mu m$ emission features, yet at low S/N due to contamination in the IRS slit from a nearby IR-bright dust-obscured galaxy, which we will discuss in the next section. We adopt the magnification estimate of $8\times$ for the arc (Finkelstein et al., 2009).

4.2.6 Additional *Spitzer* MIPS Photometry and Data Reduction

The *Spitzer* MIPS 24 and 70 μ m photometry for objects behind the Abell clusters are taken from Rigby et al. (2008) with exception of Abell 2667a, whose 70 μ m photometry is reported as an upper limit in Rigby et al. (2008) but which was re-observed with longer integration time in *Spitzer* program ID 50586 (PI: G. Rieke). For the Clone, we downloaded the 24 and 70 μ m data observed as part of programs 40430 (PI: S. Allam) and 50372 (PI: C. Papovich). The *Spitzer* MIPS observations for the 8 O'clock arc were obtained under program 40443 (PI: C. Papovich).

We measured the 24 and 70 μ m fluxes from the Level-2 (PBCD) data using the Starfinder IDL routine (Diolaiti et al., 2000) to perform PSF photometry. The PSF model was generated using the STinyTim routine provided by the SSC and smoothed according to a prescription given by Engelbracht et al. (2007) to better match the observed PSF. We require $\sigma=3$ and the PSF correlation value of 0.75 for our 24 and 70 μ m flux measurements. The 8 O'clock arc has a 24 μ m-bright dust-obscured galaxy $\sim 6'\!5$ away that partially blends with the arc, but we were able to deblend the flux by performing PSF photometry to subtract the intervening source first and repeat the photometry to measure the flux of the arc. This contaminating galaxy is highly extincted, such that it is undetected in the SDSS imaging and was discovered only in the 24 μ m observation. Our flux measurements along with fluxes from the literature are reported in Table 4.4.

4.2.7 Augmented Sample Summary

Our augmented sample consists of the four galaxies we observed plus the three from the literature. In addition to the measurements of H α and of at least one of the IR recombination lines (Pa α and/or Br α), all of them have good 24 μ m photometry, far-IR and sub-mm photometry as well as IRS spectroscopy covering, at least, the 6 - 8 μ m wavelength region. The IRS coverage goes out to nearly 17 μ m (rest-frame) in the two lowest redshift objects (Abell 2667a and Abell 2218b, $z\sim 1.0$).

4.3 Results

In this section, we describe the near- and mid-IR spectra and the derived physical quantities, including metallicity, $L({\rm TIR})$ and SFR from optical and IR tracers, and extinction measurements.

4.3.1 Near- and Mid-IR Spectroscopy

The final 1D H α spectra from our LBT/LUCIFER1 observations are shown in Figures 4.2 and 4.3 along with the IRS spectra. The 6.2 μ m PAH emission line, 7.7 μ m complex, and 8.6 μ m complex are clearly detected in all galaxies.

The spectra from both slit positions (Section 4.2.2) of Abell 2218b show highly asymmetric line profiles. The profile at the central position is double-peaked in both H α and [NII] while the central+0'9 spectrum shows a single-sided profile with stronger emission at the red side of the line. The combined line profile from both slit positions is well fitted with a double Gaussian, whose deconvolved spectral width (corrected for instrumental resolution) indicates a velocity dispersion of 163 ± 3 km/s. Traces of the arc northeast of the main component hinted in the ACS image are not detected at H α . The IRS spectrum for Abell 2218b shows a strong [Ne III] 15.56 μ m line as well as the [Ne II] line at 12.81 μ m, apart from other PAH features. The Br α line is detected at 4.8σ with line flux of $4.3 \pm 0.9 \times 10^{-16}$ erg/s/cm².

The spectra of Abell 2667a were extracted from two apertures in the slit. Both of these positions are very bright in H α . Referring to Figure 4.1, these apertures are at (1) the main arc north-northeastern of the brightest cluster galaxy (BCG) (identified as 'A1' by Sand et al. (2005), and in Figure 4.1); and (2) the smaller arc east of the BCG (the 'A2' arc in the Sand et al. study). Although it appears that a part of the smaller arc is outside the slit in the optical image, the H α line is clearly detected (the light gray spectrum in Figure 4.3 top row, left column). Both apertures show the same profile for both H α and [NII] lines. No velocity shift between the two components is observed. The formal fit to the Br α line yields a flux of $(0.4 \pm 1.0) \times 10^{-16}$, a non-detection. The galaxy has the warmest dust continuum among our samples, as seen in the rising SED towards the red

end of the IRS spectrum in Figure 4.3 (cf. Abell 2218b's continuum in Figure 4.2). However, the strong PAH emission is inconsistent with the system's emission being dominated by an AGN in the mid-IR. Its $\log([NII]/H\alpha)$ line ratio of -0.40 alone (i.e., without the [OIII] and H β) does not unambiguously support or rule out the presence of a weak narrow-line AGN. But even with the presence of a weak, optically selected AGN, the EW of the 6.2 μ m PAH emission could still serve as a good tracer of SFR because the suppression of PAH emission due to AGN is found to be limited to the nuclear region (Diamond-Stanic & Rieke, 2010).

The H α line of Abell 2218a also shows a double-peaked profile indicating a velocity dispersion of 188 ± 5 km/s. The galaxy has been a subject of a previous near-IR spectroscopic study by Richard et al. (2011). Our slit orientation, however, is different (see their Figure 1); they excluded the β and γ components (the former being a major component) in the nomenclature of Kneib et al. (2004), as shown in Figure 4.1, while our slit orientation covers all the main components (α , β and γ). The Pa α observation, which targets the β component, detected Pa α line at 4.8σ with line flux of $5.7 \pm 1.2 \times 10^{-16}$ erg/s/cm². This measurement is consistent with the previously published reduction of the same data by Papovich et al. (2009) who measured the line flux to be $8.5 \pm 1.4 \times 10^{-16}$ erg/s/cm². We attribute the small difference in the two measurements to the different definition of the continuum: Papovich et al. (2009) defined their continuum with IRAC photometry whereas our reduction adopted the simultaneous multi-component fit of spectral features described in Section 4.2.4.

Abell 1835a shows a faint H α line, too faint to measure asymmetry in the line profile, but a bright Pa α line with a flux of 7.9 \pm 1.5 \times 10⁻¹⁶ erg/s/cm². This is the second brightest Pa α detection in our sample, after the 8 O'clock arc, whose Pa α flux is 11.5 \pm 2.2 \times 10⁻¹⁶ erg/s/cm². The LL1 PAH spectrum of the

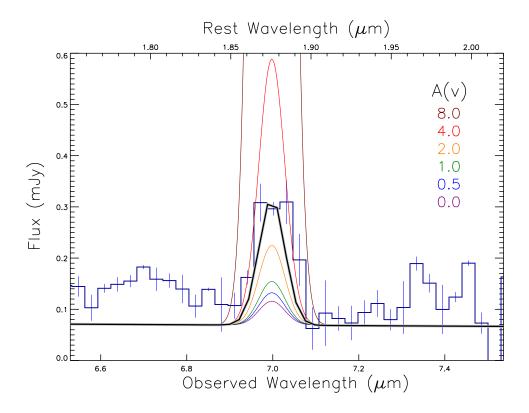


Figure 4.5: *Spitzer* IRS SL2 spectrum for the 8 O'clock arc, showing the Pa α line. The color coding for IRS module and the line fluxes for each extinction scenario are the same as Figures 4.2, 4.3, and 4.4.

8 O'clock arc does not have sufficient S/N to use PAHFIT to construct a noise free spectrum as a template for the Pa α line flux measurement (Section 4.2.4) due to the contamination from the nearby IR-bright dust-obscured galaxy, thus instead the continuum of the arc for the measurement is defined by interpolating between the IRAC 5.0 and 8.0 μ m photometric points. These IRAC observations yield fluxes of 74 ± 3 and 64 ± 4 μ Jy for the 5.8 and 8.0 μ m bands, respectively. We present the Pa α spectrum of the 8 O'clock arc in Figure 4.5.

For the two IRS spectra from the literature, the Clone and cB58, our reduction generally agrees with those published previously by Fadely et al. (2010) and Siana

et al. (2008), respectively. Small differences are noted in the PAH line fluxes due to the way that the continuum for the fit is defined. PAHFIT uses multi-component dust features to represent the continuum, while a single-component power-law is used by Fadely et al. and Siana et al. Their approach resulted in a similarly good fit to the data compared to ours, although the measured PAH flux could differ, as observed in the Clone's PAH fluxes from the $6.2-11.3~\mu m$ features where the Fadely et al. (2010) values are a factor of 2.6 - 3.7 larger than ours. Fadely et al. reported that their results are a factor of 1 - 8 higher than those of Brandl et al. (2006) in their re-reduction of the same data set. Brandl et al. use a continuum level defined on either side of the emission features and thus their PAH fluxes will be systematically smaller than with either our PAHFIT measurement or the single component continuum method. That is, we expect the measurements of the PAH line flux from the same data to yield flux values in the following increasing order: Brandl et al., PAHFIT, and Fadely et al./Siana et al., which is consistent with the differences we find. The formal Pa α line fit for cB58 yields a flux of $(-0.2 \pm 2.3) \times$ 10^{-16} erg/s/cm², from which we determined the Pa α flux limit to be $< 2.3 \times 10^{-16}$ erg/s/cm², which agrees with the non-detection reported by Siana et al. (2008), < 6×10^{-16} erg/s/cm². The formal Br α line fit yields a line flux of $(-0.4 \pm 1.3) \times 10^{-16}$ erg/s/cm², thus we report a limit of $< 1.3 \times 10^{-16}$ erg/s/cm².

The formal fit to $Pa\alpha$ line flux of the Clone yields $(0.3\pm1.3)\times10^{-16}$ erg/s/cm², from which we report an upper limit similar to that of cB58 above. In the panel showing the $Pa\alpha$ wavelength region for the Clone in Figure 4.4, we note a spectral feature at 5.9 μ m (1.96 μ m rest-frame) that resembles a $Pa\alpha$ line at $z\sim2.1$. However, the spectroscopic redshift of 2.0026 was measured with multiple optical lines (Hainline et al., 2009) and thus precludes the possibility of the feature being interpreted as the $Pa\alpha$ line. It is also unlikely to be an H_2 emission line at

1.96 μ m given the absence of other H₂ lines nearby (2.03 and 2.12 μ m). The source of the apparent feature therefore remains unknown.

4.3.2 Metallicity

We estimate metallicity with the N2 index (Pettini & Pagel, 2004) using both linear and 3rd-order fits (Table 4.5). The index is not affected by the optical extinction given the proximity of the lines. Both estimators yield consistent values, which agree well with those found by Erb et al. (2006) for massive galaxies at $z \gtrsim 2$ selected via UV luminosity. The range of the metallicity found in our sample is also in good agreement with the sample of 28 lensed galaxies at 1.5 < z < 5 observed by Richard et al. (2011), $8.00 \ge Z \ge 8.94$, with an average oxygen abundance of Z = 8.55, similar to the average value from the linear N2 index in this work, Z = 8.56. That is, our sample has typical oxygen abundance for field and lensed galaxies at similar z.

4.3.3 Infrared Luminosity and Star Formation Rate

We can measure the star-formation rate (SFR) from $L(\mathrm{TIR})$, which in turn can be estimated by three tracers: (1) far-IR SED fitting, (2) the monochromatic 24 $\mu\mathrm{m}$ $L(\mathrm{TIR})$ estimator given by Rujopakarn et al. (2012), and (3) PAH emission line luminosity. The SFR can also be estimated from the H α luminosity as well as the combination of H α and 24 $\mu\mathrm{m}$ luminosity. We adopt the SFR derived from the SED-fitted $L(\mathrm{TIR})$ as a fiducial for comparison. SFRs are calculated from $L(\mathrm{TIR})$ by the relationship given by Rujopakarn et al. (2012). All SFR estimates are converted from their respective IMF assumptions to the Kroupa (2002) IMF. The SFR results are presented in this section and their implications are discussed in Section 4.4.

Table 4.5. Metallicity Estimates from [NII]/H α

Source	Z _{PP04} (1)	Z _{PP04, 3rd order (2)}		
Abell 2218b	8.55 ± 0.04	8.53 ± 0.10		
Abell 2667a	8.67 ± 0.05	8.73 ± 0.10		
 1 01				
The Clone	8.49 ± 0.02	8.45 ± 0.07		
Abell 2218a	8.55 ± 0.10	8.52 ± 0.25		
Abell 1835a	8.75 ± 0.15	8.91 ± 0.33		
-DE0	0.21 0.10	0.26 0.25		
cB58	8.31 ± 0.10	8.26 ± 0.35		
8 O'clock	8.58 ± 0.04	8.57 ± 0.09		

Note. — Values are in 12+ log(O/H). Col. (1) Metallicity estimates from the N2 linear formula provided by Pettini & Pagel (2004); Col. (2) Metallicity estimates from the N2 3rd-order estimator from Pettini & Pagel (2004).

The far-IR SED fitting (e.g., 30 μ m to \sim 1 mm) is the most straightforward among the methods to measure L(TIR). However, far-IR photometry is often affected by confusion noise at longer wavelengths in crowded fields, thus limiting the applicability of far-IR SED fitting in deep cosmological surveys. The far-IR and sub-mm photometry in our sample is aided by magnification of the gravitational lenses and thus we can probe fluxes below the typical confusion limit of the instrument. The SED fitting for the L(TIR) for Abell 2218b and Abell 1835a were carried out by Rigby et al. (2008) by combining the 24 and 70 μ m data with submillimeter observations, including at least 450 and 850 μ m for all their galaxies and additionally 1.3 mm for Abell 1835a. The value for Abell 2218a is measured using Herschel observations by Finkelstein et al. (2011). The SED-fitted L(TIR)for the Clone and cB58 were from the Fadely et al. (2010) and Siana et al. (2008) studies, respectively. Abell 2667a and the 8 O'clock arc have no L(TIR) estimates from far-IR SED fitting because the longest band we presently have is 70 μ m. The 70 μ m imaging for the latter is complicated by the nearby bright dust-obscured galaxy (Section 4.2.6) that blends with the arc.

The monochromatic (i.e., single-band) $24~\mu m~L({\rm TIR})$ estimator from Rujopakarn et al. (2012) yields $L({\rm TIR})$ consistent with the far-IR SED fitting at 0 < z < 2.8 within 0.02 dex, on average, with a scatter of 0.12 dex for individual star-forming galaxies. Rujopakarn et al. (2012) take into account the evolution of the bolometric correction from local galaxies out to z=2.8 (the farthest redshift where the 24 μ m band traces predominantly dust and PAH emissions) due to the structural differences of IR galaxies by using the IR surface brightness, $\Sigma_{\rm L(TIR)}$, as an indicator of IR SED, which has been demonstrated by Rujopakarn et al. (2011). Specifically, high-z IR galaxies are physically extended and typically have $100-1000\times$ more surface area than local counterparts at similar $L({\rm TIR})$ (Rujopakarn et al., 2011),

and thus larger PAH-emitting area, which affects the bolometric corrections in the PAH wavelength region that is probed by the 24 μ m band, particularly at z>1 (Rujopakarn et al., 2012). We report the values of L(TIR) from this 24 μ m indicator along with those from SED fitting in Table 4.6. The agreement between the monochromatic indicator and the far-IR SED fitting is within 0.12 dex (average difference of 0.06 dex), similar to the agreement reported in Rujopakarn et al. (2012). No systematic trends in redshift, luminosity, or metallicity are observed.

The last L(TIR) estimator is derived via the luminosity of the 6.2 μ m PAH emission line, following the relationship given by Pope et al. (2008), which was measured by combining a local sample from Brandl et al. (2006) and the results for their sub-millimeter galaxies (SMGs). Pope et al. (2008) report a slope of the relationship between log 6.2 μ m PAH luminosity and log L(TIR) to be approximately unity (formal slope = 1.01 ± 0.01) over L(TIR) ranging from $10^{10} - 10^{13} L_{\odot}$. Our objects are shown in Figure 4.6 on top of data points from Pope et al. (2008) and Brandl et al. (2006). The 24 μ m L(TIR) values are used here instead of those from the far-IR SED fitting because Abell 2667a has no far-IR L(TIR) estimate. Because of the methodological differences in the PAH flux measurements between Pope et al. (2008) and ours, particularly the assumption of the continuum level, for the purpose of the comparison in Figure 4.6, we normalize the PAH luminosity by a factor determined by matching our 6.2 μ m PAH luminosity of cB58 to the measurement of the same object by Siana et al. (2008), who adopt the same continuum assumption as Pope et al. (2008). The 6.2 μ m PAH feature was chosen to represent the aromatic emissions over other stronger PAH emission lines and emission complexes because it is narrow and relatively isolated from other lines, which mitigates the systematic uncertainties introduced by the process of deblending contributions from adjacent lines (which is required for, e.g., the 7.7

Table 4.6. Derived Quantities

Source	LIR	$L(\log L_{\odot})$		SFR ($\mathcal{M}_{\odot}/\mathrm{yr}$)					$A_{ m v}^{ m IR}$	$A_{ m v}$
	$24~\mu\mathrm{m}$	Far-IR SED	$H\alpha$	${\rm H}\alpha$ + 24 $\mu{\rm m}$	$PAH_{6.2} \mu m$	$LIR_{24} \mu m$	$LIR_{\mathrm{Far-IRSED}}$			
	(1)	(2)	(3)	(4)	(5)	(6)	(7)	(8)	(9)	(10)
Abell 2218b	11.69	11.68	10.3	36.6	66.7	48.0	46.8	2.8 ± 0.3	2.1	2.5
Abell 2667a*	11.68	•••	13.9	39.9	19.4	47.1	•••	- 2.4*± 3.1	1.7	-0.4
The Clone [†]	11.20	11.38	11.4	20.0	36.2	15.1	23.2	$< -1.1^{\dagger}$	1.0	1.0
Abell 2218a	11.81	11.83	7.5	42.3	170.2	63.8	66.5	3.3 ± 0.4	3.0	3.2
Abell 1835a	12.71	12.83	14.5	298	558.2	561	752	5.9 ± 0.4	5.4	5.7
$cB58^{\dagger}$	11.04	11.04	13.6	19.8	26.6	10.4	10.4	$< 0.7^{\dagger}$	-0.4	-0.4
8 O'clock	12.17		71.5	154		149		2.8 ± 0.3	1.0	1.9

Note. — * IR recombination line detected at low significance; † IR recombination line not detected; Quantities in this table are corrected for lensing magnification. Col. (1) L(TIR) estimated from the monochromatic 24 μ m indicator from Rujopakarn et al. (2012); Col. (2) L(TIR) measured by fitting SED to far-IR and sub-mm photometry. The values for Abell 2218b and Abell 1835a are from Rigby et al. (2008). The values for Abell 2218a, the Clone and cB58 are from Finkelstein et al. (2011), Fadely et al. (2010) and Siana et al. (2008), respectively.; Col. (3) H α SFR estimated by the Kennicutt (1998) formula (no extinction correction); Col. (4) Extinction-corrected SFR estimated using the H α and rest-frame 24 μ m luminosity formula provided by Kennicutt et al. (2009); Col. (5) Col. SFR estimated by the PAH 6.2 μ m complex luminosity; (6) SFR estimated by 24 μ m monochromatic indicator provided by Rujopakarn et al. (2012); Col. (7) SFR estimated using the Far-IR L(TIR) in Col. (2) and the relationship given by Rujopakarn et al. (2012); Col. (8) Screen extinction $A_{\rm v}$ in mag estimated with H α and IR recombination lines assuming case-B recombination scenario. The value for cB58 uses H α and the Pa α line, the Br α limit for cB58 indicates an extinction limit of $A_{\rm v} < 1.8$ mag.; Col. (9) $A_{\rm v}^{\rm IR}$ in mag. See Section 4.3.4 for more details.; Col. (10) Final extinction estimate from averaging values in Col (8) and (9). For cB 58 and The Clone, the $A_{\rm v}^{\rm IR}$ values are adopted.

 μ m complex and 8.6 μ m line). To estimate the SFR from the 6.2 μ m PAH luminosity, the PAH luminosity is first converted to L(TIR) via the Pope et al. (2008) conversion and then to SFR via the Rujopakarn et al. (2012) relation.

In addition to estimating SFR via L(TIR), we also show: the Kennicutt (1998) formula for H α (no extinction correction) and the Kennicutt et al. (2009) indicator that combines H α and the rest-frame 24 μ m luminosity in order to correct for dust extinction in the SFR estimates. The SFR estimates from each method are tabulated in Table 4.6. We discuss the effects of extinction on the SFR estimates in Section 4.4.

4.3.4 Extinction

Extinctions derived from optical lines (e.g., $H\alpha/H\beta$) could suffer systematic underestimation where the overall extinction is large and the dust is mixed with the sources. This possibility can be tested with IR recombination lines which are more robust to high extinction (Alonso-Herrero et al., 2006). To obtain a fiducial estimate, we assume a foreground screen and measure the extinction relative to $H\alpha$ using the $Pa\alpha$ and $Pa\alpha$ lines assuming case-B recombination. For instance, for $Pa\alpha$, the $Pa\alpha$ are given by

$$\frac{I_{\text{Br}\alpha}}{I_{\text{H}\alpha}} = \frac{I_{\text{Br}\alpha,0}}{I_{\text{H}\alpha,0}} \exp\left[-\frac{A_{\text{v}}^{\text{H}\alpha/Spitzer}}{1.086}(A_{\text{Br}\alpha} - A_{\text{H}\alpha})\right]$$
(4.1)

where $I_{\rm Br\alpha,0}/I_{\rm H\alpha,0}=0.0291$ and for Pa α , $I_{\rm Pa\alpha,0}/I_{\rm H\alpha,0}=0.1226$ (Osterbrock & Ferland, 2006) for T $_e=10,000$ K at the low-density limit. The $A_{\rm H\alpha}$, $A_{\rm Pa\alpha}$, and $A_{\rm Br\alpha}$ are given by interpolation using the Rieke & Lebofsky (1985) extinction law, which for $A_{\rm v}$ of 1 mag are 0.8 mag, 0.15 mag, and 0.04 mag, respectively.

Alternatively, the extinction can be estimated from the optical and IR SFR values by taking the latter to be a fiducial SFR. The assumption is secure in our sample of IR luminous galaxies, where direct UV leakage from the galaxy is expected

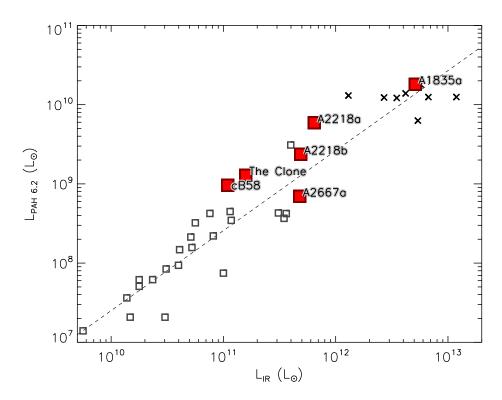


Figure 4.6: The relationship of 6.2 μ m PAH emission line luminosity to L(TIR) in our sample (large red squares) compared to the local star-forming galaxies and LIRGs from the Brandl et al. (2006) study (squares) and the high-redshift sub-mm galaxies from Pope et al. (2008) (crosses). The dashed line is a linear relationship between log luminosities with slope of 1.01 measured by Pope et al. (2008). Our galaxies fall within this relationship, confirming the approximately unity slope reported by Pope et al. at the intermediate luminosities between the local and SMG samples.

to be small (Rieke et al. 2009 and references therein). This alternative extinction estimate, $A_{\rm v}^{\rm IR}$, following Choi et al. (2006) is

$$A_{\mathrm{H}\alpha}^{\mathrm{IR}} = 2.5 \log \left(\frac{\mathrm{SFR}_{\mathrm{IR}}}{\mathrm{SFR}_{\mathrm{H}\alpha}} \right)$$
 (4.2)

The $A_{\rm H\alpha}^{\rm IR}$ can then be converted to the $A_{\rm v}^{\rm IR}$ via the Rieke & Lebofsky (1985) extinction law. When available, we use the far-IR SFR_{IR} to calculate the $A_{\rm v}^{\rm IR}$, otherwise the value estimated from the 24 μ m $L({\rm TIR})$ is used.

The $A_{\rm v}^{{\rm H}\alpha/Spitzer}$ method assumes a foreground screen of dust and therefore is a lower limit, whereas the $A_{\rm v}^{{\rm IR}}$ does not. The comparison of measurements from both methods, tabulated in Table 4.6, shows that in three out of four galaxies where IR recombination lines are well detected (Abell 2218b, Abell 2218a, and Abell 1835a), both methods agree within the range of uncertainty, which suggests that the nature of the dust distribution in these galaxies is roughly uniform, resembling the the foreground screen assumption. The other object with a well-detected Pa α (the 8 O'clock arc), however, shows a 1.8 mag difference between $A_{\rm v}^{{\rm H}\alpha/Spitzer}$ and $A_{\rm v}^{{\rm IR}}$. The latter disagreement indicates an inhomogeneous mixture of dust in the 8 O'clock arc and highlights the diversity of the dust distribution scenarios at redshift 1 < z < 3.

Abell 2218a, Abell 1835a, cB58, the Clone, and the 8 O'clock arc have extinction measurements from optical and/or rest-frame optical spectroscopy in the literature that can be compared with our IR measurements. Richard et al. (2011) found $E(B-V)_{\rm star}$ of 0.18 for Abell 2218a from SED fitting, implying $A_{\rm v}$ of 0.6 mag, assuming the R=3.1 law. Abell 1835a has extinction measurements by Nesvadba et al. (2007) using H α /H β ratio of E(B-V)=1.3-1.6, implying $A_{\rm v}$ of 4.0 – 5.0 mag. Teplitz et al. (2000) measured E(B-V) of 0.27 for cB58 from the H α /H β line ratio, implying $A_{\rm v}$ of 0.4 mag. For the Clone, Hainline et al. (2009) measured E(B-V) using the H α /H γ line ratio to be 0.28, which implies $A_{\rm v}$ of

0.9 mag. The extinction of the 8 O'clock arc was measured by Finkelstein et al. (2009) using weighted mean of $H\alpha$, $H\beta$, and $H\gamma$ line ratios to be $A_{\rm v}=1.17\pm0.36$ mag (using only $H\alpha/H\beta$ yields $E(B-V)_{\rm gas}$ of 0.97, implying $A_{\rm v}$ of 1.3 mag); and by Dessauges-Zavadsky et al. (2011) to be $E(B-V)_{\rm gas}=0.30\pm0.04$ mag, implying $A_{\rm v}$ of 0.9 mag. From Table 4.6, the extinction measurements from IR recombination lines for Abell 2218a, Abell 1835a, and the 8 O'clock arc, where we have secure IR line detections are 3.3 ± 0.4 mag, 5.9 ± 0.4 mag, and 2.8 ± 0.3 mag, respectively. While our sample size is too small to draw a general conclusion, the comparison suggests that the optical measurements may sample systematically lower extinction regions, in agreement with local LIRGs and ULIRGs (e.g., Alonso-Herrero et al., 2006).

The $A_{\rm v}^{{\rm H}\alpha/Spitzer}$ values for Abell 2667a and the Clone are negative because the formal fits to the Pa α and Br α line yield values (or flux limits) lower than those expected for the extinction of 0 mag (as shown in the simulated $A_{\rm v}$ in Figures 4.3 and 4.4); the line is undetected), albeit with a considerable uncertainty. For cB58, the line flux for both Pa α and Br α are negative and thus the $A_{\rm v}^{{\rm H}\alpha/Spitzer}$ cannot be formally calculated and we report a 1- σ upper limit as cB58's $A_{\rm v}^{{\rm H}\alpha/Spitzer}$. Given the general agreement between $A_{\rm v}^{{\rm H}\alpha/Spitzer}$ and $A_{\rm v}^{{\rm IR}}$ in a majority of objects with secure measurements of Pa α and Br α , we adopt an average value of $A_{\rm v}^{{\rm H}\alpha/Spitzer}$ and $A_{\rm v}^{{\rm IR}}$ as a representative value of $A_{\rm v}$ (except for the cB58 and the Clone for which we adopt the $A_{\rm v}^{{\rm IR}}$ value).

We present our final $A_{\rm v}$ estimates as a function of $L({\rm TIR})$ from the 24 $\mu{\rm m}$ indicator in Figure 4.7. Again, the 24 $\mu{\rm m}$ $L({\rm TIR})$ is used here because Abell 2667a and the 8 O'clock arc lack far-IR $L({\rm TIR})$ estimates. Our measurements are compared with the $A_{\rm v}^{\rm IR}$ measurements by Choi et al. (2006), who study the extinctions of objects selected in the near-IR and mid-IR from the *Spitzer* First Look

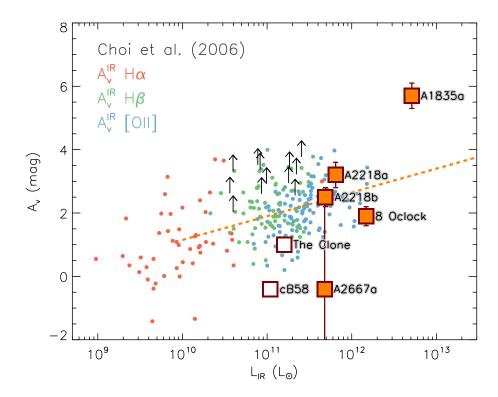


Figure 4.7: Optical extinction, $A_{\rm v}$, from this work compared to the distribution of Choi et al. (2006) from the *Spitzer* First-Look Survey (FLS) with mean redshift of z=0.8. Our points are shown in filled squares, except for the cB58 point (empty square), where we adopt the $A_{\rm v}^{\rm IR}$ value as an extinction estimate (see Section 4.3.4). The Choi et al. (2006) points are $A_{\rm v}^{\rm IR}$ measured by comparing the IR SFR, which is taken as a fiducial value, with the optical SFR measured from the H α , H β , and [OII] emission lines. These are shown in red, blue, and gray circles, respectively. The intrinsic spread of points towards higher extinction of the Choi et al. sample may be larger if the line non-detections (upward arrows), which are likely due to large extinction, could have been measured. The intrinsic spread of extinction at high-z is far wider than previously known from optical-based measurements.

Survey (FLS), which have a mean redshift of z = 0.8 and luminosities ranging from the sub-LIRG to ULIRG range. Their extinction measurements are obtained by comparing the SFR estimates from the H α , H β , and [OII] line fluxes with those from IR luminosities. That is, they estimated the extinction using the ratio of SFR from the individual optical indicators to the IR SFR estimates, e.g. $SFR_{H\alpha}/SFR_{IR}$, $SFR_{H\beta}/SFR_{IR}$, etc. The Choi et al. distribution of extinction values shows a correlation between $A_{\rm v}^{\rm IR}$ and $L({\rm TIR})$ with a formal fit of $A_{\rm v}^{\rm IR}=0.75\times {\rm log}L({\rm TIR})-6.35$, shown as the orange line in Figure 4.7. The scatter is ~ 0.8 mag; however, this value does not include cases where [OII] is undetected (shown as lower limits in Figure 4.7). Allowing for these limits, the scatter is $\gtrsim 1$ mag. This fit and the large scatter are similar to the result of Afonso et al. (2003), who estimate extinction by comparing H α and [OII] SFR estimates to those from the 1.4 GHz radio continuum at a similar mean redshift of z = 0.8. A number of authors (e.g., Bai et al., 2007; Kocevski et al., 2011) find that the variations in extinction are so large that [OII] can be difficult to detect in some galaxies that have high SFRs indicated at $24 \mu m$, although with high quality spectra there are relatively few cases where [OII] is completely absent (Weiner et al., 2007).

We found the spread of our extinction values to be at least as large. Abell 2218a, Abell 2218b, and the 8 O'clock arc lie within the uncertainties of the Choi et al. relationship. Abell 2667a and cB58, with nearly zero mag extinction are less obscured for their $L({\rm TIR})$, whereas the extinction of Abell 1835a is far above the relationship. Selection effects may have reduced the scatter in many previous studies (e.g., the need to have an [OII] line of measurable strength). Our results indicate that galaxies up to $z\sim 3$ show a very large range of $A_{\rm v}$, as is the case in the local Universe.

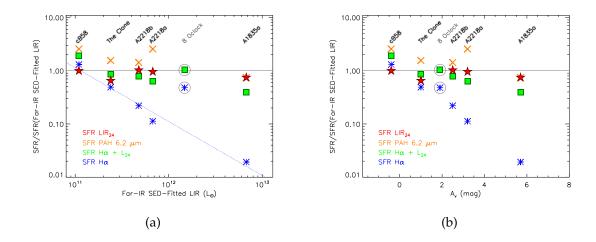


Figure 4.8: Comparison of star formation rate (SFR) estimated from the uncorrected H\$\alpha\$, H\$\alpha\$ + rest-frame \$L(24 \mu m)\$, \$L(TIR)\$ from 24 \$\mu m\$ indicator, and \$L(TIR)\$ from the 6.2 \$\mu m\$ PAH emission line, to the SFR estimated from far-IR SED fitted \$L(TIR)\$, which is taken as a fiducial value, as a function of \$L(TIR)\$ and \$A_v\$: shown in the left and right panels, respectively. The H\$\alpha\$ SFR indicator systematically underestimates \$L(TIR)\$ with increasing discrepancy from the fiducial at larger \$L(TIR)\$, while the rest are consistent to the fiducial within the range of uncertainties. A trend line for the extinction effect on the H\$\alpha\$ SFR indicator in objects with a screen-like extinction scenario (Section 4.4) is shown as the blue dotted line. The points representing the 8 O'clock arc are circled in gray to indicate that \$L(TIR)\$ of the arc is estimated from 24 \$\mu\$m because the SED-fitted \$L(TIR)\$ is not available. The deviation of H\$\alpha\$ SFR of the arc from the trend line in the left panel, however, is not due to the \$L(TIR)\$ measurement, but rather the differences of dust distribution scenarios between the inhomogeneous mixture in the arc and the homogeneous distribution in the rest of the sample (see Section 4.3.4)

4.4 Effects of Extinction on Star Formation Rate Indicators

In Figure 4.8, we compare the SFR estimates from $H\alpha$ (uncorrected for dust extinction), $H\alpha + L(24~\mu\text{m})$, $L(24~\mu\text{m})$, and the 6.2 μm PAH emission with those of L(TIR) measured by far-IR SED fitting as a function of L(TIR) (Figure 4.8 left) and A_{v} (Figure 4.8 right). Abell 2667a is excluded from this comparison due to its lack of the far-IR SED fitted L(TIR) and the fact that the curvature of the lensed arc caused a fraction of $H\alpha$ flux to fall off the slit (the position of the slit is shown in the bottom left panel of Figure 4.1; a part of the 'A2' arc is outside the slit). Without the correction for dust extinction, the $H\alpha$ SFR indicator is clearly affected at high L(TIR) and extinction. For the cases that extinction behavior resembles a uniform dust screen (every galaxy except the 8 O'clock arc), there is a tight trend of the $H\alpha$ SFR deviation from the fiducial SED-fitted SFR as a function of the L(TIR) that is given by

$$\log[SFR(H\alpha)/SFR(LIR)] = 11.21 - 1.01\log(LIR) \tag{4.3}$$

Applying a single overall extinction to H α will increase the estimates of SFRs and improve the agreement to the L(TIR) SFR, but will not correct the trend with L(TIR). Further improvement in H α -based SFRs require introducing corrections for extinction as a function of stellar mass (e.g., Moustakas et al., 2006; Weiner et al., 2007), or of the SFR itself (e.g. Buat et al., 2005); see Section 4.4.

The deviation of the $H\alpha$ point of 8 O'clock arc in Figure 4.8 (left) indicates that a larger amount of $H\alpha$ flux is escaping from the arc given its L(TIR), which could be due to a different dust distribution relative to the star forming regions. The indicator is usually applied with a single nominal level of extinction; in this case, the line in Figure 4.8 (left) would be shifted upward but the slope would not be corrected.

For Abell 2218a, Abell 1835a, and the 8 O'clock arc where Pa α line is welldetected, we apply the extinction correction to the Pa α line luminosity and compare the ratio of $L(24 \mu m)/L(Pa\alpha_{corr})$ with the relationship that Alonso-Herrero et al. (2006) found for local LIRGs. Papovich et al. (2009) made this comparison for Abell 2218a and found the $L(24 \,\mu\text{m})/L(\text{Pa}\alpha_{\text{corr}})$ ratio to be $\simeq 0.5$ dex lower than the local relation, indicating that Abell 2218a has lower $L(24 \mu m)$ than local galaxies of comparable $L(Pa\alpha_{corr})$, while agreeing with those of local individual HII regions. Papovich et al. interpreted this difference as an indication that Abell 2218a harbors extended star-forming regions similar to a scaled-up local HII regions, rather than nuclear starburst like local U/LIRGs. In our analysis, we have reproduced the $L(24 \mu m)/L(Pa\alpha_{corr})$ ratio measured by Papovich et al. using our reduction technique for Abell 2218a, $\log[L(24 \,\mu\text{m})/L(Pa\alpha_{\text{corr}})] = 2.2 \pm 0.2$, and also found that the ratio for Abell 1835a and the 8 O'clock arc are 0.9 - 1.1 dex lower than the Alonso-Herrero et al. (2006) relationship. This is consistent with the result in Table 4.6 that the Rujopakarn et al. (2012) single-band 24 μ m L(TIR)indicator yields L(TIR) values agreeing with the far-IR SED-fitted L(TIR), which implies that these galaxies have extended star formation (see Section 4.3.3 for details of the indicator). That is, the local relationship of $L(Pa\alpha_{corr})$ and $L(24 \mu m)$ reported by Alonso-Herrero et al. (2006) could have limited applicability at high redshift because the Pa α line will systematically have lower extinction for a given $L(24 \mu m)$ due to the extended structure of star formation.

All the other indicators give consistent estimates, within the expected errors of ~ 0.2 dex. We found that the H α + $L(24~\mu\text{m})$ indicator by Kennicutt et al. (2009) tends toward a smaller value of SFR at large extinctions or large L(TIR), particularly above $10^{12}~L_{\odot}$, as observed in Abell 1835a and the 8 O'clock arc. The SFR estimates from the 6.2 μ m PAH emission do not show a systematic trend with

 $L({
m TIR})$, although the scatter is larger than with other indicators. The scatter for individual galaxies is \sim 0.2 dex, similar to the scatter of $L({
m TIR})$ values we have found in Rujopakarn et al. (2012) at redshifts where the 24 $\mu{\rm m}$ band probes the PAH emissions. Since these are high S/N measurements of an individual (i.e., relatively non-blended) PAH emission line, this result suggests that the Rujopakarn et al. (2012) SFR indicator has succeeded in correcting for the SED evolution.

4.5 Chapter Conclusions

We observed four strongly gravitationally lensed star-forming galaxies at 1 < z < 3 with Spitzer/IRS and the LBT/LUCIFER to obtain the mid-IR and near-IR spectroscopy. These observations are targeted to cover IR recombination lines, including $H\alpha$ in the near-IR and $Pa\alpha$ or $Br\alpha$ in the mid-IR. We include another three galaxies from the literature with similar suites of observations, yielding a total sample of seven galaxies. Our sample spans the redshift range of 1.03-2.73 and the L(TIR) range of $1.3 \times 10^{11} L_{\odot}$ to $7.0 \times 10^{12} L_{\odot}$.

The IR recombination line ratios are used to measure extinction that can probe deep into the highly obscured star-forming regions and thus provide an unbiased measure of extinction under the foreground screen assumption. Independently, we estimate the extinction by comparing the optical and IR SFRs, a method that does not make the foreground screen assumption. The results from the two methods are consistent in three out of four galaxies with good IR recombination line flux measurements, suggesting that the dust extinction in these galaxies is consistent with a foreground screen (i.e., uniform dust distribution). However, in the fourth case, the extinction estimates from two methods disagree by 1.8 mag, indicating a deviation from the uniform dust screen assumption, which suggests an inhomogeneous dust mixture. The extinction range of our sample (assuming

a foreground screen) is $\sim 0.0-5.9$ mag, which is a larger spread than previously known for intermediate and high redshift galaxies based on measurements with optical emission lines. These results suggest a large diversity in both the extinction levels and dust distribution scenarios at high redshift.

We compare the performance of various SFR indicators over the extinction range and find that substantial extinction corrections are required for the H α -based SFR indicator. The remaining indicators (1) combined H α and $L(24 \,\mu\text{m})$; (2) $L(24 \,\mu\text{m})$; and (3) PAH (6.2 μ m) all give estimates consistent to within the expected uncertainties of ~ 0.2 dex.

We thank Brian Siana and Eiichi Egami for helpful discussions. WR thanks Alexandra Pope and Philip Choi for data points in Figures 4.6 and 4.7, respectively, and acknowledges the support from the Thai Government Scholarship. This work is supported by contract 1255094 from Caltech/JPL to the University of Arizona.

CHAPTER 5

The Evolution of the Star Formation Rate of Galaxies at $0.0 \leq z \leq 1.2^{1}$

We present the 24 μ m rest-frame luminosity function (LF) of starforming galaxies in the redshift range $0.0 \le z \le 0.6$ constructed from 4,047 spectroscopic redshifts from the AGN and Galaxy Evolution Survey (AGES) of 24 μ m-selected sources in the Boötes field of the NOAO Deep Wide-Field Survey. This sample provides the best available combination of large area (9 square degrees), depth, and statistically complete spectroscopic observations, allowing us to probe the evolution of the 24 μ m LF of galaxies at low and intermediate redshifts while minimizing the effects of cosmic variance. In order to use the observed 24 μ m luminosity as a tracer for star formation, active galactic nuclei (AGN) that could contribute significantly at 24 μ m are identified and excluded from our starforming galaxy sample based on their mid-IR spectral energy distributions or the detection of X-ray emission. Optical emission line diagnostics are considered for AGN identification, but we find that 24 μ m emission from optically-selected AGN is usually from starforming activity and therefore should not be excluded. The evolution of the 24 μ m LF of starforming galaxies for redshifts of $z \le 0.65$ is consistent with a pure luminosity evolution where the characteristic 24 μ m luminosity evolves as $(1+z)^{3.8\pm0.3}$. We extend our evolutionary study to encompass $0.0 \le z \le 1.2$ by combining our data with that of the Far-Infrared Deep Extragalactic Legacy Survey (FIDEL). Over this entire redshift range the evolution of the characteristic 24 μ m luminosity is described by a slightly shallower power law of $(1+z)^{3.4\pm0.2}$.

 $^{^1\}mathrm{Originally}$ appeared as Rujopakarn et al. 2010, The Astrophysical Journal, 718, 1171

We find a local star formation rate density of $(1.09 \pm 0.21) \times 10^{-2}~M_{\odot} {\rm yr}^{-1} {\rm Mpc}^{-3}$, and that it evolves as $(1+z)^{3.5\pm0.2}$ over $0.0 \le z \le 1.2$. These estimates are in good agreement with the rates using optical and UV fluxes corrected for the effects of intrinsic extinction in the observed sources. This agreement confirms that star formation at $z \le 1.2$ is robustly traced by 24 μ m observations and that it largely occurs in obscured regions of galaxies.

5.1 Introduction

We have learned in the past 15 years that the star formation rate (SFR) of the universe peaked at a redshift of $z \geq 1$ and then rapidly declined by an order of magnitude to the present day (e.g., Lilly et al., 1996; Madau et al., 1996; Chary & Elbaz, 2001; Hopkins, 2004; Le Floc'h et al., 2005; Pérez-González et al., 2005; Hopkins & Beacom, 2006) . The exact cause of the decline of the SFR remains unknown. However, since the period from $z \sim 0.6$ to the present encompasses nearly half of cosmic time coinciding with the SFR decline, this redshift range is a key regime for constraining the mechanisms that may be responsible.

The evolution of the SFR has been measured extensively at mid-IR (MIR; 8–30 μ m), far-IR (FIR), ultraviolet (UV), and optical wavelengths. Among these wavelengths, MIR and UV are ideal tracers for dust-obscured and unobscured galaxies, respectively. The MIR emission of galaxies originates from the reprocessed UV radiation of dust-embedded, highly obscured starforming regions, and hence is sensitive to radiation from star formation that can not be seen directly at optical wavelengths (e.g., Kennicutt, 1998; Buat et al., 1999). The stellar UV radiation field is largely created by hot OB stars ($M_* > 10~M_\odot$), which have very short lifetimes ($< 20~{\rm Myr}$) and hence trace current star formation. The dust obscuration is generally substantial for star formation in galaxies at and above the characteristic

luminosity L* (Schmitt et al., 2006; Buat et al., 2007). Such galaxies comprise the majority of galaxies studied beyond the low redshift volume, so the MIR offers a relatively complete probe of SFR at intermediate and high redshifts. Among the IR wavelengths, the 24 μ m-band is particularly suitable to study SFR evolution because it avoids most of the strong emission features from the stochastically heated aromatic hydrocarbons (hereafter PAH) at wavelengths $3.3 < \lambda < 13~\mu m$ for redshifts $z \lesssim 0.5$ while still avoiding the contamination from the Galactic IR cirrus at longer wavelengths (Shupe et al., 1998).

Measurements of IR number counts and luminosity functions (LF) of galaxies demonstrate the rapid evolution of the SFR. Early IR studies utilized the IRAS Bright Galaxy Sample (Soifer et al., 1989) and the IRAS calibration field (Hacking & Houck, 1987) and focused on accounting for the cosmic infrared background (CIB; Elbaz et al., 1999) with discreet MIR sources (Hacking et al., 1987; Saunders et al., 1990; Soifer & Neugebauer, 1991). Studies of galaxy number counts with ISO and Spitzer have shown that IR galaxies evolve very strongly (Elbaz et al., 1999; Franceschini et al., 2001; Dole et al., 2004; Marleau et al., 2004; Papovich et al., 2004). As redshifts of IR samples became available, the LF could be constructed in the nearby volume (Rieke & Lebofsky, 1986; Saunders et al., 1990; Yahil et al., 1991; Rowan-Robinson et al., 1997; Shupe et al., 1998) and subsequently extended to intermediate and high redshifts (z > 3) with large samples of photometric redshifts (Pozzi et al., 2004; Le Floc'h et al., 2005; Pérez-González et al., 2005; Caputi et al., 2007; Marleau et al., 2007) to study the SFR evolution over cosmic time. However, most of these studies were either in the local regime (z < 0.1) or at intermediate to high redshifts (z > 0.5). The redshift range 0.1 < z < 0.6includes more than 4 Gyr of galaxy evolution and needs to be characterized in detail to understand this process.

Observations of galaxy evolution at low and intermediate redshifts face two challenges. First, a large area, deep survey is required to access a large volume at lower redshifts, which is critical to minimize cosmic variance. For example, a deep survey at redshift $z\sim0.5$ would need five times the solid angle coverage of one at $z\sim 1$ to probe a comparable comoving volume. Second, while photoz's are generally adequate for distance determination at high redshift, accurate spectroscopic redshifts are critical at low and intermediate redshifts. To illustrate this issue, consider typical photometric redshift uncertainties of $\Delta z/(1+z) =$ 0.05. The corresponding fractional uncertainty in z would be a tolerable 10% at $z\sim 1$, while at $z\sim 0.25$ and below, the fractional uncertainty would exceed 25%. Also, photometric redshifts are only accurate for galaxies whose SEDs are well matched by either SED templates or, in the case of empirical photometric redshifts, galaxies in a spectroscopic training set. This may not be the case for heavily obscured galaxies such as luminous IR galaxies (LIRGs). In addition, the accuracy of some photometric redshift samples in the literature has not been verified with spectroscopy, and unknown systematic errors may be present.

In this work we construct the rest-frame 24 μ m LFs of starforming galaxies, measure their evolution, and estimate the SFR for $0.0 \le z \le 0.6$ from the LF. In addition to constraining the LF and SFR evolution accurately at low and intermediate redshifts, we combine our results with those from the Far-IR Deep Extragalactic Legacy Survey (FIDEL, Magnelli et al., 2009) to extend the constraints to $z \sim 1.2$. We organize this paper as follows. In § 5.2 we discuss our *Spitzer* 24 μ m sample, the spectroscopic redshifts from AGES, the optical catalog from NDWFS, and address their completeness. In § 5.3 we describe the construction of the LF, starting with the derivations of galaxy luminosities (§ 5.3.1), identification and exclusion of AGN from starforming galaxies (§ 5.3.2), estimators for the LF (§ 5.3.3),

parameterization of the evolution of the LF with redshift (§ 5.3.5), and the estimation of the SFR from the LF (§ 5.3.6). We then present the results in § 5.4 for the local LF (§ 5.4.1), the LF evolution at low and intermediate redshifts (§ 5.4.2), the LF evolution constraint out to $z \sim 1.2$ (§ 5.4.3), as well as the star formation rate evolution of starforming galaxies (§ 5.4.4). We summarize our results in § 5.5. We assume a Λ CDM cosmology with $\Omega_m = 0.3$, $\Omega_{\Lambda} = 0.7$, and $H_0 = 70$ km s⁻¹Mpc⁻¹ throughout this paper.

5.2 The Data

We construct the 24 μ m LF of galaxies in the 9 sq. degree Boötes field of the NOAO Deep Wide-Field Survey (NDWFS Data Release 3; $\alpha = 14^h 32^m$, $\delta = +34^\circ 16'$, J2000.0; Jannuzi & Dey, 1999). The Boötes field has optical imaging reaching the 5- σ flux limit of 26.6, 26.0, 26.0, and 21.4 in B_W , R, I, and K (Vega magnitudes), respectively. Details about the NDWFS can be found in Jannuzi & Dey (1999) and at the survey's website¹.

In addition to the deep optical imaging, the Boötes field has extensive panchromatic coverage from other surveys, including an X-ray survey with the *Chandra* Space Telescope (XBoötes; Murray et al., 2005) comprising of 5 ks ACIS-I exposures, near-UV deep 30 ks imaging from *GALEX* (Martin et al., 2003), the IRAC Shallow Survey in the 3.6, 4.5, 5.8, and 8.0 μ m bands reaching magnitudes of 19.1, 18.3, 15.9, and 15.2 mag (Vega mag), respectively, (Eisenhardt et al., 2004), the deeper *Spitzer* Deep, Wide-Field Survey (SDWFS, Ashby et al., 2009), and MIPS MIR photometry at 24 μ m down to 0.27 mJy (Papovich et al., 2004; Houck et al., 2005). These imaging data are complemented by the set of optical spectroscopic redshifts from the AGN and Galaxy Evolution Survey (AGES; Kochanek et al.,

¹http://www.noao.edu/noao/noaodeep

in prep.), which is a statistically complete redshift survey of the field at low and intermediate redshifts ($0 \le z \le 0.8$) (Kochanek et al., in prep.).

5.2.1 Spitzer 24 μ m-Observations, Reduction, and the Final Catalogue

The 24 μ m photometry in the Boötes field was obtained by the *Spitzer Space Telescope* wide-area survey with the Multiband Imaging Photometer for *Spitzer* (MIPS; Rieke et al., 2004) and processed with the MIPS GTO Data Analysis Tool (DAT; Gordon et al., 2005). The mean exposure time per pixel across the Boötes field is 87 seconds. The pixel size of the final mosaic is 1"25 with a FWHM of 5".7.

Source extraction from the final 24 μ m mosaic was done using the techniques described in Papovich et al. (2004). Briefly, we weight the image by the typical integration time of each region to obtain uniform noise across the mosaicked image. We filtered the image with a Gaussian kernel similar to our 24 μ m PSF to remove artifacts and optimize point-source detection and then used DAOPHOT (Stetson, 1987) to detect sources. The actual photometric measurement was carried out by fitting empirical point spread functions (PSF) constructed from bright sources in the image. Based on Monte Carlo simulations by Papovich et al. (2004) the 80% completeness flux threshold is $F_{\nu}(24~\mu\text{m}) = 0.27~\text{mJy}$, and there are 8,572 objects in our sample above this flux level.

The MIPS survey of the Boötes field combines considerable depth with a large contiguous area of 32,457 arcmin² (9.0 deg²). While many other fields have been surveyed to deeper $F_{\nu}(24~\mu\text{m})$, such as the GOODS, ELAIS and CDF-S fields (Pozzi et al., 2004; Le Floc'h et al., 2005; Chary, 2006; Elbaz et al., 2007) with 80% completeness flux of 25 μ Jy, 61 μ Jy and 83 μ Jy, respectively, they also cover significantly smaller area (0.011 deg², 0.036 deg², and 0.407 deg², respectively), and therefore encompass significantly smaller volumes at low and intermediate redshifts. The Cosmic Evolution Survey (COSMOS, Scoville et al., 2007) has a large

sample of spectroscopic redshifts (Lilly et al., 2007) and deep, $\sim 80~\mu Jy$, 24 μm imaging (LeFloc'h et al., 2009). The 2 deg² area of the COSMOS field is one of the best combinations of large area and depth at higher redshifts; however, a larger angular coverage is still required to suppress the effects of cosmic variances at low and intermediate redshifts. The available large-area MIR surveys, such as the *Spitzer* Wide-area Infrared Extragalactic Survey (SWIRE) and the European Large Area *ISO* Survey (ELAIS, 15 μm), currently lack thorough spectroscopic redshifts.

5.2.2 Optical Spectroscopy Target Selection, Observation, and the Final Catalogue

The Boötes field was observed spectroscopically by the AGES during 2004-2006 using the Hectospec spectrograph in a survey region of 7.9 deg² (Kochanek et al., in prep). Hectospec is a fiber-fed spectrograph with 300 robotically assigned fibers covering a 1-degree diameter field of view at the f/5 focus of the 6.5-meter MMT Observatory (Fabricant et al., 2005). AGES produced ~20,000 redshifts, of which ~16,500 and ~3,500 are galaxies and quasars, respectively, with redshift uncertainties less than $\sigma_z \sim 100 \ {\rm km \ s^{-1}}$ (as in the similar survey by Papovich et al. (2006)) and a median galaxy redshift of z=0.26 (Kochanek et al., in prep.).

Targets for spectroscopy were principally selected on the basis of their optical magnitudes. AGES targeted galaxies to $I_C < 20$, where I_C is the Kron-like magnitude (in Vega units) in the Kron-Cousins I-band of the NDWFS (SExtractor's MAG_AUTO; Bertin & Arnouts, 1996). For galaxies brighter than $I_C = 18.5$, there was full sampling. For fainter galaxies with $18.5 < I_C < 20$, AGES used random sparse sampling of 1 in 5 galaxies, with rates that depended on a variety of other factors, so as to put emphasis on more unusual objects. Additional targets were added to the spectroscopic sample if they were brighter than certain flux limits

in the X-ray, infrared, other optical bands, and radio. For example, all galaxies with $F_{\nu}(24 \ \mu \text{m})$ above 0.5 mJy were targeted, as well as 30% of those down to 0.3 mJy. For each object, the a priori sampling rate is known and so the object can be exactly weighted to form an unbiased sample of $I_C < 20$ galaxies. AGES observed the Boötes field with 15 complete tilings, so the completeness for the target galaxies is very high. Our final sample has 4.3% incompleteness due to difficulties in assigning fibers to targets and 2.1% incompleteness due to failing to get a successful redshift from an assigned fiber. We also estimate that the parent photometry catalog is missing 4% of the objects in the range $15 < I_C < 20$, half of which is due to interference by nearby bright stars, the rest likely due to blending and corruption of the parent photometry. We model these mild incompletenesses, including factors for areal target density and surface brightness, and correct the final weights of objects in the redshift catalog (Eisenstein et al., in prep.). As the total incompleteness correction is only 10%, it is very likely that the systematic error in the correction is far less than the Poisson and cosmic variance in our results.

Each Hectospec fiber is 1"5 in diameter and produces a spectrum covering the wavelength range of 3500 Å $\leq \lambda \leq$ 9200 Å with 6 Å FWHM resolution (R \sim 1,000). Typical signal-to-noise ratios of the AGES spectra are 2-14 per pixel with a median of 5 per pixel. We fit redshifts to AGES with two automated pipelines, one based on the SDSS template-fitting code, the other on cross-correlations. The pipelines make use of spectral features across the spectral range (absorption lines, emission lines, and spectral breaks due to metal-line absorptions) and hence result in accurate redshifts regardless of whether a particular spectral line is compromised (e.g. by overlap with sky lines). The two pipelines gave broadly consistent results. In addition, we visually examined every fit. Any objects with

visually questionable results were tagged for reobservation, since AGES covered the full field in six sequential passes. The result is a spectroscopic catalog with high completeness and high reliability. The spectroscopic success rate, after fiber assignment, is 98%, and we expect the redshift error rate on claimed successes to be well below 1%. Any systematic biases due to errors in the completeness corrections or the redshift catalog are likely to be considerably smaller than the statistical errors of our luminosity function.

In the redshift range of interest, $0.05 \le z \le 0.65$, we have redshifts for 4,047 objects with $F_{\nu}(24 \,\mu\text{m})$ above the 80% completeness limit of 0.27 mJy.

5.3 Infrared Luminosity Function

Here we describe the construction of the 24 μ m LF. We start by estimating the 24 μ m and optical (I-band) rest-frame luminosities, then identify and exclude AGN in our sample, and finally construct the LF using the classical $1/V_{max}$ (Schmidt, 1968; Huchra & Sargent, 1973) and the maximum likelihood estimator (MLE; e.g., Sandage et al., 1979; Marshall et al., 1983; Yahil et al., 1991). Later in this section, we describe the parameterization of LF evolution, which will be used to study the evolution of the SFR.

5.3.1 24 μ m and I-band Luminosity Estimation

In addition to the obvious need for 24 μ m luminosities, $L(24 \, \mu\text{m})$, to construct the LF, we have to compute the I-band luminosity for each galaxy. AGES spectroscopy was targeted based on an I-band, flux-limited parent catalog. Hence, an object can only be included in the final LF sample if it is detected above the flux limits at both 24 μ m and I-band. Therefore, the luminosities in both bands are needed for estimating the maximum redshift, z_{max} , that an object would still be detected in both bands to the construct the $1/V_{max}$ LF. $L(24 \, \mu\text{m})$ is estimated by

the formalism given by Rieke et al. (2009). For the I-band, we derive the I-band k-correction using the kcorrect code (Blanton & Roweis, 2007) and then use the k-correction to estimate the I-band luminosity.

The I-band k-corrections were derived using optical photometry from ND-WFS and redshifts from AGES. A fraction of our I-band objects are affected by scattered light from bright stars. Specifically, some of the NDWFS I-band Kronlike magnitudes (SExtractor's MAG_AUTO), I_C , are overly bright due to contamination from low-surface-brightness halos of nearby bright stars. This problem can be corrected by synthesizing a new I-band magnitude, I_R , by adding a Kron-like magnitude in R-band, R_C , to the I-R color from 6" apertures ($I_R=R_C+I_{6''}-I_{6''}$ $R_{6''}$). This synthesized I_R is less sensitive to the I-band halo than I_C . Then we compare I_R to I_C to compute a new I-band magnitude, I_{total} , that uses the fainter magnitude if the two differ significantly; otherwise we average them (Eisenstein et al., in prep.). The I_{total} computation is done in a way that the continuity of the magnitudes is preserved. In the cases that require averaging I_R and I_C , the differences are on the order of a tenth of a magnitude and hence averaging a logarithm does not introduce a significant bias. We note that the aperture correction is insensitive to the choice of estimation procedure and that the final LFs are little affected by this correction, ultimately because the I-band generally has deeper photometry than at 24 μ m and hence most of the values of z_{max} will be limited by the 24 μ m photometry. Apart from the I_{total} for I-band photometry, we use the 4"-diameter aperture magnitude from NDWFS for the B_W and R bands to perform k-correction estimation. We adopt the following corrections to convert the Vega zero points to AB: +0.02 mag, +0.19 mag, and +0.44 mag in B_W , R, and I, respectively. The Galactic extinction for our field is $A_I = 0.02$ mag (Schlegel et al., 1998).

The estimation of $L(24~\mu\text{m})$ requires an assumption for the spectral energy distribution (SED) of a galaxy in the IR regime, which has been modeled by many authors (e.g., Dale et al., 2001; Chary & Elbaz, 2001; Dale & Helou, 2002; Lagache et al., 2003, 2004; Smith et al., 2007; Dale et al., 2007). More recently, Rieke et al. (2009) constructed a library of SEDs by combining stellar photospheric spectra from $0.4-5~\mu\text{m}$ with Spitzer IRS spectra from $5-30~\mu\text{m}$ and a modified blackbody spectrum at longer wavelengths for 11 representative local Luminous IR galaxies (LIRGs; $10^{11}L_{\odot} < L(\text{TIR}) < 10^{12}L_{\odot}$) and ultraluminous IR galaxies (ULIRGs; $L(\text{TIR}) > 10^{12}L_{\odot}$). Higher L(TIR) galaxies contain more intense starforming activity and hence a larger fraction of warm dust, leading to changes in the SED with IR luminosity.

Normally, the derivation of SFR from MIR photometry involves selecting the SED that best matches the object's luminosity given its MIR flux and redshift, integrating this SED to obtain $L({\rm TIR})$, and then using a SFR metric to calculate the SFR. However, this procedure implies fitting a SED with only one data point, 24 $\mu{\rm m}$ in our case, because the number of objects that are detected in multiple MIPS bands is very limited, which could lead to significant uncertainties. Rieke et al. (2009) circumvented this problem by first assigning a SFR to each SED, which has a unique $L({\rm TIR})$. They then derive a flux in the relevant band pass (24 $\mu{\rm m}$) over a range of redshifts.

Given that $L(\text{TIR})/L(24~\mu\text{m}) \sim 10$ (e.g., Rieke et al., 2009), our sample with galaxies mainly in the 24 μm luminosity range $10^{8.5} < L(24~\mu\text{m}) < 10^{10.5}$ (Fig. 5.1, left panel), is dominated by normal starforming galaxies ($L(\text{TIR}) < 10^{11} L_{\odot}$). LIRGs only start contributing significantly to the MIR luminosity density at redshifts greater than z=0.2. Although ULIRGs start to appear in our sample at $z\sim0.4$, we will demonstrate in § 5.3.2 that they are mostly AGN and we will

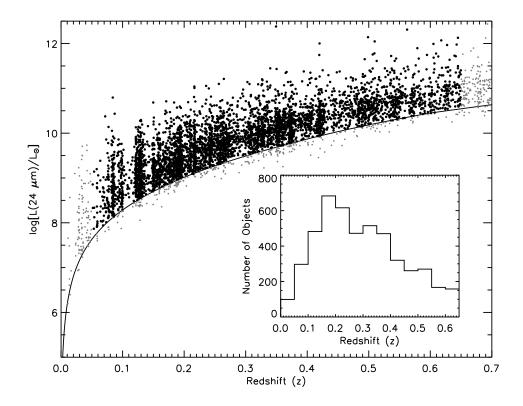


Figure 5.1: Redshift distribution of the rest-frame 24 μ m luminosity for our sample. The grey dots show all 24 μ m galaxies with spectroscopic redshifts from AGES. The black dots are those above the 24 μ m completeness flux limit (0.27 mJy) at $0.05 \le z \le 0.65$ that we use to construct the LF. The line indicates the $L(24~\mu\text{m})$ corresponding to this completeness flux threshold as a function of redshift. *Inset*: The redshift distribution of the AGES objects detected at 24 μ m.

exclude them from our sample of starforming galaxies.

5.3.2 Separating Starforming Galaxies and AGN Hosts

To quantify the 24 μ m emission due to star formation, we need to minimize the contribution of AGN. There are several methods to identify AGN in a galaxy sample. Optical emission line diagnostics such as the BPT method (Baldwin et al., 1981) are commonly used when optical spectra are available. MIR power-law characteristics of AGN (e.g., Alonso-Herrero et al., 2006; Donley et al., 2007) and

MIR color criteria (e.g., Lacy et al., 2004; Stern et al., 2005) can be used if multi-band MIR photometry is available. X-ray emission is also a direct indicator of AGN activity. Since the Boötes field has multiwavelength coverage that permits using all these, we investigate all of them in this section.

5.3.2.1 Optical Emission Line AGN Diagnostics

In addition to identifying the broad-line AGN (type 1), our spectroscopic survey allows us to identify narrow-line AGN (type 2) in the sample using the BPT diagram. We require that all four relevant lines (H α , H β , [OIII], and [NII]) are detected at S/N > 3. Thus, the BPT method can only be used for redshift of z < 0.35 because at higher redshifts the H α emission line shifts beyond the red limit of the spectral range covered by Hectospec. We identify AGN on the BPT diagram (Fig. 5.2) as objects with line ratios above the theoretical limit (hereafter the Kewley line; Kewley et al., 2001, 2006) of ratios that starforming regions could produce. The Kewley line was estimated by considering all possible combinations of starforming galaxy spectra based on the Starburst99 (Leitherer et al., 1999) models. Objects above the Kewley line will be referred to hereafter as optically selected AGN. We identified 421 optically selected AGN at $0.0 \le z \le 0.35$, 46% of which (192/421) have $F_{\nu}(24 \, \mu \text{m}) > 0.27 \, \text{mJy}$.

However, we need to determine whether the 24 μ m emission from optically selected AGN is actually dominated by the AGN. Our 1"5 diameter spectroscopic fiber would cover a distance of 6 kpc at the median redshift of the AGES sample (z=0.26) and the fiber would be placed at the center of the target galaxy. Thus our BPT classification would be sensitive to the nuclear flux from the AGN but could miss the emission lines contributions from starforming regions outside the fiber. In the case that star formation dominates the global optical emission but an AGN dominates the emission within the fiber, the global 24 μ m flux could in

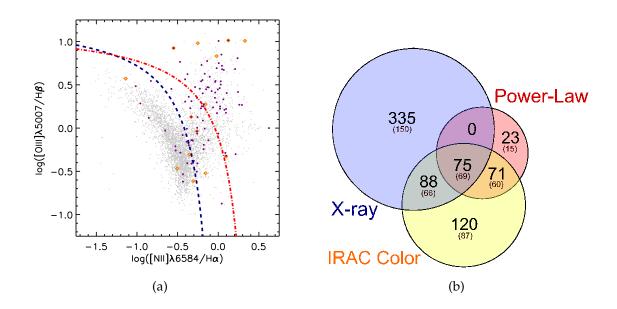


Figure 5.2: (a) Optical selection of AGN using the BPT diagram. Orange diamonds and magenta dots are power-law and X-ray selected AGN, respectively. The Kewley and Kauffmann lines are shown by red dot-dashed line and blue dashed line, respectively (Kewley et al., 2001; Kauffmann et al., 2003). Many power-law and X-ray selected AGN are identified as starforming galaxies by the BPT diagram. Note that a large fraction of power-law and X-ray selected AGN are not shown here because they do not have sufficiently strong emission lines to apply the BPT diagnostic and most of them are at z > 0.35 where H α line redshifts out of the Hectospec spectrum. (b) The Venn diagram for 712 AGNs at $0.0 \le z \le 0.65$ to illustrate the overlapping of AGN identified by X-ray detections, power-law fitting, and the (Stern et al., 2005) color criteria. The numbers in each area and the numbers in parentheses are the total numbers of objects and the numbers of objects detected at 24 μ m, respectively. 288 of 712 AGNs in this Venn diagram are detected at 24 μ m, pass all quality cuts, and are in the main galaxy sample. They are excluded from the sample to obtain the starforming galaxy sample that can be accurately used as a tracer of star formation.

fact be dominated by the emission from starforming activity and excluding such objects would lead to an underestimation of the star formation rate.

We therefore investigate the origin of mid-IR emissions from the optically selected AGN by studying the IRAC colors of these AGN. Using IRAC photometry from the IRAC Shallow Survey (6" aperture, \S 5.2), we study the [3.6 μ m] - [4.5 μ m] versus [5.8 μ m] – [8.0 μ m] color-color diagram (hereafter, [3.6]–[4.5] and [5.8] – [8.0], respectively) for optically selected AGN (Fig. 5.3, *left*). The color-color diagram can be used to identify MIR aromatic emission characteristic of star formation activity (Smith et al., 2007; Shi et al., 2007), because the strongest aromatic features at 6.2, 7.7, and 8.6 μ m fall into the 8.0 μ m band (channel 4; \simeq 6.2 - 10 μ m) at redshifts $0.0 \le z \le 0.5$. This behavior results in a redder [5.8]–[8.0] color for objects with MIR aromatic emission, which also implies that the MIR emission of these objects is dominated by star formation. The empirical color boundary that separates the aromatic and non-aromatic region is $[5.8]-[8.0] \simeq 1$ (Brand et al., 2009). We found optically selected AGN distributed across the full range of [5.8]–[8.0] color. However, if we further separate optically selected AGN into those detected at 24 μ m and those that are not, they split into two locales. Optically selected AGN without 24 μ m detection are relatively blue in [5.8]–[8.0] color while more than 70% of those with 24 μ m detection congregate in the aromatic locus. The bluer MIR locus of optically selected AGN without 24 μ m detection is consistent with the Rayleigh-Jeans tail of an old stellar population's photospheric emission that peaks at 1.6 μ m. This suggests the source of 24 μ m emission in an optically selected AGN is likely to be starforming activity, not the AGN.

5.3.2.2 X-ray Detections

We have also searched for AGN detected in the 5 ks X-ray survey of the Boötes field (XBoötes; Murray et al., 2005). We define an X-ray selected AGN as any source

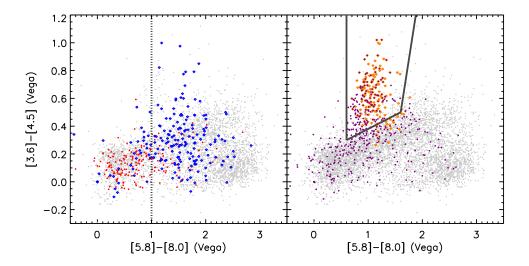


Figure 5.3: Mid-IR properties of AGNs in our sample *Left*: The [3.6]–[4.5] vs. [5.8]–[8.0] color-color diagram separates objects with and without aromatic emissions at an empirical boundary of [5.8]–[8.0] ~ 1 (*vertical line*, Brand et al., 2009), with aromatic-emitting objects on the redder [5.8]–[8.0] side. Blue and red dots represent optically selected AGN with and without 24 μ m detection, respectively. *Right*: the same diagram showing the Stern et al. (2005) AGN selection criteria (*trapezoidal box*), power-law selected AGN (*orange diamonds*), and X-ray selected AGN (*magenta dots*). A majority of optically selected AGN that emit strongly at 24 μ m are aromatic-emitting objects and their MIR emission is likely dominated by starforming activity. On the other hand, a majority of X-ray selected AGN share the same locus as power-law selected AGN, indicating that their AGN component could contribute significantly at 24 μ m.

with two or more X-ray counts and a > 25% probability based on the Bayesian matching method described by Brand et al. (2006). Since XBoötes is designed to have a large contiguous area and a shallow flux limit, X-ray identification based on the survey will only identify the strongest AGN. The X-ray luminosities of these sources are typically brighter than $10^{42}\,\mathrm{erg}\,s^{-1}$ (Hickox et al., 2009) and hence they are unlikely to be dominated by starforming activity. Although it is not possible to infer directly the AGN contribution to the 24 μ m flux from the strength of the X-ray emission, strong AGN are known to emit significantly in the MIR (e.g., Barmby et al., 2006). We found 498 X-ray selected AGN at $0.0 \le z \le 0.65$ and 175 of them are at the redshift range where we construct the LF (0.05 < z < 0.65), are in the main galaxy sample, and are detected at 24 μ m.

5.3.2.3 MIR AGN Diagnostics

AGN with significant MIR emission can be identified most directly by applying MIR selection methods. MIR photometry can be used to identify luminous AGN due to their characteristic power-law SED rising from the optical wavelengths to the IR. This power-law SED is due to the combination of thermal emission of warm and hot dust components and non-thermal emission of the nuclear region (Neugebauer et al., 1979; Elvis et al., 1994; Rieke & Lebofsky, 1981). AGN can be identified by fitting a power law, $F_{\nu} = \nu^{\alpha}$, to all four bands of IRAC photometry covering 3.6 - 8 μ m (Eisenhardt et al., 2004) with χ^2 minimization. We require an object to be detected in all four bands at above 5- σ for power-law fitting. *Power-law selected AGN* are defined as galaxies exhibiting power-laws with α ranging from -0.5 to -2.0 (Ivezić et al., 2002; Alonso-Herrero et al., 2006; Donley et al., 2007). The power-law method identified 169 AGN. Among these AGN, 144 are detected at 24 μ m (85%), which is the highest fraction among the AGN classification methods. This suggests that the 24 μ m emission of power-law selected

AGN is an extension of their power-law AGN SED to longer wavelengths rather than from the warm dust characteristic of starforming galaxies. Therefore the power-law selection of AGN provides a good basis to exclude AGN from our 24 μ m starforming galaxy sample. However, the signal-to-noise requirement on the IRAC photometry for power-law fitting affects the completeness of power-law AGN selection. Among these 169 AGN, 73 are at 0.05 < z < 0.65 and pass all targeting and quality cuts, and are detected at 24 μ m.

Another manifestation of power-law SED of AGN is their locus on MIR colorcolor diagrams (\S 5.3.2). Again, we consider the [3.6]–[4.5] vs. [5.8]–[8.0] colorcolor diagram. AGN (mostly type 1) exhibit power-law SEDs and this results in a distinct locus that is significantly redder in the [3.6]–[4.5] color than both early type and starforming galaxies (see Fig. 1 of Stern et al., 2005). The locus of early type galaxies, which also exhibit power-law SEDs but with $\alpha > -0.5$, would lie blueward in both color indices (lower-left locus on the diagram) because, as mentioned earlier, their SEDs in the NIR are dominated by the Rayleigh-Jeans tail of old stellar populations. Stern et al. (2005) empirically define the AGN locus on the color-color diagram (the "Stern wedge", Fig. 5.3, right). AGN selected based on this color-color criteria (hereafter IRAC color selected AGN) are defined by galaxies with ([5.8] - [8.0]) > 0.6 and ([3.6] - [4.5]) > 0.2([5.8] - [8.0]) + 0.18 and ([3.6]-[4.5]) > 2.5([5.8]-[8.0])-3.5. We found 354 IRAC color selected AGN in the redshift range $0.0 \le z \le 0.65$, 80% (282/354) of which have 24 μ m detections. A majority (86%, 146/169) of the power-law selected AGN are also selected by the Stern et al. (2005) criteria. The reverse is not the case: only 41% (146/354) of IRAC color selected AGN exhibit identifiable power-law characteristics. However, Fig. 5.3 (right) illustrates that there are a few galaxies in the power-law selected AGN locus but not identified as AGN by the MIR power-law fitting. These galaxies

satisfy the Stern et al. (2005) criteria, which suggests that adopting the Stern et al. (2005) AGN selection criteria helps augment the completeness of power-law AGN selection in our case. Among these 354 IRAC color selected AGN, 159 are at 0.05 < z < 0.65 and pass all targeting and quality cuts, and are detected at 24 μ m.

As another test for MIR-emitting AGN, we used the behavior of the IRAC [5.8] - [3.6] color. For $z \ge 0.2$, both bands should be on the Rayleigh-Jeans tail of the photospheric SED without substantial contamination by infrared excess emission from normal star formation (see, e.g., the Rieke et al. (2009) SED templates). However, the warm dust around an AGN should appear as an anomalously red color. Many of the objects identified in this way are still dominated by aromatic emission, as judged by their full set of IRAC colors. However, a small fraction (21 objects at 0.05 < z < 0.65) may have IR excesses associated with AGN that are not identified by other methods. These 21 objects amount to only 7% of our AGN sub-sample. Without other independent AGN signatures we cannot determine whether the 24 micron emission of these galaxies is dominated by AGN. Our results are independent, within the errors, of whether we include or exclude these sources from our starforming galaxy sample.

5.3.2.4 Summary of Multiwavelength AGN Selection

We found that optical line diagnostics (the BPT diagram) select AGN that frequently have 24 μ m fluxes dominated by emission from star formation (§ 5.3.2) and therefore that these diagnostics should not be used as a basis to exclude AGN from the MIR starforming galaxy sample. Methods based on power-law characteristic of AGN (power-law SED selection (Donley et al., 2008) and color criteria, e.g. Stern et al. (2005)) yield AGN samples more relevant to our 24 μ m study (§ 5.3.2). On the [3.6]–[4.5] vs. [5.8]–[8.0] color-color diagram, X-ray selected

AGN occupy regions encompassing the locus of power-law selected AGN and extend toward the bluer [5.8]–[8.0] and [3.6]–[4.5] color regions (Cardamone et al., 2008; Gorjian et al., 2008), indicative of older stellar populations, suggesting that X-ray selection helps augment the completeness of AGN selection by the MIR selection methods. Therefore we combine MIR selection of AGN with X-ray selection to create a list of AGN to be excluded from our 24 μ m LF study.

The Venn diagram (Fig. 5.2) illustrate the significant overlapping of AGN selected by X-ray, Power-law fitting, and the Stern et al. (2005) criteria. At $0.0 \le z \le 0.65$, we find a total of 712 AGNs, 288 of which are detected at 24 μ m, pass all targeting and quality cuts, and are in the redshift range $0.05 \le z \le 0.65$ where we use to construct LFs. Fig. 5.4 illustrates the fraction of AGN as a function of 24 μ m luminosity and redshift. Note that objects with $L(24 \ \mu\text{m}) > 10^{11} \ L_{\odot}$ are mostly AGN. Most of the trend in the AGN fraction with redshift seen in Fig. 5.4) is a consequence of the increasing fraction of AGN at higher $L(24 \ \mu\text{m})$. Higher redshift bins are dominated by higher luminosity galaxies because of the survey flux limit and hence will show higher AGN fractions.

Excluding these 288 AGNs from the 4,047 galaxies at $0.05 \le z \le 0.65$ that are detected at 24 μ m, we obtain a sub-sample of 3,759 starforming galaxies to construct the LFs.

5.3.3 Methodology

We estimate our LF at redshift $0.05 \le z \le 0.65$ using the $1/V_{max}$ formalism (Schmidt, 1968; Huchra & Sargent, 1973), and the local 24 μ m LF (hereafter *local LF* or *LLF*) using the parametric maximum likelihood estimator (MLE; e.g., Sandage et al., 1979; Yahil et al., 1991; Marshall et al., 1983). The local LF is then evolved to fit the higher redshift $1/V_{max}$ LFs using a χ^2 minimization to determine the evolution of the LF as a function of redshift (§ 5.3.5).

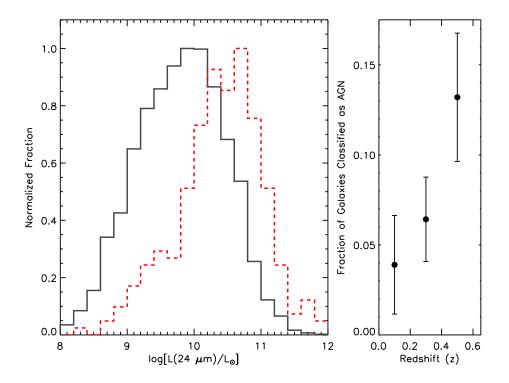


Figure 5.4: The 24 μ m Luminosity distribution of the starforming and AGN subsamples at $0.05 \le z \le 0.65$. Left: The rest-frame $L(24~\mu\text{m})$ distribution of 3,759 starforming galaxies (solid histogram) and 288 AGNs (dashed histogram) identified by their characteristic power-law SED (based on power-law fitting and IRAC colors) and X-ray detections that pass all targeting and quality cuts. Right: The fraction of galaxies identified as AGN in our sample rises with redshift at $z \le 0.6$. This is partly due to the fact that AGN are intrinsically more luminous, as shown in the left panel. ULIRGs (galaxies with $L(IR) > 10^{12}~L_{\odot}$ or $L(24~\mu\text{m}) > 1.5 \times 10^{11}~L_{\odot}$) are dominated by galaxies exhibiting AGN activity that are excluded from our LFs of starforming galaxies.

The $1/V_{max}$ estimator is non-parametric in the sense that it does not assume a functional form for the LF. However, it is sensitive to density variations due to large scale structures. The large areal coverage of the NDWFS helps to mitigate this problem. But at the lowest redshifts that we observed, even a 9 sq. deg field covers a sufficiently small volume to show significant cosmic variance. The most prominent example is a \sim 50% overdensity near $z \simeq 0.15$ (see Fig. 5.1).

We construct the $1/V_{max}$ LF by first computing a spectroscopic selection function that takes into account the parent catalog's incompleteness due to imaging and targeting issues. These issues include sparse sampling due to priority conflicts in Hectospec fiber assignment, incompleteness due to fiber allocation limits (such as the proximity limit), and redshift extraction failure (§ 5.2.2). The selection function is then applied to each galaxy as a weight, w_i , that corrects for incompleteness. The V_{max} in our analysis is taken to be the volume enclosed by the maximum redshift that allows an object to be included in both our I-band (spectroscopic targeting) and 24 μ m samples. That is, we take the smaller of the redshift at which $F_{\nu}(24 \,\mu\text{m})$ would drop below 0.27 mJy or the redshift at which the object will have $I_C > 20$ mag. We estimate the $1/V_{max}$ LF in four independent redshift bins ranging from redshift z = 0.05 to z = 0.65 with a bin width of 0.15. The lowest redshift region (e.g. z < 0.05) was excluded to avoid potentially unrealistic number densities due to the very small volume and number of galaxies and also to minimize the effect of photometric bias due to nearby, large galaxies that extend beyond our 24 μ m PSF. This redshift cut excludes only 82 objects (2% of the sample). In each bin, we take V_{min} to be the volume enclosed by the z_{max} of the adjacent lower redshift bin.

The MLE method was used to determine the shape of the local 24 μ m luminosity function (LLF). MLE requires no binning of data and is insensitive to

density variations, which is ideal for the lowest redshift regime where large scale structures affect the $1/V_{max}$ LF the most. We parameterize the LF with the double-power law proposed by Yahil et al. (1991).

$$\Psi(>L) = C\left(\frac{L}{L_*}\right)^{-\alpha} \left(1 + \frac{L}{L_*}\right)^{-\beta},\tag{5.1}$$

which corresponds to the differential luminosity function

$$\Phi(L) = \left(\frac{\alpha}{L} + \frac{\beta}{L + L_*}\right)\Psi(>L). \tag{5.2}$$

This functional form is commonly used to describe the MIR luminosity function (Shupe et al., 1998; Xu et al., 1998; Xu, 2000; Sanders et al., 2003; Magnelli et al., 2009). The Xu (2000) template was also used by Le Floc'h et al. (2005) to describe MIR LF evolution to $z \sim 1$. It should be noted that the turnover of the Schechter function (Schechter, 1976) frequently used for optical LFs is too steep to fit the IR LF (Rieke & Lebofsky, 1986; Yahil et al., 1991; Le Floc'h et al., 2005).

We determine the parameters by maximizing the likelihood function over the parameter space of the bright-end slope, α , the faint-end slope, β , and the characteristic luminosity, L_* , using the sample members in the redshift range of $0.05 \le z \le 0.25$. The normalization factor, C, has to be determined separately (since the factor cancels and does not appear in the likelihood function) by matching the integrated number density expected from MLE to that observed in the $1/V_{max}$ LF of the same sample. We constructed the LLF for both starforming and all-galaxy samples.

For the purpose of constructing a local luminosity function, the redshift range $0.05 \le z \le 0.25$ cannot be considered purely local. Especially with a population with the strong luminosity evolution of IR galaxies, the L_{*} estimate from such a wide redshift range would inherently be brighter than the true local L_{*}. To illustrate this, if we assume that the luminosity of IR galaxies evolves as $(1+z)^{3.3}$ and

the median redshift of the sample used for the LLF is z = 0.15, we would expect a 60% luminosity increase from the actual $L_*(z=0)$. There are a number of possible approaches to solve this problem. The first is to fit the luminosity evolution as a parameter in the MLE simultaneously while constraining the shape parameters. In practice such a fit would be difficult due to the additional free parameters and the degeneracy between luminosity and density evolution. One might need to fix some shape parameters (such as the faint-end slope) to achieve a plausible fit. The second approach would be to limit the redshift range of the sample to estimate the LLF. However, reducing the redshift bin size would compromise the constraints on the bright-end slope; we need to estimate the LLF using a sample selected to $z \le 0.25$ to encompass enough volume to find rare, bright galaxies. Others have faced the same problem. The Shupe et al. (1998) and Xu (2000) LLFs contain few bright galaxies as far as $z \sim 0.2$. Although their median redshift is much closer to local, the luminosity evolution could result in a more luminous L_{*} than the true local value. Another way to limit the redshift range to the local volume would be to rely on an MIR sample from all-sky IR surveys with shallow limiting fluxes such that the sample is limited to very nearby galaxies. But since all-sky surveys lack complete spectroscopic redshift follow-up and usually have to compile redshifts from several catalogs, the spectroscopic selection function of the combined sample may not be well understood. Robustly constraining a true local L_{*} is important because the local L_{*} is often used to constrain the evolution of the LF at higher redshifts, such as in Le Floc'h et al. (2005), who used the Sanders et al. (2003) local L_{*} derived from the IRAS 60 μ m-selected sample.

Our solution to this problem is to take advantage of the evolution information in our full sample, an option not available to studies limited to $z \lesssim 0.2$. The evolution constraint from the higher redshifts can be used to constrain the evolution

and extrapolate L* back to the true value at z = 0.0 (§ 5.3.5).

5.3.4 Bivariate Selection Bias

Since AGES spectroscopy was targeted on a flux-limited I-band parent catalog, our sample could be affected by biases created by excluding 24 μ m-bright, optically faint galaxies. This *bivariate selection bias* may result in a sample that systematically excludes galaxies with optically obscured star formation.

We quantify the possible bias by estimating the fraction of the 24 μ m number densities excluded because their contributing sources fall below the I-band flux limit. This can be done by constructing a 24 μ m LF as a function of I-band luminosity (bivariate luminosity function, or BLF) of a model sample constructed by evolving a sample at lower redshift, where it is complete to a fainter I-band luminosity, to a higher redshift bin of interest. To illustrate this experiment, consider the BLF in Fig. 5.5. In this case, we are investigating the bivariate selection effect for $0.35 \le z \le 0.50$. We construct a model sample by evolving a sample from $0.20 \le z \le 0.35$ (which is complete to deeper luminosity) in both I-band and 24 μ m to construct a BLF at $0.35 \le z \le 0.50$. As illustrated in Fig. 5.5, some objects would fall below the luminosity corresponding to the I-band flux limit (I=20.0) at the low-redshift edge of the bin (z=0.35) and would therefore be excluded from our sample, resulting in a fraction of the missing 24 μ m LF. We found, however, that this fraction is small (<2%) in this redshift bin, for 24 μ m luminosities above our 24 μ m completeness flux.

To model the evolution of L(I), we refer to Willmer et al. (2006) and Brown et al. (2007) who found that the optical characteristic magnitudes brighten by ~ 1.3 mag per unit redshift, which would correspond to a luminosity evolution law $L \propto (1+z)^{1.6}$ at $0 \leq z \leq 1$. For the 24 μ m luminosity evolution model, we adopted $L \propto (1+z)^{3.3}$ based on Pozzi et al. (2004); Le Floc'h et al. (2005) and

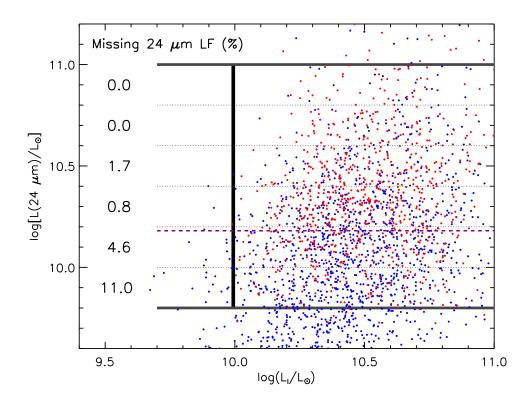


Figure 5.5: The 24 μ m and I-band bivariate luminosity functions (BLF) were constructed to quantify the effects of incompleteness at 24 μ m of MIR-bright, optically-faint galaxies (the bivariate selection bias). The BLF construction to quantify the bivariate selection bias for the sub-sample at redshift $0.35 \le z \le 0.5$ is illustrated in this figure. The blue dots illustrate the sample observed at $0.20 \le z \le 0.35$ evolved in both I-band and 24 μ m luminosities to match the distribution at $0.35 \le z \le 0.5$ (shown in red dots as a comparison). The solid vertical line is the luminosity, corresponding to the I-band limiting magnitude (I = 20) at z=0.35, below which a galaxy will be excluded from our $0.35 \le z \le 0.5$ sub-sample. The values indicated in the missing fraction column are the percent of the 24 μ m LF potentially excluded due to the bivariate selection bias (fraction of 24 μ m LF contributed by objects represented by blue dots on the left of the thick vertical line) in each $L(24 \mu m)$ bin (separated by the horizontal dotted lines). The horizontal dashed line indicates the luminosity corresponding to the 24 μ m completeness limit (0.27 mJy) at z = 0.50, above which 24 μ m sub-sample at $0.35 \le z \le 0.5$ is complete. We quantified the missing LF due to this effect to be less than 2% at $L(24 \mu m)$ above the completeness limit, indicating that our spectroscopic targeting method did not exclude significant numbers of MIR-bright, optically-faint galaxies.

Pérez-González et al. (2005).

We repeated this test for the other two higher redshift bins and found that the bivariate selection bias is negligible in the $0.20 \le z \le 0.35$ bin; none of galaxies is excluded from the sample in this redshift bin due to bivariate selection bias. Only in the highest redshift bin, $0.50 \le z \le 0.65$, does the missing fraction become more significant. In this bin we found the missing fraction in the $L(24~\mu\text{m})$ bins of $10^{10.7}$, $10^{10.9}$, and $10^{11.1}~L_{\odot}$ to be 8.7%, 4.4%, and 0.0% respectively.

The bivariate selection biases are under 5% for all but the lowest luminosity bin of our highest redshift sub-sample. We correct for it by by applying a correction factor based on the missing fraction estimated for each bin of the $1/V_{max}$ LF. This correction is included in the LF shown in Fig. 5.6. In a broader picture, this test indicates that our spectroscopic targeting method does not systematically exclude MIR-bright, optically-faint galaxies from the final sample.

5.3.5 Evolution of the Luminosity Function

The evolution of the 24 μ m LF is quantified using two methods. The first is to evolve the local LF template (§ 5.3.3) to fit the $1/V_{max}$ LF at higher redshifts so we can estimate the characteristic luminosity, L*, and any evolution in comoving number density as a function of redshift. The second is to determine the luminosity in each redshift bin at which the cumulative number density reaches a common threshold.

In the first method, we parameterize the LF evolution assuming a functional form of

$$\psi(L,z) = g(z)\phi\left[L/f(z)\right] \tag{5.3}$$

where $\phi(x)$ is given by equation (1). The terms $f(z) = (1+z)^{\alpha_L}$, and $g(z) = (1+z)^{\alpha_D}$ describe the evolution of the luminosity and number density with redshift, respectively. We then take our LLF determined by the MLE method (§ 5.3.3) as

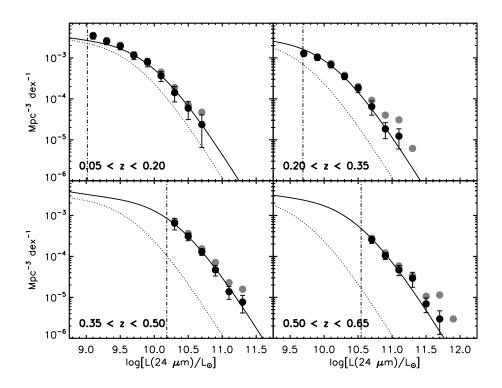


Figure 5.6: Evolution of the 24 μ m luminosity function (LF) of starforming galaxies (black circles) and all galaxies (grey circles, error bars omitted for clarity) for four redshift bins between $0.05 \le z \le 0.65$. The dotted LF is the local 24 μ m LF of starforming galaxies determined by the maximum likelihood estimator and the solid line in each panel is the local LF evolve to fit the starforming galaxy $1/V_{max}$ LF of the corresponding redshift bin (see § 5.3.5 and § 5.4.2). The vertical dot-dashed lines indicate the luminosity corresponding to the 24 μ m completeness flux at the upper limit of the redshift bin, above which our sample is complete. We note that the $1/V_{max}$ LF in the lowest redshift bin could be affected by the overdense region near $z \simeq 0.15$ (see Fig. 5.1). The strong evolution of the LF can be described by pure-luminosity evolution.

a local template and fit it to the $1/V_{max}$ LF in each higher redshift bin using χ^2 minimization and the median redshift of the bin. By using the LLF as a template, we assume a fixed LF shape across the redshift range, and focus on the change in L_* and C as a function of redshift. To fit the LF template to the $1/V_{max}$ LF, we only consider $1/V_{max}$ data points above the luminosity corresponding to the 80% completeness flux threshold (0.27 mJy) at the upper redshift limit of the bin. Below this luminosity our sample in the corresponding redshift bin is no longer complete. The fit is done in two ways: fitting all redshift bins simultaneously to estimate the global evolution of the LF at $0.0 \le z \le 0.6$, and fitting each bin individually to explore any bin-specific deviations from the global law. We also integrate the individually fitted LFs over luminosity to determine the luminosity density, which will be used to estimate the star formation rate density ($\hat{\rho}_*$ § 5.3.6).

As mentioned in \S 5.3.3, the LLF is affected by the evolution of IR galaxies within the redshift bin where the LLF was constructed. With a known median redshift of the LLF sample (z=0.17 for both starforming and all-galaxy samples), we can use χ^2 minimization to give the best fit evolution law that would evolve the L_{*} of the LLF from $L_*(z_{median})$ back to $L_*(z=0)$ and simultaneously evolve the LLF with $L_*(z=0)$ to fit the $1/V_{max}$ LF at all higher redshift bins. After using the global luminosity evolution constraint to evolve L_{*} back to z=0, we can then use $L_*(z=0)$ as a local anchor point to quantify the luminosity evolution in each bin individually.

In the second method to quantify luminosity evolution, we determined the luminosity at which the corresponding cumulative number density reaches a common arbitrary threshold in each redshift bin. The *individual* fit of the LF is integrated downward in luminosity from the bright-end until the integrated number density reaches $10^{-4} {\rm Mpc}^{-3}$. This method robustly quantifies the luminosity evo-

lution because the bright-end of our LF is very well constrained and little affected by incompleteness.

5.3.6 Estimation of SFR

We adopt the SFR calibration of Rieke et al. (2009) to estimate the SFR from the observed $F_{\nu}(24 \,\mu\text{m})$. Every SFR indicator using infrared luminosity is based on the assumption that UV radiation from young stars is efficiently reprocessed into IR radiation, and that the fraction of UV radiation escaping the starforming regions without being reprocessed is small. This escape fraction depends strongly on the total-IR luminosity since more luminous IR emission implies greater UV and optical extinction. This relationship has been studied by comparing the L(UV)and L(TIR) of galaxies (Schmitt et al., 2006; Buat et al., 2007), who found that the UV contribution to the total luminosity (the UV escape fraction) is about 20% for galaxies with L(TIR) equivalent to $L(24 \, \mu m) \simeq 10^{8.65} \, L_{\odot}$ and decreases rapidly to 8% and 2.5% at $L(24 \,\mu\mathrm{m}) \simeq 10^{9.6} \,L_{\odot}$ and $L(24 \,\mu\mathrm{m}) \simeq 10^{10.1} \,L_{\odot}$, respectively. Therefore the calorimetric condition can be assumed for our normal starforming galaxies, whose $L(24 \mu m)$ are in the range of $10^8 - 10^{10} L_{\odot}$, although the error will increase between 10^8 and $10^{8.65}$ L_{\odot} . This is relevant only at the lowest redshifts. We note that the Rieke et al. (2009) 24 μ m SFR calibration has a scatter of < 0.2dex, but a relative trend such as the $\dot{\rho}_*$ evolution law will not be affected by this scatter so long as the sample is large. The luminosity density that we use to estimate the star formation rate density $(\dot{\rho}_*)$ is calculated by integrating the fitted LFs (§ 5.3.5) in each redshift bin over luminosity from 10^6 to $10^{15} L_{\odot}$.

The IR SFR indicators are calibrated with local SEDs. Employing these indicators at higher redshifts carries an assumption of no or little SED evolution over the relevant range of z (to 1.2). This assumption is supported by Marcillac et al. (2006), Bayouzet et al. (2008) and Magnelli et al. (2009). There are indications that,

at redshifts of $z\sim 2$, the calibration of the observed 24 μm flux density and SFR may shift from values deduced from local SED templates (Papovich et al., 2007; Rigby et al., 2008; Farrah et al., 2008). The primary cause of these changes appears to be that the aromatic bands tend to be stronger for a given luminosity at high redshift, so the SEDs resemble more closely those of local galaxies with significantly smaller total infrared luminosity. The probable cause of this behavior is that local ULIRGs tend to have intense star formation concentrated into very optically thick nuclear regions, whereas galaxies of similar infrared luminosity at high redshift probably have more widely distributed star forming regions of lower optical depth. It is unlikely that this effect significantly alters the calibration of SFRs in this paper. First, the effect appears to be weaker for normal starforming galaxies and galaxies of LIRG-level luminosity even at high redshift (Rigby et al., 2008); the galaxies that dominate our study are of lower luminosity still. Second, given their relatively low redshifts, the observed 24 μ m flux densities from our galaxies are not strongly affected by the aromatic band strengths. Third, the evolutionary state of our galaxies should resemble local galaxies at least as much as it does those at $z \sim 2$; in fact, Magnelli et al. (2009) show that the SEDs of infrared galaxies for $0.4 \le z \le 1.2$ resemble those of local galaxies reasonably closely.

5.3.7 Uncertainties Analysis for the LF and SFR

We use jackknife resampling to estimate the uncertainties in our $1/V_{max}$ LFs and the LLF parameters (α , β , L_* , and the normalization factor; see § 5.3.3), as well as star formation rate density and evolution laws derived from the LFs.

The AGES survey used 15 overlapping tiles corresponding to the Hectospec field of view. These tiles are a natural way to build 15 jackknife samples, each dropping one of these roughly 1-degree diameter tiles and then using the variance in parameter estimates for these 15 sub-samples to estimate the uncertain-

ties. This procedure will include Poisson uncertainties and sub-degree-scale cosmic variance effects. It will underestimate uncertainties due to larger scale correlations between galaxies.

We can estimate the large scale effects by shifting the entire LF estimation for each redshift bin by our estimate of the total cosmic variance and recalculating the parameters. The cosmic variance on the scale of our survey volume ($\sim 10^6 {\rm Mpc}^3$) can be estimated using Peebles (1980) and by assuming the power-law correlation function estimated from the SDSS for late-type galaxies, $\xi = (r/r_0)^{-\gamma}$, with $r_0 = 3.6 \ h^{-1} {\rm Mpc}$ and $\gamma = 1.7$ (Zehavi et al., 2005). In the bins of redshift $0.05 \le z \le 0.20, 0.20 \le z \le 0.35, 0.35 \le z \le 0.50$, and $0.50 \le z \le 0.65$, we expect the uncertainties on the LF due to cosmic variances to be 15%, 11%, 10%, and 9%, respectively (Dai et al., 2009).

5.4 Results

Here we will discuss our determination of the local 24 μ m LF and compare it to other studies (§ 5.4.1) to establish a baseline for our study of LF evolution to $z \sim 0.6$ (§ 5.4.2). Next, we discuss the evolution constraints based on the combination of our Boötes field data and the 35 μ m LF evolution from Magnelli et al. (2009) who focused on $0.4 \le z \le 1.3$ (§ 5.4.3) using the FIDEL survey. The combination of these two studies lets us determine the $\dot{\rho}_*$ evolution from $0 \le z \le 1.2$ in a unified and accurate way. We will then present the local star formation rate density and the star formation rate density evolution derived from the LFs (§ 5.4.4).

5.4.1 Local 24 μ m Luminosity Functions

The local 24 μ m LFs for both the starforming and all-galaxy populations are shown in Fig. 5.7. Both LLFs are constructed from a sample at $0.05 \le z \le 0.25$ (median redshift z=0.17) and evolved back to z=0.0 using the global evolution

law estimated in § 5.3.5. Their shape parameters are tabulated in Table 5.1 along with other estimates of the LLF using the double-power law form of equation.

The starforming and all-galaxy LLFs have identical faint-end slopes, but the starforming LLF has a slightly steeper bright-end slope and a brighter characteristic luminosity. Both differences are within the uncertainties of the respective parameters, but nevertheless the steeper slope of the starforming LLF is expected because the sample excluded the IR-luminous AGN, as illustrated in Fig. 5.4. This comparison shows that the overall impact of AGN on the LLF is small, and that any residual unidentified AGN should have little effect on our conclusions. In Fig. 5.7 we present our LLF along with the bandpass and cosmologically adjusted $1/V_{max}$ LLF of Rush et al. (1993), Sanders et al. (2003) and Pozzi et al. (2004), and the MLE LLF of Shupe et al. (1998).

One of the most important parameters of the LLF is the value of $L_*(z=0)$. Our L_* estimates for the starforming and all-galaxy populations are $(4.27\pm0.71)\times 10^9$ and $(4.07\pm0.67)\times 10^9$ L_\odot , respectively. We compare our results with other works that adopt the double power-law form of LF by correcting for cosmological assumptions and bandpasses using the Rieke et al. (2009) SED library. The Shupe et al. (1998) LLF using IRAS 25 μ m measurements reports a local L_* of $(4.67\pm0.41)\times 10^9$ L_\odot , which corresponds to $(4.47\pm0.40)\times 10^9$ L_\odot when corrected for the difference between the IRAS 25 μ m and MIPS 24 μ m bandpasses. Xu et al. (1998) report an ISO 15 μ m local L_* of $(4.79\pm1.69)\times 10^9$ L_\odot , corresponding to $(6.40\pm2.25)\times 10^9$ L_\odot at 24 μ m. Sanders et al. (2003) report a local total-IR L_* of $10^{10.5}L_\odot$, which corresponds to a 24 μ m L_* of 4.4×10^9 L_\odot . Our estimate of L_* agrees well with all these other studies. More importantly, the extrapolation of the LLF L_* back to z=0.0 using the luminosity evolution constraint from our full sample ensures that these values reflect an accurate value at z=0 in addition

Table 5.1. Parameters of the mid-IR local luminosity function in comparison with other works

Reference ^a	α	β	$L_*(24~\mu\mathrm{m})$ ($10^9\mathrm{L}_\odot$)	C $(10^{-3} \rm{Mpc}^{-3})$
All Galaxies	0.36 ± 0.04	2.17 ± 0.35	4.07 ± 0.67	1.2 ± 0.8
Starforming	0.37 ± 0.04	2.36 ± 0.41	4.27 ± 0.71	1.2 ± 0.8
Shupe et al. (1998)	0.437 ± 0.032	1.749 ± 0.067	4.47 ± 0.40	1.0 ± 0.6
Xu et al. (1998)	0.47 ± 0.13	2.20 ± 0.13	6.40 ± 2.25	0.9 ± 0.5
Sanders et al. (2003)	0.6 ± 0.1	2.2 ± 0.1	4.4	$0.8^{\rm b}$

^aResults from other studies are corrected for their bandpass differences to reflect estimates at 24 μ m using the Rieke et al. (2009) SED library. Redshift ranges for each study are the following. This study: $0.05 \le z \le 0.25$, median redshift of 0.17 in both samples, with L* evolve back to z=0.0 (for both all-galaxy and starforming sample) simultaneously with the evolution fit (see § 5.3.5); Shupe et al. (1998): $0.001 \le z \le 0.07$; Xu et al. (1998): $0.02 \le z \le 0.22$; Sanders et al. (2003): median and mean redshifts of 0.0082 and 0.0126, respectively.

^bSanders et al. (2003) do not report their normalization explicitly but a power-law break fit to their $1/V_{max}$ LLF (see their Table 6) suggests a value of 8×10^{-4} Mpc⁻³.

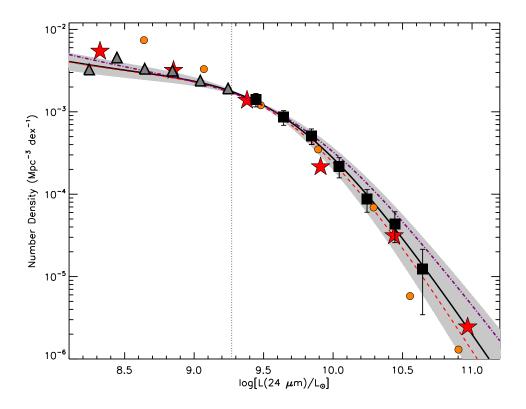


Figure 5.7: The mid-IR local luminosity function (LLF). We construct the LLF for the all-galaxy (solid black line) and starforming (dashed red line) samples. The $1/V_{max}$ LLF points are shown in black squares above the luminosity corresponding to the 24 μ m completeness flux limit at the upper limit of redshift range where we select the sub-sample to construct the LLF (0.27 mJy at z=0.25, vertical line) and lower-limits (upward triangles) below this completeness threshold. Note that this completeness limit does not affect the maximum likelihood (MLE) LLF. Uncertainties in the bright and faint-end slopes of the MLE LLF derived from the jackknife analysis are illustrated by the shaded area. The mid-IR LLFs from Rush et al. (1993); Shupe et al. (1998) and Sanders et al. (2003) are corrected for bandpass differences and shown in circles, dot-dashed line, and stars, respectively. The consistency of our LLF shape with previous work shows that it is a reliable local anchor point to study the evolution of the LF.

to providing the best-match LLF template to study the evolution of the LF in our sample.

5.4.2 Evolution of the 24 μ m LF

Strong luminosity evolution is evident in the $1/V_{max}$ LFs over the redshift range $0.05 \le z \le 0.65$ shown in Fig. 5.6. We considered two evolutionary scenarios for the 24 μ m LF parameterized by equation (3), including pure luminosity evolution and pure density evolution. These scenarios were tested by evolving our local 24 μ m LF to fit the $1/V_{max}$ LF at higher redshift by χ^2 minimization. We cannot constrain a combined luminosity and density evolution model because we do not sample below L** in these higher redshifts sub-samples. The density evolution model can be rejected on the basis of the χ^2 values with high confidence. Other studies have found that the density evolution is small. Le Floc'h et al. (2005) and Pérez-González et al. (2005) derived a density evolution laws of $\phi^* \propto (1+z)^{0.7^{+0.2}_{-0.6}}$ and $\phi^* \propto (1+z)^{1.0\pm0.3}$, respectively. More recently, Magnelli et al. (2009) used a stacking analysis to study the evolution of the 35 μ m LF and reported density evolution given by $\phi^* \propto (1+z)^{0.1\pm0.7}$ at $z \lesssim 1.2$. This implies a density variation of about $5\% \pm 40\%$ at $0.0 \le z \le 0.6$, which is comparable to the uncertainties due to cosmic variance in the density.

Using a pure luminosity evolution model, we obtain an evolution law given by $L_*(24~\mu\mathrm{m}) \propto (1+z)^{3.8\pm0.3}$ for the starforming sample. This luminosity evolution is shown as a fit to the $1/\mathrm{V}_{max}$ LF in Fig. 5.6. One of the evolution descriptions of Pérez-González et al. (2005) uses pure luminosity evolution with the Schechter (1976) form of LF. They report luminosity evolution of $(1+z)^{3.6\pm0.3}$ for z<0.8, agreeing with our result. The evolution of the LF was also quantified by determining the luminosity above which the cumulative number density reached $10^{-4}\mathrm{Mpc}^{-3}$; as tabulated in Table 5.2. This luminosity increases by more than a

Table 5.2. The 24 μ m and total-IR luminosities above which the cumulative number density of starforming galaxies is $10^{-4} \mathrm{Mpc}^{-3}$ for each redshift bin

Redshift Bin	$L(24~\mu{ m m})$ $10^{10}L_{\odot}$	$L({ m TIR})^{ m a}$ $10^{10} L_{\odot}$
0.05 < z < 0.20	1.2 ± 0.4	9.2 + 2.9
$0.03 \le z \le 0.20$ $0.20 < z < 0.35$	1.2 ± 0.4 1.7 ± 0.4	9.2 ± 2.9 13.2 ± 3.0
$0.35 \le z \le 0.50$	2.5 ± 0.5	18.9 ± 3.7
$0.50 \le z \le 0.65$	3.9 ± 0.7	28.1 ± 5.3

 $^{\mathrm{a}}L(\mathrm{TIR})$ is estimated using the Rieke et al. (2009) formalism.

factor of three from a redshift of 0.05 to 0.65. We should note that while we cannot jointly constrain luminosity and density evolution, the simple power-law model is an adequate description of our data. Improving on it would require a deeper sample in a comparably large area to the Boötes field.

Our method to determine evolution of the LF assumes no evolution in LF shape from the local template. The template, however, yields a better fit at low redshift than in the higher redshift bins. Discrepancies between the template and the data are most visible at $0.50 \le z \le 0.65$ (Fig. 5.6). This discrepancy could be due to an intrinsic evolution toward a shallower bright-end slope at higher redshifts. On the other hand, it could indicate a contribution from unidentified AGN in the higher 24 μ m luminosity regime. The latter explanation is consistent with the observation that AGN are progressively more abundant at higher redshifts

(Fig. 5.4) as well as from Fig. 5.6 itself, which shows that the bright-end slope of the $1/V_{max}$ LF of all galaxies (including AGN) becomes shallower to a greater extent compared to that of the starforming galaxy LF.

5.4.3 Extending the LF evolution constraint to $z \sim 1.2$

We augment our LF evolution constraint at low and intermediate redshifts with the result of Magnelli et al. (2009) at 35 μ m. This is a useful combination because Magnelli et al. (2009) used the deep (50 μ Jy and 3 mJy at 24 and 70 μ m, respectively), narrow-field (0.5 sq. deg.), FIDEL survey. The FIDEL sample has \sim 7000 and \sim 600 starforming galaxies detected at 24 μ m and 70 μ m, respectively, with known redshifts. AGN were excluded on the basis of deep (200 ks - 2 Ms) X-ray observations. Additionally, Magnelli et al. (2009) employ a stacking analysis to provide further constraints for the LFs. Their approach provides one of the best evolution constraints for the LFs at higher redshifts to date but will be affected by cosmic variance at intermediate redshifts, where our results should be more reliable. In addition, the rest frame 35 μ m values can be corrected to 24 μ m with minimal uncertainties due to luminosity conversions.

We need to correct Magnelli et al. (2009) for (1) bandpass differences; and (2) k-correction differences (SED assumptions). To correct for bandpass differences, we use the Rieke et al. (2009) SED library to calculate a luminosity-dependent conversion factor between the Magnelli et al. (2009) rest-frame 35 μ m, which was observed at 70 μ m and k-corrected to z=1 (the observed 70 μ m band probes the 35 μ m rest-frame SED at z=1). This conversion factor varies slowly from 0.5 at $L(\text{TIR}) \sim 10^{10} L_{\odot}$ to 0.3 at $L(\text{TIR}) \sim 10^{12} L_{\odot}$. Next we compare the consistency of the Chary & Elbaz (2001) SED used by Magnelli et al. (2009) and our Rieke et al. (2009) SED. The best test for differences lies in the $L_*(z=0)$ anchor point, $L_*(z=0,35~\mu\text{m})=10^{9.85}~L_{\odot}$, that Magnelli et al. (2009) obtained by converting

the Shupe et al. (1998) IRAS 25 μ m L_{*} to 35 μ m (MIPS 70 μ m observed bandpass at z=1) using the Chary & Elbaz (2001) SED. Converting this L_{*}($z=0,35~\mu$ m) back to our MIPS 24 μ m rest-frame (which is about 5% fainter than the original value at 25 μ m) using the Rieke et al. (2009) SED would yield L_{*}($z=0,24~\mu$ m) of $3.72\times10^9~h^{-2}L_{\odot}$, which is 20% lower than the original Shupe et al. (1998) value tabulated in Table 5.1. In other words, a 20% discrepancy resulted from subjecting a luminosity through this conversion exercise and we must apply a +20% correction factor to the FIDEL data points to correct for SED differences.

For the combined fit, we omitted two data points. First, we dropped the lowest redshift Magnelli et al. (2009) bin $(0.4 \le z \le 0.7)$, which overlaps with our highest redshift bin, because this redshift bin will be more strongly affected by cosmic variance since our highest redshift bin encompasses about an order of magnitude more volume. Second, we dropped our local point because it was estimated by evolving the sample in the lowest redshift bin $(0.05 \le z \le 0.20)$ back to z = 0.0 based on the higher redshift bins (§ 5.3.5), so including this point would "double count" the data. Instead we use the Shupe et al. (1998) local point converted to 24 μ m. Note, however, that our local L_* estimate is consistent with Shupe et al. (1998). The combined fit yields (shown in Figure 5.8) a slightly shallower evolution law than that estimated from the Boötes field alone (§ 5.4.2), with $L_{*,combined} \propto (1+z)^{3.4\pm0.2}$.

5.4.4 The Evolution of the Star Formation Rate Density

Now that we have constructed the LF and determined the luminosity evolution from z=0.0 to 1.2 we can provide a complete picture of the $\dot{\rho}_*$ evolution from z=0.0 to $z\sim1.2$. We compute SFRs based on Kroupa (2002) IMF used by Rieke et al. (2009). This leads to estimates of $\dot{\rho}_*$ a factor of 0.66 lower than those assuming a Salpeter (1955) IMF with a single power-law slope of -1.35 from 0.1

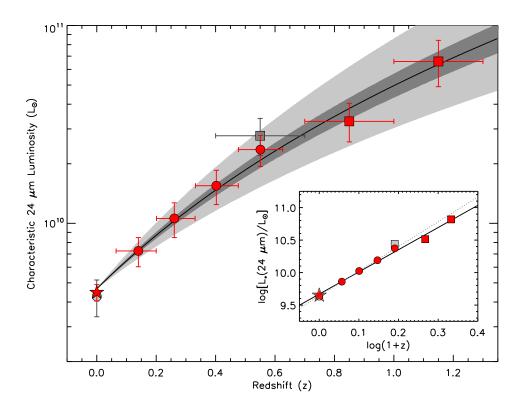


Figure 5.8: Evolution of the characteristic 24 μ m luminosity of galaxies, L*, to $z\sim 1.2$ based on our results (red circles) and that of Magnelli et al. (2009) using FIDEL (red squares). The light shaded area is the luminosity evolution law $L_*\propto (1+z)^{\alpha_L}$ bounded by α_L of 2.7 and 4.2 from the lowest and highest uncertainty limits of Pérez-González et al. (2005) and Magnelli et al. (2009), respectively. The combined evolution law, $L_{*,combined}\propto (1+z)^{3.4\pm0.2}$, is shown as a solid line with the uncertainties from the combined fit shown by the dark shaded area. The local point for the global fit (red star) is that of Shupe et al. (1998) converted to 24 μ m. Two data points were excluded from the fit (see details in § 5.4.3) and are shown in grey. Inset: The combined of luminosity evolution (solid line) with the same symbols as the main figure (error bars are omitted for clarity) and the fit (dotted line) based on the Boötes data alone, $(1+z)^{3.8\pm0.3}$.

to 100 M_{\odot} .

Our estimates for $\dot{\rho}_*$ in each redshift bin to $z\sim 1.2$, including both our results and the adjusted values from Magnelli et al. (2009), are tabulated in Table 5.3, and shown in Fig. 5.9 along with $\dot{\rho}_*$ measurements from other wavelengths from the UV to radio. Based on the fit of the combined data out to $z\sim 1.2$, our $\dot{\rho}_*$ evolution law is given by

$$\log(\dot{\rho}_*) = (3.5 \pm 0.2)\log(1+z) - 1.96 \pm 0.08 \tag{5.4}$$

At z=0 our fit yields a local $\dot{\rho}_*$ of $(1.09\pm0.21)\times10^{-2}M_{\odot}{\rm yr}^{-1}{\rm Mpc}^{-3}$ for Kroupa (2002), which corresponds to $\dot{\rho}_*$ of $(1.65\pm0.32)\times10^{-2}M_{\odot}{\rm yr}^{-1}{\rm Mpc}^{-3}$ for a Salpeter (1955) IMF. Our estimate agrees with previous works on the local $\dot{\rho}_*$ that have properly accounted for the internal extinction of the galaxy. Without such corrections the $\dot{\rho}_*$ will be underestimated by 50 - 70 % (Gallego et al., 1995; Tresse & Maddox, 1998; Hanish et al., 2006; Salim et al., 2007). The agreement between $\dot{\rho}_*$ estimates corrected for internal extinction and our $\dot{\rho}_*$ derived from 24 μ m luminosity suggests that \sim half of the local star formation is obscured and the MIR provides a direct and reliable means for SFR measurement.

Fig. 5.9 illustrates the good agreement of the normalization of our $\dot{\rho}_*$ estimates and those derived from the UV observation corrected for the effects of intrinsic extinction of the target galaxies (normalization corrections can be as large as 0.7-dex; e.g., Fig. 5 of Schiminovich et al. (2005) illustrates the extent of the required correction for the UV observations). Hopkins (2004) reports the fit to a compilation of the $\dot{\rho}_*$ that has been corrected for extinction of the target galaxies with an assumption of a luminosity-dependent obscuration. The resulting best fit is given by $\log(\dot{\rho}_*) = (3.29 \pm 0.26)\log(1+z) - 1.98 \pm 0.04$ (assuming the Kroupa (2002) IMF), which also agrees well with our evolution determined from the combination of

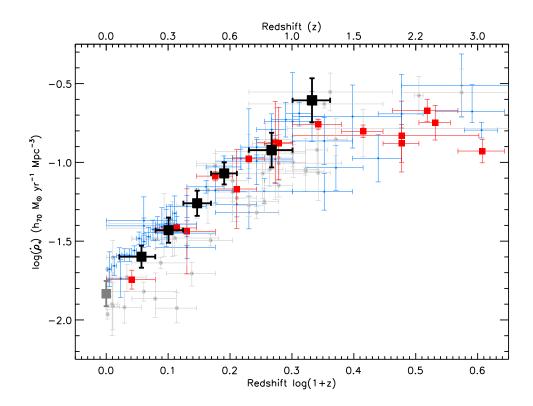


Figure 5.9: Evolution of the star formation rate density $(\dot{\rho}_*)$ as a function of redshift assuming Salpeter (1955) IMF. Our $\dot{\rho}_*$ estimates are shown in large black squares and our extrapolated local point (§ 5.4.1) shown in grey, compared to the $\dot{\rho}_*$ from the following. The extinction-corrected UV $\dot{\rho}_*$ from the compilation of Hopkins (2004) and Hopkins & Beacom (2006) are shown in blue circles; IR $\dot{\rho}_*$ in red squares (Hopkins, 2004; Pérez-González et al., 2005; Reddy et al., 2008); grey dots are the radio (1.4 GHz), X-ray, and extinction-corrected [OII], H α , and H β $\dot{\rho}_*$ (Hopkins, 2004; Seymour et al., 2008; Smolčić et al., 2009; Zhu et al., 2009). The agreement of our $\dot{\rho}_*$ normalization and those from extinction-corrected optical and UV observations confirms that a majority of star formation at z < 1.2 is obscured and can be directly traced by 24 μ m observation.

Table 5.3. Evolution of the characteristic 24 μ m luminosity, L*(24 μ m), and the star formation rate density, $\dot{\rho}_*$, to $z\sim 1.2$

Redshift	$L_*(24~\mu m)$ $10^9~L_\odot$	$\log(\dot{ ho}_*)^{\mathrm{a}}$
0.00 (This Work)	4.27 ± 0.71	-1.83 ± 0.08
0.00 (Shupe et al., 1998)	4.47 ± 0.40	-1.71 ± 0.04
$0.05 \le z \le 0.20$	7.25 ± 1.12	-1.60 ± 0.07
$0.20 \le z \le 0.35$	10.6 ± 1.8	-1.43 ± 0.08
$0.35 \le z \le 0.50$	15.5 ± 2.4	-1.26 ± 0.08
$0.50 \le z \le 0.65$	23.6 ± 3.6	-1.07 ± 0.07
$0.7 \le z \le 1.0^{\rm b}$	32.8 ± 7.8	-0.92 ± 0.11
$1.0 \le z \le 1.3^{\rm b}$	65.8 ± 18.8	-0.61 ± 0.14

 $^{^{\}rm a}\dot{
ho}_*$ estimates assume a Salpeter (1955) IMF and are given in the unit of $M_{\odot}{
m yr}^{-1}{
m Mpc}^{-3}$. Assuming the Kroupa (2002) IMF would yield 0.66 $\dot{
ho}_*$ given here.

 $^{^{\}mathrm{b}}$ Based on FIDEL luminosity functions (Magnelli et al., 2009).

the NDWFS and the FIDEL results. Again, this agreement confirms that star formation at redshift 0.0 < z < 1.2 occurs in obscured environments and can be traced directly with 24 μ m observations given a proper classification and exclusion of AGNs. It should be noted that our result is consistent with findings of Takeuchi et al. (2005), which show an evolution of the fraction of obscured star formation from 50% locally to > 80% at $z \sim 1$.

5.5 Chapter Conclusions

We study the evolution of 24 μ m-selected galaxies by constructing their 24 μ m (rest-frame) luminosity functions (LF). Our sample contains 4,047 galaxies with spectroscopic redshifts at $0.0 \le z \le 0.65$ in the Boötes field of the NOAO Deep-Wide Field Survey (NDWFS). The 24 μ m data and spectroscopic redshifts were obtained with *Spitzer* and with the AGN and Galaxies Evolution Survey (AGES), respectively. Our sample is a unique combination of wide field, spectroscopic redshifts, and 24 μ m imaging that is ideal for intermediate redshifts where MIR galaxy evolution has not been well-studied. The large area (9 sq. deg.) of the Boötes field helps mitigate cosmic variance, which otherwise can be a serious issue at low and intermediate redshifts. Theoretically, the cosmic variance in our study is less than 10% at z>0.2. Spectroscopic redshifts reduce cross-talk between redshift bins and faint/bright end slope biases and provide an accurate number density contribution for each object.

Galaxies exhibiting AGN activities characterized by X-ray emission and mid-IR power-law are excluded from our starforming sample. We find that the optical line diagnostics (the BPT method) are not suitable for identifying AGN dominant at mid-IR wavelengths because the mid-IR emission from optically-selected AGNs is often dominated by star formation. We identified 288 objects with 24

 μ m emission likely to be dominated by AGN. Excluding them leaves a sample of 3,759 starforming galaxies.

We derive the 24 μ m luminosity using calibrations derived from the most recent SED library of the mid-IR spectra from *Spitzer* (Rieke et al., 2009). Our sample is comprised mainly of normal starforming galaxies (66% have $L(\text{TIR}) < 10^{11}$ L_{\odot}) and LIRGs (33% have 10^{11} $L_{\odot} < L(\text{TIR}) < 10^{12}$ L_{\odot}). Only 1% are ULIRGs ($L(\text{TIR}) > 10^{12}$ L_{\odot}) and we found that most of the ULIRGs contain AGN.

We construct the local 24 μ m luminosity function (LLF) as a template to study evolution of the LF. Our LLF was constructed at $0.05 \le z \le 0.25$ and evolved back to z=0 simultaneously with the fit to constrain the global evolution of our sample. The LLF template for our starforming sample is given by a double power-law with faint-end slope, $\alpha=0.37\pm0.04$, bright-end slope, $\beta=2.36\pm0.41$, characteristic luminosity, $L_*(z=0)=(4.27\pm0.71)\times 10^9 L_\odot$, and density normalization, $C=(1.2\pm0.8)\times 10^{-3} {\rm Mpc}^{-3}$. Our major results are:

- 1. The evolution of the LF at $z \leq 0.65$ can be represented by pure luminosity evolution with the characteristic 24 μ m luminosity of starforming galaxies evolving as L_{*}(24 μ m) $\propto (1+z)^{3.8\pm0.3}$. We demonstrate by the construction of the bivariate I-band and 24 μ m luminosity function that the fraction of missing 24 μ m-luminous, optically-faint galaxies due to our I-band magnitude limit for spectroscopic targeting is very small.
- 2. We extend the constraint on the evolution of L_* to $z\sim 1.2$ by combining our results with the higher redshift results from Magnelli et al. (2009) based on the FIDEL survey. The combined sample gives a slightly shallower luminosity evolution of $L_*(24~\mu\text{m}) \propto (1+z)^{3.4\pm0.2}$. The shallower evolution law derived by

including the FIDEL sample at redshifts of z=0.85 and 1.15 suggests that the evolution in $\dot{\rho}_*$ may begin to slow compared to lower redshifts.

3. The local star formation rate density based on our 24 μ m data is $\dot{\rho}_*$ of $(1.09\pm0.21)\times10^{-2}M_{\odot}{\rm yr}^{-1}{\rm Mpc}^{-3}$ assuming the Kroupa (2002) IMF, which corresponds to $\dot{\rho}_*$ of $(1.65\pm0.32)\times10^{-2}M_{\odot}{\rm yr}^{-1}{\rm Mpc}^{-3}$ for a Salpeter (1955) IMF. The combined evolution constraint for the LF at $z\leq1.2$ indicates that $\dot{\rho}_*$ evolves as $\dot{\rho}_*\propto(1+z)^{3.5\pm0.2}$. Our normalization and evolution measurements agree well with the $z\lesssim1$ extinction-corrected findings from other studies, which confirms that most of star formation is obscured and that 24 μ m serves as a direct and reliable $\dot{\rho}_*$ indicator in these cases.

We thank Benjamin Weiner, Benjamin Magnelli, Christopher Willmer, and Pablo Pérez-González for invaluable discussions. WR thanks Andrew Hopkins for supplying his $\dot{\rho}_*$ compilation and Xinyu Dai for his inputs on the cosmic variance in the Boötes field. This work was supported by the contract 1255094 from JPL/Caltech to the University of Arizona. WR was supported by Spitzer archival grant JPL-1278815, NSF AST-0607541, and the Thai Government Scholarship.

CHAPTER 6

SUMMARY AND THE WAY FORWARD

In the late 1990s, the *Hubble Space Telescope* and large ground-based telescopes allowed astronomers to measure the Cosmic SFR history back to $z \sim 1$ for the first time. Apart from revealing that the Cosmic SFR was $20 \times$ greater than the present, comparison of optical and infrared (e.g., from ISO) deep-field surveys found that star formation at high-z occurs in obscured environments, where dust absorbs most of the UV and re-radiates in the thermal IR. *ISO* and *Spitzer* confirmed that the number counts of IR galaxies evolve rapidly with redshift, and that high-redshift star formation was indeed obscured: luminous IR galaxies (LIRGs; galaxies with total infrared luminosities $> 10^{11} L_{\odot}$) dominate the Cosmic SFR history beyond z = 0.7 (e.g., Le Floc'h et al., 2005).

Major questions at the time I began my graduate study were, for instance: Are high-*z* starburst galaxies triggered and fueled by mergers like their local counterparts? Are AGN common in star-forming galaxies, or do they prefer quiescent ones? If AGNs are indeed ubiquitous, would mid-IR observations be useful as SFR tracers at high-*z*? What shut off the Cosmic star formation? These questions may be interconnected: if high-*z* starbursts are indeed triggered by mergers, and if the most luminous starbursts harbor AGNs like local ULIRGs, AGN would be very common at high-*z*, the Cosmic SFR decline would largely be explained by feedback from merger-triggered AGNs, and the mid-IR wavelength would be dominated by AGN emission. This scenario is elegant, and was a plausible explanation for some time, but it must compete with the simpler picture of the exhaustion of the molecular gas fuel for new stars. Over the course of the past half a decade, it gradually dawned on us that mother nature is more complicated

than we had imagined and that both explanations could be proven right in their respective regimes: secular evolution for most typical starbursts (>99% by numbers) and merger-driven SF/AGN in the most luminous starbursts (<1%). Our understanding of galaxy evolution is far from complete, but the voids are being filled rapidly, especially in the era of *Spitzer* and *Herschel*. The summary of the contribution of this thesis is as follows.

6.1 Systematic study of the structure of star-forming galaxies from local to high-z

Observations from *Spitzer* showed that the spectral energy distributions (SEDs) of local and high-z ULIRGs are different. Compared to local counterparts with similar total infrared luminosities, L(TIR), ULIRGs at high-z exhibit stronger aromatic (PAH) emission, colder dust, and Pa α emission that indicates a lower extinction at high-z (Rigby et al., 2008; Symeonidis et al., 2009; Papovich et al., 2009). All these suggest that local and high-z ULIRGs could have fundamentally different structures. The physical size of the galaxy-wide star-forming regions is the most fundamental structural parameter. But there has been no systematic study of the sizes of star formation regions over a large redshift range, because they are difficult to measure from local to high-z under a consistent metric.

In Chapter 2, I presented the star-forming sizes of local and high-z ULIRGs using Pa α , 24 μ m and radio continuum observations, which trace nearly identical physical regions despite different emission physics (Rujopakarn et al., 2011). I discovered that high-z ULIRGs have extended SF regions over 3-10 kpc, similar to local lower L(TIR) SF galaxies, but with the star formation rate surface density, Σ_{SFR} , scaled up by 100-1,000 times. Local ULIRGs, in contrast, are compact and nearly all merger-triggered starbursts (Sanders & Mirabel, 1996). The results from

this chapter are confirmed by many recent observations, such as those of Elbaz et al. (2011) and Gladders et al. (2012) using *Herschel* far-IR observations; Nelson et al. (2012) using *Hubble* near-IR grism spectroscopy, as well as by numerical simulations (e.g., Niemi et al., 2012).

A major implication to galaxy evolution is that there is a route besides major mergers to trigger very high levels of SF activity at $z\sim 2$. This conclusion is further supported by the optical morphological study using Hubble imaging (Section 2.2.3), which indicates that only $\sim 1/3$ of star-forming galaxies in the Hubble Deep Field show signs of disturbed morphologies. The smaller fraction of galaxies that exhibit merger signs and the extended structure of star formation further suggest that major mergers played lesser role in fueling starbursts at high z compared to other secular processes, e.g., larger gas reservoir (Davé et al., 2010). Mergers may contribute significantly in triggering the anomalously luminous starbursts at the bright-end of the luminosity function (e.g., at $L({\rm TIR})>10^{13}~L_{\odot}$), but not in the typical starburst galaxies ($L({\rm TIR})$ of $10^{12}-10^{11}~L_{\odot}$), which is 100-1,000 times more common at z=1-3.

6.2 A new mid-IR star formation rate indicator for 0 < z < 3

In deep surveys, *Spitzer* 24 μ m observations currently provide a tracer of SFR that probes the weakest levels of obscured star formation at any given redshift over 0 < z < 3 (Elbaz et al., 2011). However, 24 μ m observations have suffered from overestimation of the L(TIR) and the SFR of up to an order of magnitude at redshift beyond $z \sim 1$. Several explanations for this overestimation were proposed, such as the presence of unidentified AGNs, intrinsic strengthening of PAH emissions, or unknown SED evolution. Empirically, some studies found low-luminosity local galaxies' SED could be used as template for high-z ULIRGs. But

the underlying cause of the SED differences were not systematically examined. Chapter 2 explained why: this is the consequence of the structural differences between local and high-z IR galaxies. The work in Chapter 2 further found $\Sigma_{\rm LIR}$ to be a universally good indicator of the IR galaxy SED. Thus in Chapter 3, I used this finding to develop a new $L({\rm TIR})$ and SFR estimator using single-band 24 μ m observations (Rujopakarn et al., 2012). The resulting indicator predicts $L({\rm TIR})$ within 0.15 dex of the values measured with far-IR photometry at 0 < z < 3 (e.g., from Herschel). This agreement indicates that our first-order understanding of the structure of star formation at high-z is consistent with the true nature of starforming galaxies, and that they are dominated by extended starbursts (> 94% by numbers, see Section 3.4.1), which, along with the results in Chapter 2, underscores the significance of secular galaxy evolution process at the peak of the galaxy evolution.

Similar formalisms to estimate $L({\rm TIR})$ from 24 $\mu{\rm m}$ observations have also been recently suggested by Elbaz et al. (2011) and Nordon et al. (2012). Along with our indicator, these results will allow exploitation of the mid-IR wavelengths for galaxy evolution studies to the fullest, especially in the era of JWST, which will provide spatially-resolved mid-IR observation of galaxies at out to $z\sim 3$ for the first time and thus will allow SFR to be probed in an unobscured manner in their substructures.

6.3 Physical properties of individual star-forming galaxies at 1 < z < 3

At 1 < z < 3, SFRs are commonly measured with rest-frame UV tracers, which could be affected by dust extinction in the U/LIRG environments. Such galaxies, whose SFRs are on the order of $10~M_{\odot}/\text{yr}$ or more, can be so obscured that less than 3% of the UV light can escape directly (Buat et al., 2007). But the extinction in

individual galaxies at these redshifts has not been explored with an independent estimator that can probe obscured regions thoroughly. In Chapter 4, I measured the intrinsic extinction in gravitationally lensed star-forming galaxies at 1 < z < 3by using near and mid-IR spectroscopy from the Large Binocular Telescope and *Spitzer* to observe their H α , P α and Br α emission (also, Papovich et al., 2009). I found the spread of extinction values of SF galaxies to be larger than previously known from optical observations (Rujopakarn et al., 2012). In most cases, the intrinsic extinction ranges from 3-6 mag, even though detailed optical line measurements indicate 1-1.5 mag. For galaxies with IR luminosities above $10^{11} L_{\odot}$, the uncorrected H α line emission no longer correlates with the intrinsic SFR. The result also indicates a large variety of dust distribution scenarios, from a uniform mixture that resembles the extinction screen assumption, to inhomogeneous mixtures. Despite the more extended structure of star formation indicated by results in Chapters 2 and 3, which would suggest lower optical depths for high-z starburst galaxies, this chapter demonstrated that extinction at high z are diverse, i.e., cannot be taken for granted to be low and simple to correct, and that the mid-IR wavelengths are among the best tools to study the intensely star-forming galaxies in these epochs.

6.4 The Evolution of Star-forming Galaxies at 0 < z < 1.2

Given the large spread of intrinsic extinction in high-z SF galaxies, mid-IR observations provide one of the most complete and unbiased views of high-z star formation. In Chapter 5 (Rujopakarn et al., 2010), I measured the SFR history out to $z\sim 1.2$ by constructing luminosity functions of SF galaxies using the *Spitzer* 24 μ m observations and spectroscopic redshifts in the 9 sq. degree Boötes field. The luminosity functions are then integrated to determine the total Cosmic IR

luminosity density, which traces the Cosmic SFR as a function of redshift.

I identified AGN in the field using the X-ray, mid-IR power-law SED shape, and optical emission line diagnostics, and found AGN fraction to be \sim 7% of galaxies. Mid-IR diagnostics of optically-selected AGN further indicate that the mid-IR emission from optically-selected AGN are dominated by star formation activity. The result from this chapter that the Cosmic SFR evolution goes by $(1+z)^{3.5\pm0.2}$ up to $z\sim1$ is supported by several recent studies. Most notably is from that of Patel et al. (2012) using 49 sq. deg Spitzer Wide-area InfraRed Extragalactic survey (SWIRE), which shows remarkable agreement. In addition, a by-product of the work in Chapter 5 is an accurate measurement of the local luminosity function and the local SFR density. These results were later confirmed by subsequent large area surveys, for example, Wu et al. (2011) and Patel et al. (2012). The small fraction of AGN and the results from Chapter 2 and 3 that indicate the lack of merger dominance and extended structure of star formation are inconsistent with the scenario of merger-triggered starburst and AGN and their roles in suppressing the Cosmic star formation. These observations, again, are supporting the secular picture that galaxies evolved in isolation and the rapid decline of the Cosmic SFR could primarily be due to the exhaustion of molecular hydrogen gas (H_2) that fuels SF.

6.5 Future Works

The use of radio interferometric observations in Chapter 2 to study the physical sizes of star-forming regions has demonstrated their power to obtain extinction-free spatially-resolved distributions of star formation in galaxies at high-z. However, the sample of 92 galaxies in the *Hubble* Deep Field from the Very Large Array (VLA) and Multi-Element Radio Linked Interferometer Network (MERLIN) used

in Chapter 2 is currently insufficient to draw general conclusions of the nature of galaxies at the peak of galaxy evolution. With the modernization of the electronics of the VLA (Perley et al., 2011), the sensitivity and bandwidth of the array have been increased by a factor of $10\times$ and $80\times$, respectively. The array, now known as the Jansky Very Large Array (JVLA), opens up many new possibilities; among them is to conduct deep galaxy surveys. The large bandwidth of JVLA allows higher frequencies to be exploited to gain resolution while maximizing sky coverage. This presents an opportunity to vastly expand the sample as the one in Chapter 2.

JVLA radio continuum observations (e.g., C band, 4-8 GHz) provide a means to distinguish the two fundamental modes of SF: (1) "in situ" galaxy assembly through disk-wide SF ("main sequence") and (2) merger-triggered starbursts, both by directly studying the SF morphology and by determining the $\Sigma_{\rm SFR}$ (see Chapter 2). Such high resolution images will further provide a foundation for other critical measurements building on this topic. They will allow selection of galaxies spanning a wide range of $\Sigma_{\rm SFR}$ and redshift to study their distributions and properties of H_2 gas to further understand the secular picture of galaxy evolution. Spatially and dynamically resolved observations of H_2 gas can be carried out through its tracer molecule, carbon-monoxide (CO), particularly the ${\rm CO}(J=1-0)$ transition at $\nu_{\rm rest}=115.2712$ GHz, which are observable by the JVLA and the Atacama Large Millimeter Array (ALMA).

Together, the spatially-resolved observations of SF and H_2 will probe the power-law dependence of surface density of SF rate on surface density of gas (SF law; e.g., Kennicutt 1998), which is critical to understanding how SF proceeds on galactic scales, and is a key assumption in simulations of galaxy evolution. Dynamically-resolved CO observations will provide a direct constraint on gas density, kinetic

temperature, and velocity maps that will allow us to study the dynamics of cold gas. Combined with the near-IR spectroscopy that probes rest-frame optical spectra, these observations have the potential to unveil a complete picture of the star formation process from cold gas to young stars for a wide range of star-forming galaxies at the peak epoch of the Cosmic SFR.

I am leading a collaboration to conduct a high-resolution 4-8 GHz radio continuum survey of a section of the UKIDSS Deep Survey (UDS) field using the JVLA. The region was selected to overlap deep treasury surveys from *Spitzer* at 24 μ m, *Hubble* imaging in near-IR, and *Hubble* near-IR grism spectroscopy, along with multiwavelength ancillary data. The JVLA observations will start in the Fall 2012.

APPENDIX A

ESTIMATION OF PHYSICAL SIZES FOR LOCAL IR GALAXIES

Our local sample of star-forming galaxies was selected to represent a broad range of IR luminosities from normal star-forming galaxy ($L(\text{TIR}) \leq 10^{11} L_{\odot}$), luminous IR galaxy (LIRG, $10^{11} \leq L(\text{TIR}) \leq 10^{12} L_{\odot}$), to ultraluminous IR galaxy (ULIRG, $L(\text{TIR}) \geq 10^{12} L_{\odot}$). Here we discuss how we select the local starburst galaxies and the methods we employ to estimate the physical sizes to compare with high-redshift star-forming galaxies in the same metric. For all but three local galaxies, L(TIR) was obtained from the IRAS Revised Bright Galaxy Sample (RBGS; Sanders et al., 2003). The RBGS provides L(TIR) that has a definition similar to that of L(TIR) from the Rieke et al. (2009) formalism used for our intermediate and high redshift compilation. The three exceptions are discussed separately.

A.1 Normal Star-Forming Galaxies

Galaxies from the *Spitzer* Infrared Nearby Galaxies Survey (e.g., Kennicutt et al., 2003; Calzetti et al., 2007) are used to represent normal star-forming galaxies. SINGS galaxies are selected from within the local volume to allow IR imaging at reasonably good physical resolution. We use the 24 μ m images of these galaxies to map star formation. We only select high-luminosity galaxies. As noted by Calzetti et al. (2007), NGC 4125 and NGC 5195 contain Seyfert 2 nuclei and thus are excluded from our compilation. L(TIR) for the other galaxies was taken from the RBGS except for NGC 1512, NGC 2841, and NGC 4625 that are not in the catalog. For these three galaxies we use 24 μ m fluxes from Dale et al. (2007) to estimate L(TIR) using the appropriate Rieke et al. (2009) SED.

We convolved the SINGS 24 μ m MIPS images with a series of Gaussians that

have angular FWHM corresponding to physical sizes ranging over 1-8 kpc at the galaxy's distance and then fit 2D Gaussians to estimate a deconvolved size from the convolved images. We found that the recovered FWHM is a slowly varying function of the convolved Gaussian's FWHM, which assures that sizes estimated from this method are robust. For the actual size measurement for these galaxies we convolve all SINGS 24 μ m imaging with a Gaussian that has FWHM corresponding to 4 kpc at each galaxy's distance and measure deconvolved sizes from the convolved image. This procedure is illustrated by NGC 3627 in Fig. 2.1. These sizes are reported in Table A.1 for normal star-forming galaxies.

We have 19 galaxies from the SINGS sample with L(TIR) in the range of $10^{8.6}$ – $10^{10.6} L_{\odot}$, a median L(TIR) of $10^{9.8} L_{\odot}$, and a median physical diameter of 3.5 kpc.

A.2 LIRGs

Our local LIRGs were drawn from Condon et al. (1991), Alonso-Herrero et al. (2006), and Iono et al. (2009). Their size measurements are based on the 8.4 GHz VLA radio observations, Pa α imaging using *Hubble* Space Telescope (HST), and Submillimeter Array (SMA) submillimeter observations, respectively.

Condon et al. (1991) observed 40 LIRGs selected from the *IRAS* Bright Galaxy Sample using the VLA with a resolution of 0″25. From these 40 LIRGs, 15 are dominated by a compact radio component likely to be an AGN, referred to by Condon et al. (1991) as "monsters" and another 5 are known to harbor AGN according to SIMBAD, which we exclude; 6 are multi-component with one or more components not reported, which we exclude; 2 are multi-component with well constrained sizes for both components (NGC 3690, which is Arp 299 for which we adopt CO size measurement from Iono et al. (2009), and IRAS F15163+4255); one has an observational issue (NGC 1614) but it was also observed by Iono et al.

(2009) and therefore we adopt the Iono et al. (2009) size measurement for NGC 1614; there are size measurements for only four galaxies of the remaining 11. These four are UGC 2369, IRAS F03359+1523, UGC 4881, and IRAS F17132+5313. Along with the aforementioned IRAS F15163+4255, a multi-component object with well-measured size, we have five LIRGs from Condon et al. (1991).

The Alonso-Herrero et al. (2006) LIRGs were selected such that their $Pa\alpha$ emission line would fall in the narrow band of the F190N filter of the Near Infrared Camera and Multi-Object Spectrometer (NICMOS) on HST. The resolution of NICMOS (0'.076/pixel) resolved detailed structures of these LIRGs and thus we need to measure their sizes using the same procedure as in \S A.1. However, we convolved the images using Gaussians with FWHMs corresponding to only 1 kpc at each LIRG's distance. This was necessary because of the intrinsically smaller sizes of the LIRGs, which we also tested by measuring the diameter encircling 90% of flux. The results from our measurements are given in the LIRGs section of Table A.1.

Iono et al. (2009) report sizes of LIRGs within 200 Mpc using the SMA, based on CO (3 - 2) observations by Wilson et al. (2008). The sample contains LIRGs harboring AGN (including NGC 2623, NGC 6240, UGC 5101, Mrk 231, Mrk 273, IRAS F10565+2448 and IRAS F17207-0014) and multicomponent objects where the sizes of some components cannot be determined (including Arp 55, Arp 299, NGC 5331, and NGC 5257/8) and thus we are left with four starburst-dominated objects with good size estimates. They are Arp 193, VV 114, NGC 1614, and IRAS 10565.

In total we have 21 LIRGs with median L(TIR) of $10^{11.5}$ L_{\odot} and a median physical diameter of 0.8 kpc. This sample is dominated by the 12 galaxies with $Pa\alpha$ images, and these galaxies by themselves should provide an unbiased esti-

mate of sizes of the star forming regions in LIRGs. The estimated sizes of the galaxies measured in the radio and in CO are consistent with those from Pa α .

A.3 ULIRGs

Despite the many local ULIRGs, selecting a sample to study the physical sizes of the starburst regions is complicated by two issues. First, a majority of these ULIRGs harbor AGN and thus do not represent a starburst environment. Second, the sizes of the IR-emitting regions are significantly smaller than the optical and near-IR extents of these galaxies and the existing mid-IR data in the literature (e.g. SINGS) do not resolve the ULIRGs' IR emission. Our compilation therefore relies on radio and submillimeter interferometric observations of four ULIRGs that are known to have their IR luminosity dominated by star-forming emission: VII Zw 31, IRAS F23365+3604, Arp 220, and IRAS F17207-0014. Their IR luminosities according to Sanders et al. (2003) are in the range of $10^{12.00} - 10^{12.45} L_{\odot}$.

Arp 220 has two nuclei \sim 370 pc apart; the western nucleus is slightly more luminous than the eastern nucleus (Rovilos et al., 2003). This galaxy was studied with Very Long Baseline Interferometry (VLBI) at 18 cm by Smith et al. (1998) who found the western nucleus to contain most of the individual 18 cm sources (13 sources in the western nucleus vs. three in the eastern nucleus). They report that the sources in the western nucleus are confined within 75 pc \times 150 pc. Circularizing these values gives a diameter of 0.1 kpc for the western nucleus alone. The 1.6 and 5 GHz MERLIN radio maps by Rovilos et al. (2003) indicate both nuclei have similar physical sizes. We estimate the physical size of Arp 220 from the 5 GHz map where the two nuclei are clearly separated. Combining the emission regions from both nuclei, we adopt an effective diameter of 0.2 kpc for the starburst region of Arp 220.

The sizes of VII Zw 31 and IRAS F23365+3604 are reported by Downes & Solomon (1998) based on CO (1 - 0) observations; the IRAS F17207-0014 size by Iono et al. (2009) is based on CO (3 - 2) observations. Again, we treat these CO-derived sizes as upper limits for the size of the IR-emitting extent of the galaxy.

Table A.1. Local Compilation of Star-Forming Galaxies

Source	IRAS ID	Distance ^a	$L(TIR)^{a}$	Diameter	References ^b
		(Mpc)	$(log L_{\odot})$	(kpc)	
Normal SF Galaxies					
NGC 2976	F09431+6809	3.8	8.61	1.5	1
NGC 4826	F12542+2157	6.0	9.14	1.2	1
NGC 2403	F07320+6543	3.8	9.25	3.0	1
NGC 925	F02242+3321	9.8	9.46	6.1	1
NGC 1512		11.3	9.49	3.2	1
NGC 5866	F15051+5557	13.0	9.51	1.8	1
NGC 2841		10.5	9.52	4.9	1
NGC 4559	F12334+2814	11.9	9.62	5.0	1
NGC 4736	12485+4123	5.7	9.79	1.7	1
NGC 3198	F10168+4547	14.7	9.81	3.8	1
NGC 3184	10152+4140	11.9	9.86	6.5	1
NGC 3351	F10413+1157	10.8	9.89	2.2	1
NGC 3938	F11502+4423	13.1	9.99	4.7	1
NGC 4569	F12343+1326	17.8	10.08	3.1	1
NGC 5055	F13135+4217	8.4	10.15	4.3	1
NGC 5033	F13111+3651	14.7	10.19	1.1	1
NGC 3627	F11176+1315	9.3	10.44	3.5	1
NGC 5194	F13277+4727	8.8	10.48	5.7	1

Table A.1 (cont'd)

Source	IRAS ID	Distance ^a	$L(TIR)^{a}$	Diameter	References ^b
		(Mpc)	$(log L_{\odot})$	(kpc)	
NGC 7331	F22347+3409	16.2	10.64	4.7	1
LIRGs					
NGC 23	F00073+2538	63.9	11.11	1.2	2
NGC 6701	F18425+6036	60.6	11.11	0.7	2
UGC 1845	F02208+4744	66.4	11.13	0.81	2
NGC 5936	F15276+1309	65.1	11.13	0.56	2
MCG +02-20-003	F07329+1149	72.4	11.14	0.78	2
NGC 2369	F07160-6215	47.1	11.16	0.82	2
ESO 320-G030	F11506-3851	40.4	11.16	0.91	2
IC 5179	F22132-3705	50.0	11.22	1.6	2
NGC 2388	F07256+3355	61.9	11.29	0.84	2
NGC 7771	F23488+1949	61.2	11.40	1.04	2
MCG +12-02-001	F00506+7248	68.9	11.50	0.8	2
	F03359+1523	146.9	11.53	0.07	3
NGC 1614	F04315-0840	67.1	11.66	0.9	4
UGC 2369	F02512+1446	130.7	11.66	0.08	3
Arp 236	F01053-1746	84.2	11.71	2.6	4
Arp 193	F13182+3424	107.1	11.73	0.8	4
UGC 4881	F09126+4432	172.7	11.75	0.14	3

Table A.1 (cont'd)

Source	IRAS ID	Distance ^a	$L(\mathrm{TIR})^{\mathrm{a}}$	Diameter	References ^b
		(Mpc)	$(log L_{\odot})$	(kpc)	
Arp 299	F11257+5850	51.2	11.94	0.42	4
	F17132+5313	218.9	11.95	0.14	3
•••	F15163+4255	180.8	11.95	0.22	3
	F10565+2448	188.9	11.99	0.8	4
ULIRGs					
VII Zw 31	F05081+7936	230.2	12.00	2.1	5
•••	F23365+3604	269.8	12.19	1.1	5
Arp 220	F15327+2340	85.6	12.27	0.2	6
	F17207-0014	188.2	12.45	< 0.9	4

 $^{\rm a}{\rm Distance}$ and $L({\rm TIR})$ from Sanders et al. (2003) and adjust to match our cosmology.

^bDiameters references 1. measured from *Spitzer* MIPS 24 μ m imaging taken by SINGS (Kennicutt et al., 2003; Calzetti et al., 2007, e.g.,), 2. measured from *Hubble* NICMOS Pa- α taken by Alonso-Herrero et al. (2006), 3. 8.4 GHz radio sizes given by Condon et al. (1991), 4. CO (3 – 2) sizes given by Iono et al. (2009), 5. CO (2 – 1) or CO (1 – 0) sizes given by Downes & Solomon (1998), 6. 5 GHz radio size based on Rovilos et al. (2003).

REFERENCES

Afonso, J., Hopkins, A., Mobasher, B., & Almeida, C. 2003, ApJ, 597, 269

Agertz, O., Teyssier, R., & Moore, B. 2009, MNRAS, 397, L64

Allam, S. S., Tucker, D. L., Lin, H., et al. 2007, ApJL, 662, L51

Alonso-Herrero, A., Rieke, G. H., Rieke, M. J., Colina, L., Pérez-González, P. G., & Ryder, S. D. 2006, ApJ, 650, 835

Armus, L., et al. 2007, ApJ, 656, 148

Ashby, M. L. N., et al. 2009, ApJ, 701, 428

Bai, L., Marcillac, D., Rieke, G. H., et al. 2007, ApJ, 664, 181

Baldwin, J. A., Phillips, M. M., & Terlevich, R. 1981, PASP, 93, 5

Barmby, P., et al. 2006, ApJ, 642, 126

Barro, G., Pérez-González, P. G., Gallego, J., et al. 2011, ApJS, 193, 30

Bavouzet, N., Dole, H., Le Floc'h, E., Caputi, K. I., Lagache, G., & Kochanek, C. S. 2008, A&A, 479, 83

Becker, G. D., Rauch, M., & Sargent, W. L. W. 2009, ApJ, 698, 1010

Berta, S., Magnelli, B., Nordon, R., et al. 2011, A&A, 532, A49

Bertin, E., & Arnouts, S. 1996, A&AS, 117, 393

Bian, F., Fan, X., Bechtold, J., et al. 2010, ApJ, 725, 1877

Biggs, A. D., & Ivison, R. J. 2008, MNRAS, 385, 893

Blain, A. W., Smail, I., Ivison, R. J., Kneib, J.-P., & Frayer, D. T. 2002, Phys. Rep., 369, 111

Blanton, M. R., & Roweis, S. 2007, AJ, 133, 734

Bothwell, M. S., et al. 2010, MNRAS, 525

Bouché, N., Lehnert, M. D., Aguirre, A., Péroux, C., & Bergeron, J. 2007, MNRAS, 378, 525

Bourne, N., Dunne, L., Ivison, R. J., Maddox, S. J., Dickinson, M., & Frayer, D. T. 2011, MNRAS, 410, 1155

Brand, K., et al. 2006, ApJ, 641, 140

Brand, K., et al. 2009, ApJ, 693, 340

Brandl, B. R., et al. 2006, ApJ, 653, 1129

Brown, M. J. I., Dey, A., Jannuzi, B. T., Brand, K., Benson, A. J., Brodwin, M., Croton, D. J., & Eisenhardt, P. R. 2007, ApJ, 654, 858

Buat, V., Donas, J., Milliard, B., & Xu, C. 1999, A&A, 352, 371

Buat, V., Iglesias-Páramo, J., Seibert, M., et al. 2005, ApJL, 619, L51

Buat, V., et al. 2007, ApJS, 173, 404

Calzetti, D., et al. 2007, ApJ, 666, 870

Calzetti, D., et al. 2010, ApJ, 714, 1256

Calzetti, D. 2010, arXiv:1010.4996

Caputi, K. I., et al. 2007, ApJ, 660, 97

Cardamone, C. N., et al. 2008, ApJ, 680, 130

Carilli, C. L., et al. 2010, ApJ, 714, 1407

Casey, C. M., et al. 2009, MNRAS, 399, 121

Chakrabarti, S., & McKee, C. F. 2005, ApJ, 631, 792

Chanial, P., Flores, H., Guiderdoni, B., Elbaz, D., Hammer, F., & Vigroux, L. 2007, A&A, 462, 81

Chapman, S. C., Smail, I., Windhorst, R., Muxlow, T., & Ivison, R. J. 2004, ApJ, 611, 732

Chapman, S. C., Blain, A. W., Smail, I., & Ivison, R. J. 2005, ApJ, 622, 772

Chary, R., & Elbaz, D. 2001, ApJ, 556, 562

Chary, R.-R., & Pope, A. 2010, arXiv:1003.1731

Chary, R.-R. 2006, ArXiv Astrophysics e-prints, arXiv:astro-ph/0612736

Choi, P. I., Yan, L., Im, M., et al. 2006, ApJ, 637, 227

Coppin, K., et al. 2006, MNRAS, 372, 1621

Condon, J. J. 1974, ApJ, 188, 279

Condon, J. J., & Dressel, L. L. 1978, ApJ, 221, 456

Condon, J. J., Huang, Z.-P., Yin, Q. F., & Thuan, T. X. 1991, ApJ, 378, 65

Condon, J. J., Cotton, W. D., Greisen, E. W., Yin, Q. F., Perley, R. A., Taylor, G. B., & Broderick, J. J. 1998, AJ, 115, 1693

Cooper, M. C., Yan, R., Dickinson, M., et al. 2011, arXiv:1112.0312

Croton, D. J., Springel, V., White, S. D. M., et al. 2006, MNRAS, 365, 11

Dai, X., et al. 2009, ApJ, 697, 506

Daddi, E., et al. 2010, ApJ, 713, 686

Daddi, E., et al. 2010, ApJL, 714, 118

Dale, D. A., Helou, G., Contursi, A., Silbermann, N. A., & Kolhatkar, S. 2001, ApJ, 549, 215

Dale, D. A. & Helou, G. 2002, ApJ, 576, 159

Dale, D. A., et al. 2006, ApJ, 646, 161

Dale, D. A., et al. 2007, ApJ, 655, 863

Damen, M., Labbé, I., van Dokkum, P. G., et al. 2011, ApJ, 727, 1

Dasyra, K. M., et al. 2009, ApJ, 701, 1123

Davé, R., Finlator, K., Oppenheimer, B. D., Fardal, M., Katz, N., Kereš, D., & Weinberg, D. H. 2010, MNRAS, 404, 1355

de Jong, T., Clegg, P. E., Rowan-Robinson, M., et al. 1984, ApJL, 278, L67

Dessauges-Zavadsky, M., Christensen, L., D'Odorico, S., Schaerer, D., & Richard, J. 2011, A&A, 533, A15

Diamond-Stanic, A. M., & Rieke, G. H. 2010, ApJ, 724, 140

Diolaiti, E., Bendinelli, O., Bonaccini, D., et al. 2000, A&AS, 147, 335

Dole, H., et al. 2004, ApJS, 154, 87

Dole, H., et al. 2004, ApJS, 154, 93

Dole, H., et al. 2006, A&A, 451, 417

Donley, J. L., Rieke, G. H., Pérez-González, P. G., Rigby, J. R., & Alonso-Herrero, A. 2007, ApJ, 660, 167

Donley, J. L., Rieke, G. H., Pérez-González, P. G., & Barro, G. 2008, ApJ, 687, 111

Downes, D., & Solomon, P. M. 1998, ApJ, 507, 615

Egami, E., et al. 2010, A&A, 518, L12

Eisenhardt, P. R., et al. 2004, ApJS, 154, 48

Elbaz, D., et al. 1999, A&A, 351, L37

Elbaz, D., Cesarsky, C. J., Chanial, P., Aussel, H., Franceschini, A., Fadda, D., & Chary, R. R. 2002, A&A, 384, 848

Elbaz, D., et al. 2007, A&A, 468, 33

Elbaz, D., et al. 2010, A&A, 518, L29

Elbaz, D., et al. 2011, arXiv:1105.2537

Elvis, M., et al. 1994, ApJS, 95, 1

Engelbracht, C. W., Blaylock, M., Su, K. Y. L., et al. 2007, PASP, 119, 994

Engelbracht, C. W., Rieke, G. H., Gordon, K. D., Smith, J.-D. T., Werner, M. W., Moustakas, J., Willmer, C. N. A., & Vanzi, L. 2008, ApJ, 678, 804

Erb, D. K., Shapley, A. E., Pettini, M., Steidel, C. C., Reddy, N. A., & Adelberger,K. L. 2006, ApJ, 644, 813

Fabricant, D. et al. 2005, PASP, 117, 1411

Fadely, R., Allam, S. S., Baker, A. J., et al. 2010, ApJ, 723, 729

Fan, X. 2006, New Astronomy Reviews, 50, 665

Farrah, D., et al. 2008, ApJ, 677, 957

Ferguson, H. C., Dickinson, M., & Williams, R. 2000, ARA&A, 38, 667

Finkelstein, S. L., Papovich, C., Rudnick, G., et al. 2009, ApJ, 700, 376

Finkelstein, K. D., Papovich, C., Finkelstein, S. L., et al. 2011, arXiv:1110.3323

Franceschini, A., Aussel, H., Cesarsky, C. J., Elbaz, D., & Fadda, D. 2001, A&A, 378, 1

Frayer, D. T., Sanders, D. B., Surace, J. A., et al. 2009, AJ, 138, 1261

Gallego, J., Zamorano, J., Aragon-Salamanca, A., & Rego, M. 1995, ApJL, 455, L1

Gao, Y., & Solomon, P. M. 2004, ApJ, 606, 271

Genzel, R., et al. 1998, ApJ, 498, 579

Genzel, R., et al. 2010, MNRAS, 407, 2091

Giavalisco, M., et al. 2004, ApJL, 600, L93

Gladders, M. D., Rigby, J. R., Sharon, K., et al. 2012, arXiv:1202.5269

Gordon, K., et al. 2005, PASP, 117, 503

Gorjian, V., et al. 2008, ApJ, 679, 1040

Greve, T. R., Ivison, R. J., & Papadopoulos, P. P. 2003, ApJ, 599, 839

Greve, T. R., Ivison, R. J., Bertoldi, F., Stevens, J. A., Dunlop, J. S., Lutz, D., & Carilli, C. L. 2004, MNRAS, 354, 779

Hacking, P., & Houck, J. R. 1987, ApJS, 63, 311

Hailey-Dunsheath, S., Nikola, T., Stacey, G. J., Oberst, T. E., Parshley, S. C., Benford, D. J., Staguhn, J. G., & Tucker, C. E. 2010, ApJL, 714, L162

Hainline, L. J., Blain, A. W., Smail, I., Frayer, D. T., Chapman, S. C., Ivison, R. J.,& Alexander, D. M. 2009, ApJ, 699, 1610

Hainline, K. N., Shapley, A. E., Kornei, K. A., et al. 2009, ApJ, 701, 52

Hacking, P., Houck, J. R., & Condon, J. J. 1987, ApJL, 316, L15

Hanish, D. J., et al. 2006, ApJ, 649, 150

Hewett, P. C., Foltz, C. B., & Chaffee, F. H. 1993, ApJL, 406, L43

Hickox, R. C., et al. 2009, ApJ, 696, 891

Hogg, D. W., & Turner, E. L. 1998, PASP, 110, 727

Hollenbach, D. J., & Tielens, A. G. G. M. 1999, Reviews of Modern Physics, 71, 173

Hopkins, A. M. 2004, ApJ, 615, 209

Hopkins, P. F., Hernquist, L., Cox, T. J., et al. 2006, ApJS, 163, 1

Hopkins, A. M., & Beacom, J. F. 2006, ApJ, 651, 142

Hopkins, P. F., Younger, J. D., Hayward, C. C., Narayanan, D., & Hernquist, L. 2010, MNRAS, 402, 1693

Houck, J. R., et al. 2005, ApJL, 622, L105

Huchra, J. & Sargent, W. L. W. 1973, ApJ, 186, 433

Iono, D., et al. 2009, ApJ, 695, 1537

Ivezić, Ž., et al. 2002, AJ, 124, 2364

Ivison, R. J., et al. 2007, MNRAS, 380, 199

Ivison, R. J., et al. 2010a, MNRAS, 402, 245

Ivison, R. J., et al. 2010b, arXiv:1005.1072

Ivison, R. J., et al. 2010c, arXiv:1005.1071

Ivison, R. J., Smail, I., Amblard, A., et al. 2012, arXiv:1206.4046

Jannuzi, B. T., & Dey, A. 1999, Photometric Redshifts and the Detection of High Redshift Galaxies, 191, 111

Johansson, D., et al. 2010, A&A, 514, A77

Juneau, S., Narayanan, D. T., Moustakas, J., Shirley, Y. L., Bussmann, R. S., Kennicutt, R. C., & Vanden Bout, P. A. 2009, ApJ, 707, 1217

Kartaltepe, J. S., et al. 2010, ApJ, 709, 572

Kartaltepe, J. S., et al. 2010, ApJ, 721, 98

Kauffmann, G., et al. 2003, MNRAS, 346, 1055

Kennicutt, R. C. 1998, ARA&A, 36, 189

Kennicutt, R. C., Jr. 1998, ApJ, 498, 541

Kennicutt, R. C., Jr., et al. 2003, PASP, 115, 928

Kennicutt, R. C., et al. 2009, ApJ, 703, 1672

Kennicutt, R. C., Calzetti, D., Aniano, G., et al. 2011, PASP, 123, 1347

Kewley, L. J., Dopita, M. A., Sutherland, R. S., Heisler, C. A., & Trevena, J. 2001, ApJ, 556, 121

Kewley, L. J., Groves, B., Kauffmann, G., & Heckman, T. 2006, MNRAS, 372, 961

Kleinmann, D. E., & Low, F. J. 1970, ApJL, 159, L165

Kneib, J.-P., Ellis, R. S., Smail, I., Couch, W. J., & Sharples, R. M. 1996, ApJ, 471, 643

Kneib, J.-P., van der Werf, P. P., Kraiberg Knudsen, K., et al. 2004, MNRAS, 349, 1211

Kobayashi, C., Springel, V., & White, S. D. M. 2007, MNRAS, 376, 1465

Kocevski, D. D., Lemaux, B. C., Lubin, L. M., et al. 2011, ApJ, 736, 38

Kroupa, P. 2002, Science, 295, 82

Lacy, M., et al. 2004, ApJS, 154, 166

Lagache, G., Dole, H., & Puget, J.-L. 2003, MNRAS, 338, 555

Lagache, G., et al. 2004, ApJS, 154, 112

Lagache, G., Puget, J.-L., & Dole, H. 2005, ARA&A, 43, 727

Lee, N., et al. 2010, ApJ, 717, 175

Le Floc'h, E., et al. 2005, ApJ, 632, 169

LeFloc'h, E., et al. 2009, ApJ, 703, 222

Lehmer, B. D., Brandt, W. N., Alexander, D. M., et al. 2005, ApJS, 161, 21

Lehnert, M. D., Nesvadba, N. P. H., Tiran, L. L., Matteo, P. D., van Driel, W., Douglas, L. S., Chemin, L., & Bournaud, F. 2009, ApJ, 699, 1660

Lin, H., Buckley-Geer, E., Allam, S. S., et al. 2009, ApJ, 699, 1242

Leitherer, C., et al. 1999, ApJS, 123, 3

Lilly, S. J., Le Fevre, O., Hammer, F., & Crampton, D. 1996, ApJL, 460, L1

Lilly, S. J., et al. 2007, ApJS, 172, 70

Lotz, J. M., et al. 2008, ApJ, 672, 177

Low, J., & Kleinmann, D. E. 1968, AJ, 73, 868

Madau, P., Ferguson, H. C., Dickinson, M. E., Giavalisco, M., Steidel, C. C., & Fruchter, A. 1996, MNRAS, 283, 1388

Magnelli, B., Elbaz, D., Chary, R. R., Dickinson, M., Le Borgne, D., Frayer, D. T., & Willmer, C. N. A. 2009, A&A, 496, 57

Magnelli, B., Elbaz, D., Chary, R. R., et al. 2011, A&A, 528, A35

Mandel, H., Seifert, W., Lenzen, R., et al. 2007, Astronomische Nachrichten, 328, 626

Marcillac, D., Elbaz, D., Chary, R. R., Dickinson, M., Galliano, F., & Morrison, G. 2006, A&A, 451, 57

Martin, C., et al. 2003, Proc. SPIE, 4854, 336

Marleau, F. R., et al. 2004, ApJS, 154, 66

Marleau, F. R., Fadda, D., Appleton, P. N., Noriega-Crespo, A., Im, M., & Clancy, D. 2007, ApJ, 663, 218

Marshall, H. L., Tananbaum, H., Avni, Y., & Zamorani, G. 1983, ApJ, 269, 35

McKee, C. F., & Ostriker, J. P. 1977, ApJ, 218, 148

Menéndez-Delmestre, K., et al. 2009, ApJ, 699, 667

Momjian, E., Romney, J. D., Carilli, C. L., & Troland, T. H. 2006, ApJ, 653, 1172

Morrison, G. E., Owen, F. N., Dickinson, M., Ivison, R. J., & Ibar, E. 2010, ApJS, 188, 178

Moorwood, A. F. M. 1986, A&A, 166, 4

Moustakas, J., Kennicutt, R. C., Jr., & Tremonti, C. A. 2006, ApJ, 642, 775

Moustakas, J., Kennicutt, R. C., Jr., Tremonti, C. A., Dale, D. A., Smith, J.-D. T., & Calzetti, D. 2010, ApJS, 190, 233

Murphy, E. J., et al. 2006, ApJ, 638, 157

Murray, S. S., et al. 2005, ApJS, 161, 1

Muxlow, T. W. B., et al. 2005, MNRAS, 358, 1159

Muzzin, A., van Dokkum, P., Kriek, M., Labbé, I., Cury, I., Marchesini, D., & Franx, M. 2010, ApJ, 725, 7

Narayanan, D., Cox, T. J., Hayward, C., & Hernquist, L. 2010, arXiv:1005.3020

Nelson, E. J., van Dokkum, P. G., Brammer, G., et al. 2012, ApJL, 747, L28

Neri, R., et al. 2003, ApJL, 597, L113

Nesvadba, N. P. H., Lehnert, M. D., Genzel, R., et al. 2007, ApJ, 657, 725

Neugebauer, G., Becklin, E. E., Oke, J. B., & Searle, L. 1976, ApJ, 205, 29

Neugebauer, G., Becklin, E. E., Oke, J. B., & Searle, L. 1976, ApJ, 205, 29

Neugebauer, G., Oke, J. B., Becklin, E. E., & Matthews, K. 1979, ApJ, 230, 79

Niemi, S.-M., Somerville, R. S., Ferguson, H. C., et al. 2012, MNRAS, 421, 1539

Noeske, K. G., et al. 2007, ApJL, 660, L47

Nordon, R., et al. 2010, A&A, 518, L24

Nordon, R., Lutz, D., Genzel, R., et al. 2012, ApJ, 745, 182

Osterbrock, D. E., & Ferland, G. J. 2006, Astrophysics of gaseous nebulae and active galactic nuclei, 2nd. ed. by D.E. Osterbrock and G.J. Ferland. Sausalito, CA: University Science Books, 2006,

Papovich, C., et al. 2004, ApJS, 154, 70

Papovich, C., et al. 2006, AJ, 132, 231

Papovich, C., et al. 2007, ApJ, 668, 45

Papovich, C., Rudnick, G., Rigby, J. R., et al. 2009, ApJ, 704, 1506

Patel, H., Clements, D. L., Vaccari, M., et al. 2012, arXiv:1205.5690

Peebles, P. 1980, The Large-Scale Structure of the Universe (Princeton University Press)

Pérez-González, P. G., et al. 2005, ApJ, 630, 82

Pérez-González, P. G., Rieke, G. H., Villar, V., et al. 2008, ApJ, 675, 234

Perley, R. A., Chandler, C. J., Butler, B. J., & Wrobel, J. M. 2011, ApJL, 739, L1

Pettini, M., & Pagel, B. E. J. 2004, MNRAS, 348, L59

Pope, A., et al. 2006, MNRAS, 370, 1185

Pope, A., Chary, R.-R., Alexander, D. M., et al. 2008, ApJ, 675, 1171

Pozzi, F., et al. 2004, ApJ, 609, 122

Quintero, A. D., Hogg, D. W., Blanton, M. R., et al. 2004, ApJ, 602, 190

Reddy, N. A., Steidel, C. C., Pettini, M., Adelberger, K. L., Shapley, A. E., Erb, D. K., & Dickinson, M. 2008, ApJS, 175, 48

Reddy, N. A., Erb, D. K., Pettini, M., Steidel, C. C., & Shapley, A. E. 2010, ApJ, 712, 1070

Rees, M. J., Silk, J. I., Werner, M. W., & Wickramasinghe, N. C. 1969, Nature, 223, 788

Rex, M., et al. 2010, A&A, 518, L13

Richard, J., Jones, T., Ellis, R., et al. 2011, MNRAS, 413, 643

Rieke, G. H., & Low, F. J. 1972, ApJL, 176, L95

Rieke, G. H., & Low, F. J. 1975, ApJL, 200, L67

Rieke, G. H., & Lebofsky, M. J. 1978, ApJL, 220, L37

Rieke, G. H. 1978, ApJ, 226, 550

Rieke, G. H., & Lebofsky, M. J. 1981, ApJ, 250, 87

Rieke, G. H., & Lebofsky, M. J. 1985, ApJ, 288, 618

Rieke, G. H., & Lebofsky, M. J. 1986, ApJ, 304, 326

Rieke, G. H., et al. 2004, ApJS, 154, 25

Rieke, G. H., Alonso-Herrero, A., Weiner, B. J., Pérez-González, P. G., Blaylock, M., Donley, J. L., & Marcillac, D. 2009, ApJ, 692, 556

Rigby, J. R., et al. 2008, ApJ, 675, 262

Rigopoulou, D., Spoon, H. W. W., Genzel, R., Lutz, D., Moorwood, A. F. M., & Tran, Q. D. 1999, AJ, 118, 2625

Roche, P. F., Aitken, D. K., Smith, C. H., & Ward, M. J. 1991, MNRAS, 248, 606

Rodighiero, G., et al. 2010, A&A, 515, A8

Roussel, H., Sauvage, M., Vigroux, L., & Bosma, A. 2001, A&A, 372, 427

Rovilos, E., Diamond, P. J., Lonsdale, C. J., Lonsdale, C. J., & Smith, H. E. 2003, MNRAS, 342, 373

Rowan-Robinson, M., et al. 1997, MNRAS, 289, 490

Rujopakarn, W., Eisenstein, D. J., Rieke, G. H., et al. 2010, ApJ, 718, 1171

Rujopakarn, W., Rieke, G. H., Eisenstein, D. J., & Juneau, S. 2011, ApJ, 726, 93

Rujopakarn, W., Rieke, G. H., Papovich, C. J., et al. 2012, ApJ, 755, 168

Rujopakarn, W., Rieke, G. H., Weiner, B. J., et al. 2012, arXiv:1107.2921

Rush, B., Malkan, M. A., & Spinoglio, L. 1993, ApJS, 89, 1

Salim, S., et al. 2007, ApJS, 173, 267

Salpeter, E. E. 1955, ApJ, 121, 161

Sand, D. J., Treu, T., Ellis, R. S., & Smith, G. P. 2005, ApJ, 627, 32

Sandage, A., Tammann, G. A., & Yahil, A. 1979, ApJ, 232, 352

Sanders, D. B., & Mirabel, I. F. 1996, ARA&A, 34, 749

Sanders, D. B., Mazzarella, J. M., Kim, D.-C., Surace, J. A., & Soifer, B. T. 2003, AJ, 126, 1607

Sanders, D. B., et al. 2007, ApJS, 172, 86

Sargent, M. T., et al. 2010, ApJL, 714, L190

Saunders, W., Rowan-Robinson, M., Lawrence, A., Efstathiou, G., Kaiser, N., Ellis, R. S., & Frenk, C. S. 1990, MNRAS, 242, 318

Schechter, P. 1976, ApJ, 203, 297

Schiminovich, D., et al. 2005, ApJL, 619, L47

Schmidt, M. 1959, ApJ, 129, 243

Schmidt, M., Schneider, D. P., & Gunn, J. E. 1995, AJ, 110, 68

Scott, S. E., et al. 2002, MNRAS, 331, 817

Scoville, N., et al. 2007, ApJS, 172, 1

Schlegel, D. J., Finkbeiner, D. P., & Davis, M. 1998, ApJ, 500, 525

Schmidt, M. 1968, ApJ, 151, 393

Schmitt, H. R., Calzetti, D., Armus, L., Giavalisco, M., Heckman, T. M., Kennicutt, R. C., Jr., Leitherer, C., & Meurer, G. R. 2006, ApJ, 643, 173

Seitz, S., Saglia, R. P., Bender, R., et al. 1998, MNRAS, 298, 945

Seymour, N., et al. 2008, ApJL, 681, L1

Shi, Y., et al. 2007, ApJ, 669, 841

Shi, Y., Rieke, G., Lotz, J., & Perez-Gonzalez, P. G. 2009, ApJ, 697, 1764

Shupe, D. L., Fang, F., Hacking, P. B., & Huchra, J. P. 1998, ApJ, 501, 597

Siana, B., Teplitz, H. I., Chary, R.-R., Colbert, J., & Frayer, D. T. 2008, ApJ, 689, 59

Siebenmorgen, R., & Krügel, E. 2007, A&A, 461, 445

Smail, I., Smith, G. P., & Ivison, R. J. 2005, ApJ, 631, 121

Smith, H. E., Lonsdale, C. J., Lonsdale, C. J., & Diamond, P. J. 1998, ApJL, 493, L17

Smith, J. D. T., et al. 2007, ApJ, 656, 770

Smolčić, V., et al. 2009, ApJ, 690, 610

Soifer, B. T., Sanders, D. B., Madore, B. F., Neugebauer, G., Danielson, G. E., Elias, J. H., Lonsdale, C. J., & Rice, W. L. 1987, ApJ, 320, 238

Soifer, B. T., Boehmer, L., Neugebauer, G., & Sanders, D. B. 1989, AJ, 98, 766

Soifer, B. T., & Neugebauer, G. 1991, AJ, 101, 354

Steidel, C. C., Adelberger, K. L., Giavalisco, M., Dickinson, M., & Pettini, M. 1999, ApJ, 519, 1

Stern, D., et al. 2005, ApJ, 631, 163

Stetson, P. B. 1987, PASP, 99, 191

Swinbank, A. M., Smail, I., Chapman, S. C., et al. 2010, MNRAS, 405, 234

Swinbank, A. M., et al. 2010b, Nature, 464, 733

Symeonidis, M., Page, M. J., Seymour, N., Dwelly, T., Coppin, K., McHardy, I., Rieke, G. H., & Huynh, M. 2009, MNRAS, 397, 1728

Tacconi, L. J., et al. 2006, ApJ, 640, 228

Tacconi, L. J., et al. 2008, ApJ, 680, 246

Tacconi, L. J., et al. 2010, Nature, 463, 781

Takagi, T., et al. 2010, A&A, 514, A5

Takeuchi, T. T., Buat, V., & Burgarella, D. 2005, A&A, 440, L17

Targett, T. A., Dunlop, J. S., McLure, R. J., Best, P. N., Cirasuolo, M., & Almaini, O. 2010, arXiv:1005.5176

Teplitz, H. I., McLean, I. S., Becklin, E. E., et al. 2000, ApJL, 533, L65

Teplitz, H. I., Desai, V., Armus, L., et al. 2007, ApJ, 659, 941

Thompson, T. A., Quataert, E., & Murray, N. 2005, ApJ, 630, 167

Thompson, T. A. 2009, Astronomical Society of the Pacific Conference Series, 408, 128

Thrall, H., Muxlow, T. W. B., Beswick, R. J., & Richards, A. M. S. 2007, Deepest Astronomical Surveys, 380, 291

Tielens, A. G. G. M. 2008, ARA&A, 46, 289

Totani, T., Takeuchi, T. T., Nagashima, M., Kobayashi, M. A. R., & Makiya, R. 2011, arXiv:1103.5402

Tresse, L., & Maddox, S. J. 1998, ApJ, 495, 691

Vacca, W. D., Cushing, M. C., & Rayner, J. T. 2003, PASP, 115, 389

Veilleux, S., Kim, D.-C., & Sanders, D. B. 2002, ApJS, 143, 315

Weiner, B. J., Papovich, C., Bundy, K., et al. 2007, ApJL, 660, L39

Willmer, C. N. A., et al. 2006, ApJ, 647, 853

Wilson, C. D., et al. 2008, ApJS, 178, 189

Wilson, G. W., et al. 2008, MNRAS, 390, 1061

Wu, H., Cao, C., Hao, C.-N., Liu, F.-S., Wang, J.-L., Xia, X.-Y., Deng, Z.-G., & Young, C. K.-S. 2005, ApJL, 632, L79

Wu, Y., Shi, Y., Helou, G., et al. 2011, ApJ, 734, 40

Xu, C., Hacking, P. B., Fang, F., et al. 1998, ApJ, 508, 576

Xu, C. 2000, ApJ, 541, 134

Yahil, A., Strauss, M. A., Davis, M., & Huchra, J. P. 1991, ApJ, 372, 380

Yee, H. K. C., Ellingson, E., Bechtold, J., Carlberg, R. G., & Cuillandre, J.-C. 1996, AJ, 111, 1783

Younger, J. D., et al. 2008, ApJ, 688, 59

Younger, J. D., et al. 2010, MNRAS, 984

Yuma, S., Ohta, K., Yabe, K., Kajisawa, M., & Ichikawa, T. 2011, arXiv:1105.2598

Zehavi, I., et al. 2005, ApJ, 630, 1

Zhu, G., Moustakas, J., & Blanton, M. R. 2009, ApJ, 701, 86